Fluorescence Technology Development for *In Vivo* Inflammation Sensing, Cell Contact Labeling, and Targeted Photoablation

Daniel S. Ackerman

submitted in partial fulfillment of the requirements
for the degree of Doctor of Philosophy

Department of Biological Sciences
Carnegie Mellon University
Pittsburgh, PA USA

Advisors: Jonathan W. Jarvik and Marcel P. Bruchez, PhDs

Table of Contents

Part 1 – The Biotattoo: Developing Cutaneous Biosensor Technologies for Real-time Inflammation Monitoring *in vivo* 1

Abstract (Part 1) 1

Introduction (Part 1) 2

Chapter 1 – *In Vitro* Survey of Adeno-Associated Virus (AAV) Infectivity in Murine and Human Skin Cells 12

Introduction 12

Results 16

Discussion 29

Materials and Methods 33

Chapter 2 – Development and Validation of AAV Drivers of Inflammation-responsive Fluorescence *In Vitro* and *In Vivo* 45

Introduction 45

Results 48

Discussion 59

Materials and Methods 62

Conclusions and Future Directions (Part 1) 67

Part 2 – TEFLA and TAPS: Expanding the Fluorogen Toolkit for *in vitro* Cell Contact Sensing and Targeted Photoablation 71

Abstract (Part 2) 71

Introduction (Part 2) 72

Chapter 3 – Tethered Dual Fluorogens Fluorescently Label Intercellular Contacts 77

Introduction 77

Results 81

Discussion 91

Materials and Methods 94

Chapter 4 – FAP-Antibody Fusions Facilitate Antigen-Specific Labeling, Intercellular Contact Sensing, and Photoablation 99

Introduction 99

Results 102

Discussion 116

Materials and Methods 118

Conclusions and Future Directions (Part 2) 127

Abbreviations 130

References..131

List of Figures and Tables

Part 1 – The Biotattoo: Developing Cutaneous Biosensor Technologies for Real-time Inflammation Monitoring *in vivo* 1

Figure 1-1. Plan for using adeno-associated viral vectors to transform skin cells into inflammation sensors. 6

Figure 1-2. Mechanism of AAV-driven transformation of endogenous cells into real-time reports of inflammation. 9

Chapter 1 – *In Vitro* Survey of Adeno-Associated Virus (AAV) Infectivity in Murine and Human Skin Cells 12

Figure 1-3. Transgene employed in the control AAV genome of serotypes 1, 2, 5, 6, and 8 from the University of Pennsylvania Vector Core. 17

Figure 1-4. Transduction efficiencies of common AAV serotypes in MPEK keratinocytes and 3T3 fibroblasts. 19

Figure 1-5. Representative confocal transmitted light (left) and fluorescence (right) microscopy images of 3T3s and MPEKs transduced at viral dose = 10,000 GC/cell. 20

Figure 1-6. Transduction efficiency of AAV2 and AAV6 on mouse skin cells. 22

Figure 1-7. Intradermally-delivered AAV2 and AAV6 transduce skin cells to produce fluorescent protein in vivo. 26

Figure 1-8. In vivo cutaneous transduction with AAV2 and AAV6 does not lead to preferential targeting of keratinocytes or fibroblasts. 28

Figure 1-S1. Representative dot plots and gating from flow cytometry analyses shown in Figure 1-6. 39

Figure 1-S2. Raw data from post-processing of in vivo images shown in Figure 1-7 using IVIS Spectrum CT software. 40

Table 1-S1. Statistical analyses of AAV infectivity comparison data shown in Figure 1-4. 41

Table 1-S2. Statistical analyses of AAV2 titration curves shown in Figure 1-6A. 42

Table 1-S3. Statistical analyses of AAV6 titration curves shown in Figure 1-6B. 43

Table 1-S4. Statistical analysis of *in vivo* data shown in Figures 1-7C and -7D.... 44

Chapter 2 – Development and Validation of AAV Drivers of Inflammation-responsive Fluorescence *In Vitro* and *In Vivo* 45

Figure 2-1. Inflammation-responsive transgene that drives reporter protein production in response to NF-κB activation. 50

Figure 2-2. HEK-293 cells transfected with pAAV-4xNFkB-mCherry-PEST express inflammatory signaling-dependent fluorescent protein. 52

Figure 2-3. AAV inflammation sensors do not drive measurable reporter production when fluorescent proteins are used. 55

Figure 2-4. AAV-based luminescent reporters drive inflammation-responsive signal in living rat skin. 58

Figure 2-S1. AAV8 exhibits higher infectivity in hairless rat skin than other comparable serotypes. 66

Part 2 – TEFLA and TAPS: Expanding the Fluorogen Toolkit for *in Vitro* Cell Contact Sensing and Targeted Photoablation 71

Figure 3-1. Fluorogen-activating proteins induce fluorescence from fluorogen ligands. 75

Chapter 3 – Tethered Dual Fluorogens Fluorescently Label Intercellular Contacts 77

Figure 3-2. Trans-TEFLA allows fluorescent labeling of cell contacts *in vitro*. ... 80

Figure 3-3. Visualization of cell-cell contacts with simultaneous application of bivalent (biotin-PEG2000-DIR) and monovalent (TO1-2p) reagents. 84

Figure 3-4. Visualizing formation and loss of cell-to-cell contacts using trans-TEFLA. 86

Figure 3-5. Bivalent FAP reagent selectively labels intercellular contacts with bright, dual-color fluorescence 89

Figure 3-S1. Trans-TEFLA reagents applied to single cognate-expressing HEK-293 cells with or without counterstain. 97

Figure 3-S2. Quantification of increase in fluorescence intensity at points of contact between HL1 and dL5 surface-expressing cells exposed to 25 nM MG-PEG3500-TO1 trans-TEFLA reagent. 98

Chapter 4 – FAP-Antibody Fusions Facilitate Antigen-Specific Labeling, Intercellular Contact Sensing, and Photoablation 99

Figure 4-1. dL5-cetuximab labels EGFR on HaCaT and A431 cells. 103

Figure 4-2. dL5-cetuximab labels EGFR on fixed HaCaT cells. 105

Figure 4-3. dL5-trastuzumab labels HER2 on SK-BR-3 cells. 106

Figure 4-4. dL5-cetuximab facilitates trans-TEFLA with only one partner expressing transgenic FAP. 109

Figure 4-5. dL5-cetuxiumab and MG-2I mediate cell death in EGFR-expressing cells 111

Table 4-1. Fluorescence intensity data from plate reader analysis of alamarBlue-treated HEK-293, HaCaT, and A431 cells after treatment with dL5-cetuximab +MG-2I and photoirradiation. 113

Figure 4-6. dL5-trastuzumab and MG-2I mediate cell death in HER2-expressing SK-BR-3 cells 115

Figure 4-S1. HTB1-FAP(dL5) reagent conjugated to cetuximab. 123

Figure 4-S2. Flow cytometric analysis of cytotoxic response via Eth-D staining in HEK, HaCaT, and A431 cells after dL5-cetuximab and MG-2I treatment and photoirradiation. 124

Figure 4-S3. Representative dot plots from flow cytometry data shown in Figure 3-S2. 125

Table 4-S1. Total number of singlet cells analyzed per condition to generate the data shown in Figure 4-S2........................126

Part 1 – The Biotattoo: Developing Cutaneous Biosensor Technologies for Real-time Inflammation Monitoring *in vivo*

Abstract (Part 1)

Diseases of the immune/inflammatory system are a widespread and significant source of pain and cost to global populations. Common, diverse, and highly variable in both symptoms and underlying mechanisms, these inflammatory disorders are challenging to address in the clinic. Critical for the development, validation, and clinical efficacy of anti-inflammatory therapeutics are bio-monitoring technologies that allow clinicians to monitor the progression of autoimmune disorders and their response to anti-inflammatory drugs. However, such technologies often suffer significant problems in their timing, means of monitoring, and lack of responsiveness to cellular-level changes in inflammatory bioactivity. Here, I describe efforts to coordinate advances in virology, cell biology, and biomedical engineering to develop and validate an *in vivo* real-time biosensor of inflammation based on cutaneous gene delivery strategies. Chapter 1 shows a survey of adeno-associated virus infectivity in skin cells, designed to facilitate inflammation reporter development *in vitro* and *in vivo*. Chapter 2 describes the development and validation of prototype inflammation sensors in the skin of an animal model. Together, these results lay the groundwork for development of an *in vivo* inflammation biosensor capable of providing real-time information on inflammatory bioactivity from the skin of a living animal.

Introduction (Part 1)

The immune system is controlled through the function and regulation of inflammation-linked transcription factors. Activated by circulating signaling molecules called cytokines, these factors bind to promoter elements in the DNA to either activate or abrogate expression of particular genes and change cell behavior. These changes form the backbone of the inflammatory response, including changes in metabolism, increased production of growth factors, and expression of more cytokines[1]. These, in turn, spur further inflammation, regulating a complex interplay between inflammation-linked genetic networks that activate and repress each other in response to multiple inputs[1,2]. The large degree of interconnectivity between inflammatory networks can lead to significant consequences from small disruptions in their ability to perform normally, and dysregulated inflammation can lead to many pathologies. These include cancers, which routinely avoid destruction by altering the body's immune activity[3–5], and autoimmune diseases such as rheumatoid arthritis, where inflammatory pathways are explosively overactive.

Autoimmune diseases are commonly treated with drugs to depress the inflammatory response by targeting specific cytokines[4,6], lowering the activity of their associated transcription factors. Patient-to-patient variability in response to these drugs is often high[7]. Inflammation monitoring is therefore crucial for measuring the reaction of individual patients to specific treatment regimens and for assessing the efficacy of cytokine-targeting therapeutics. The use of simple markers (e.g. joint counts and patient questionnaires) to track changes in inflammation, though common, is entirely qualitative and unable to provide detailed information on changes in immune activity. Because of this, current top-of-the-line inflammation monitoring techniques depend on quantitative assays of cytokine levels as biomarkers for autoimmunity. The most widely-used of these assays involve exposing patients' blood samples to cytokine-specific antibodies to measure their levels in the serum[8]. Unfortunately, these assays universally suffer from an array of problems related to their *ex vivo* nature, including lengthy sample preparation times and long sampling intervals between serum collections[8–10]. Additionally, although accurately measuring blood cytokine levels, these methods are unable to provide information on the bioactivity of these cytokines on inflammatory gene networks. This activity depends on many factors beyond blood cytokine concentration[11], and cytokine bioactivity has been found to be poorly predicted by immunoassays[12]. More sophisticated methods have been developed that involve the use of reporter cell lines to quantify the activity of cytokine antagonists present in patient serum samples[6]. Although offering more biologically relevant data on inflammation levels, such assays still involve substantial sample preparation time and are limited to providing snapshots of inflammatory activity without any information on its *in vivo* dynamics.

Because of these limitations, there is a vital need in the current clinical repertoire for a method of monitoring *in vivo* inflammation levels in real time[7–9,13,14]. Such an assay would allow sophisticated assessment of inflammatory dynamics and their response to therapeutics and other inflammation-controlling technologies[10]. Clinically-focused research has begun to shift toward the development of new assays to achieve these goals. Recently, a prototype *in vivo* inflammation sensor was developed using a pH-sensitive, nanosphere-linked fluorescent dye to report on inflammatory acidosis in real time[15]. This method links noninvasive monitoring with rapid, sensitive measurement and reports directly on a specific aspect of inflammatory bioactivity. However, as tissue acidosis is a localized phenomenon confined to sites of inflammation[16], this assay is unable to be used as a reporter on global activity. This problem is exacerbated by the low tissue-penetrance of the proposed dye-carrier nanospheres, limiting the regions to which these reporters could be delivered and observed *in vivo*[15]. The localization of this inflammatory side effect is in contrast to the systemic distribution of cytokine molecules, which are known to be widely disseminated *in vivo* during autoimmune diseases and other major inflammatory events[12]. This suggests the possibility of using circulating cytokine levels in easy-to-access tissues as reporters for inflammation levels throughout the body. Ideally, these reporters would respond directly to the bioactivity of cytokines rather than relying on indirect measures.

Part 1 of my thesis describes my work on developing such a technology for monitoring global inflammation bioactivity levels in real time. This project, a collaboration between Carnegie Mellon's Biological Sciences and Biomedical Engineering departments, centered around using fluorescent reporters under the transcriptional control of inflammatory factors, a common method for assaying the activity of these critical regulators *in vitro*. However, we aimed to expand significantly on previous assays by packaging this reporter DNA into adeno-associated viruses (AAV) for *in vivo* delivery. These viruses would be used to transport inflammation-responsive vectors to endogenous skin cells, creating a “biotattoo” of cells expressing reporter protein in response to the activity of specific transcription factors (Figure 1-1).

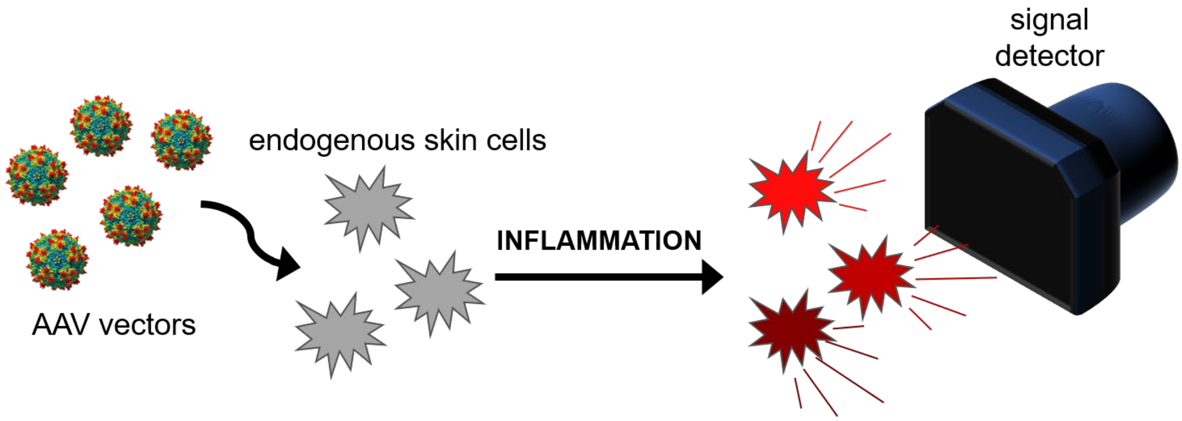
signal
detector
endogenous skin cells
INFLAMMATION
AAV vectors

Figure 1-1. Plan for using adeno-associated viral vectors to transform skin cells into inflammation sensors. AAV vectors are introduced to endogenous skin cells (keratinocytes and/or fibroblasts) which then produce a measurable protein (e.g. fluorescent or luminescent reporter) in response to an increase in local levels of inflammatory signaling molecules. AAV space-filling model from Samulski & Muzyczka[17].

AAV is a class of small, replication-deficient parvovirus that has become increasingly popular in gene therapy research due to its nonpathogenicity, low immunogenicity, and track record of safety in animal research and clinical trials[17,18]. It is capable of infecting both dividing and quiescent cells and is remarkably cell-friendly, producing no cytotoxic effects even at high multiplicities of infection (viruses per cell) tested *in vitro*[19,20] and in *in vivo* and human studies[17]. AAV-delivered recombinant DNA does not integrate into the host genome, existing instead in an extrachromosomal state with minimal risk of causing mutations or other adverse genetic effects[21].

AAV-based inflammation reporters have been described in recent literature and have been deployed successfully both *in vitro* and *in vivo*. A luminescent reporter was delivered to mouse pancreas to monitor the activity of nuclear factor-κB (NFκB), a critical inflammatory transcription factor[22], in an acute pancreatitis model[23], providing feedback on inflammatory dynamics in this organ. Separately, an AAV-delivered fluorescent reporter was developed as part of a study on gene therapy for inflammatory and degenerative diseases of the central nervous system[24]. This vector produced GFP in response to NFκB activation in the neurons of a temporal lobe epilepsy mouse model. These studies lend support to the usability of AAV for producing *in vivo* inflammation sensors by linking reporter proteins to transcription factor-specific binding elements.

In designing our inflammation sensor, we wanted to avoid deploying it to deeper tissues for a number of reasons: (1) deeper tissues are more difficult to reach, lowering clinical applicability; (2) biological tissue could hamper reporter measurement by light scattering; and (3) transduction of interior organs such as the pancreas exposes the virus to the bulk bloodstream, increasing the chances of off-target infections or clearance in the liver. Because of these issues, we settled on skin cells (keratinocytes and/or dermal fibroblasts) as an optimal reservoir to produce our inflammation-responsive reporter proteins. These cells are a tempting target for the deployment of these inflammation-responsive vectors, as fluorescence close to the body's surface is comparatively easy to observe[25]. Additionally, despite their distance from the site of localized inflammatory events (e.g. joints in rheumatoid arthritis), these cells are expected to respond to global inflammation levels. Major inflammatory pathologies (including autoimmune diseases like rheumatoid arthritis and lupus erythematosus) cause widespread release and systemic circulation of cytokines through the body[12,26,27]. Indeed, these inflammatory profiles can lead to significant additional risks, including a higher chance of developing cardiovascular disease in arthritis patients[28]. Skin cells exchange analytes efficiently with the bloodstream[29,30] and should reliably report on the activity of these cytokines circulating in response to major inflammatory events. Stimulation of inflammatory transcription factor reporters in skin cells is therefore expected to reflect global inflammation levels *in vivo*. Figure 1-2 shows a complete schematic of the pathway by which viral vectors carrying reporter DNA can be used to surveil immune signaling pathways and provide real-time readout on the activity of inflammatory transcription factors.

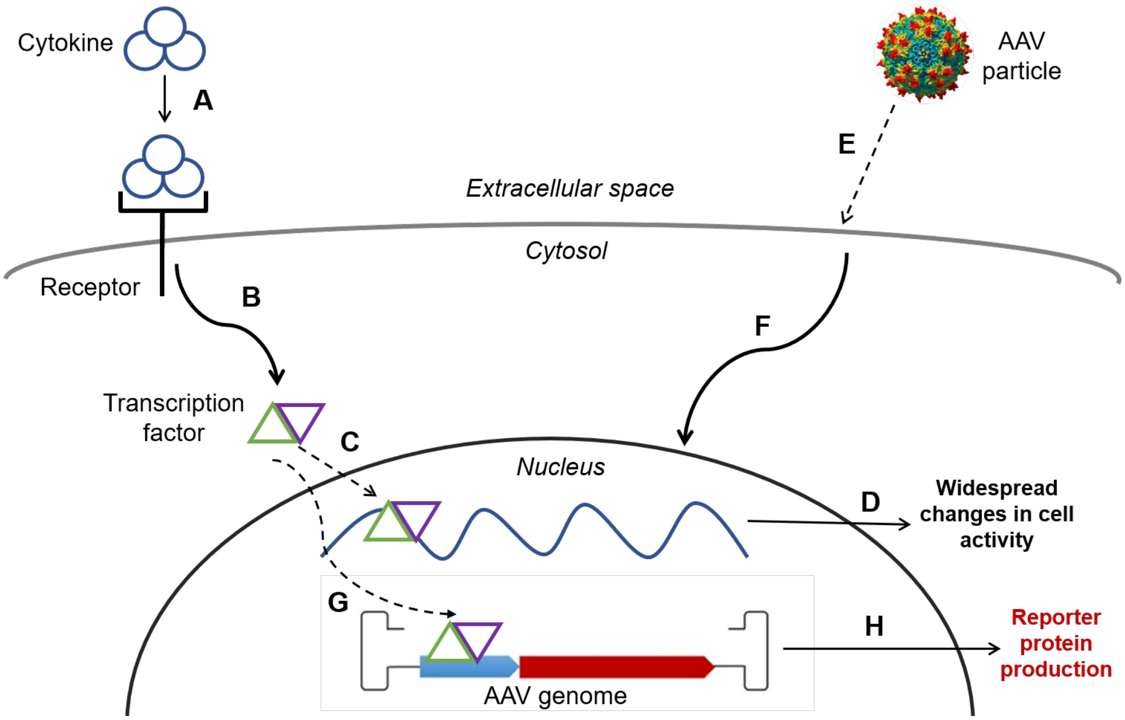
Cytokine
A
AAV particle
E
Extracellular space
Cytosol
Receptor
B
F
Transcription factor
C
Nucleus
D
Widespread changes in cell activity
G
H
Reporter protein production
AAV genome

Figure 1-2. Mechanism of AAV-driven transformation of endogenous cells into real-time reports of inflammation. Inflammatory signaling pathways are activated by circulating molecules called cytokines binding (**A**) to their cognate cell-surface receptors. This begins an intracellular signal cascade (**B**) that ends with the activation of inflammatory transcription factors and their translocation to the nucleus (**C**). There, they bind to endogenous target sites present throughout the genome, leading to changes in gene expression (**D**). At (**E**), this cell is transduced with an AAV vector carrying the gene for a reporter protein driven by a consensus binding sequence for a given inflammatory transcription factor. After trafficking to a perinuclear space (**F**), AAV release their DNA into the nucleus (**G**), where it will be bound by activated transcription factors. This will lead to an increase in reporter protein production (**H**) alongside normal inflammatory changes in cell activity.

A large number of AAV serotypes have been developed for different purposes in the lab[17]. The proteins that form the viral capsid vary slightly between serotypes, leading to different patterns of cell-surface receptor binding. Because of this, AAV serotypes can have widely different infectivity patterns (tropisms) for various cell types. AAV research to date has tended to focus on transduction of a small number of model tissues, including liver, muscle, brain, and eye[31]. For the purposes of this project, it was necessary to use a serotype of AAV with a high level of infectivity for skin cells to (1) minimize the amount of virus required for later assays and (2) ensure that viral doses deliverable by intradermal injection will infect enough cells to allow visibility of inflammation reporter signal through the skin.

Chapter 1 describes the first half of my research in the biotattoo project: validating various serotypes of AAV as potential vectors for transduction of keratinocytes/dermal fibroblasts in living skin. Separate from the inflammation sensor development, the focus of this manuscript is on developing AAV as a cutaneous gene therapy vector. Although not a focus of the manuscript itself, this work was conducted to facilitate the development of optimized reporter vectors for cutaneous inflammation sensor construction. My research specifically into inflammation sensors will be discussed in Chapter 2. This includes *in vitro* design and testing of a prototype AAV inflammation reporter and its preliminary *in vivo* deployment in the skin of living rats. Together, this data should provide a promising foundation for the biotattoo project, showing the viability and potential of skin-based viral drivers of real-time inflammation reporters while highlighting the challenges of cutaneous vector deployment and the *in vitro* to *in vivo* transition.

Chapter 1 – *In Vitro* Survey of Adeno-Associated Virus (AAV) Infectivity in Murine and Human Skin Cells

This work is in review at PLOS One.

Ackerman, D. S.; Korkmaz, E.; Yalcintas, E. P.; Telmer, C. A.; Smith, J. D.; Campbell, P. G.; Jarvik, J. W.; Ozdoganlar, O.B.; and Bruchez, M.P. Adeno-associated virus-mediated cutaneous gene delivery in mice. *In review*.

Introduction

The skin is the front line of the immune system and the first barrier against pathogens and particulates in the environment[32,33]. Because of its easy accessibility to environmental insults, the skin is often the site of critical injuries beyond its capacity for self-regeneration[34]. It is also commonly affected by chronic autoimmune diseases (e.g. psoriasis and vitiligo), which impact approximately 10% of the population worldwide[30,35] and currently have no cure[36,37]. The potential of gene therapy to provide such a cure for cutaneous autoimmunity and to facilitate the healing of grievous wounds has cultivated interest in this field for many years[38–40]. Additionally, because of the rich vascularization of the dermis, the skin has the potential to act as a bio-reservoir for sustained release of secreted therapeutic proteins to alleviate distant ailments[41].

Efforts towards skin-directed gene therapy have included both transplantation of exogenously-altered cells and the direct modification of endogenous cells by a variety of methods, including transduction by recombinant viral vectors[42,43]. Adeno-associated virus (AAV) is a particularly attractive candidate for this purpose due to its ability to drive robust and long-lived transgene expression[17], its nonpathogenicity[44], and its overall clinical safety profile[17,18]. There is a wide variety of AAV serotypes capable of targeting many different tissues *in vivo*[45]. AAV can infect both dividing and non-dividing cells[46,47] with a genome that rarely inserts into host chromosomes, minimizing the possibility of insertional mutagenesis that is a primary risk of other gene therapy viral vectors[21,48]. Additionally, the low immunogenicity of AAV[44,46] increases its appeal as a gene therapy vector in comparison to viral alternatives (e.g. adenovirus[49], lentivirus, or other retroviruses).

Despite the advantages of AAV vectors, AAV-based cutaneous gene delivery poses significant challenges. While numerous studies have been conducted in human skin cells, they have shown conflicting results and generally low transduction efficiency[19,50–55]. Recent results with capsid-engineered virus shows promise for improving AAV transduction efficiency in human keratinocytes[34,56]. Nonetheless, given the regulatory constraints inherent to *in vivo* studies of viral infectivity in humans, murine models continue to have high importance for testing AAV in living organisms[20,34]. Most research has focused on deeper tissues and organs (e.g. liver and muscle) for long-term gene therapy. AAV transduction of mouse skin remains an understudied area, with most studies focusing on physical wound models[20].

Murine genetic models for inflammatory skin conditions, including psoriasis and atopic dermatitis, remain highly important both for drug development and for studying the underlying mechanisms of skin diseases[57–59]. Advances in cutaneous gene therapy in mice are therefore likely to contribute to the success of drug development and skin-targeted treatment efforts.

Current approaches to AAV-based cutaneous gene therapy in mice suffer from (1) a lack of reproducible transduction protocols due to a knowledge gap regarding the infectivity of AAV vectors toward skin cells, and (2) a limited understanding of *in vitro* and *in vivo* AAV cutaneous transduction characteristics[60].

Here, a systematic survey of AAV transduction efficiency in mouse skin cells *in vitro* has identified AAV serotypes that are highly infective in mouse keratinocytes and fibroblasts under standard culture conditions. Specifically, we tested identical genome GFP-expressing viral vectors prepared from widely-available AAV serotypes – 1, 2, 5, 6, 8, and DJ (a synthetically-developed serotype with a hybrid capsid[61]). These AAV serotypes were used to measure infectivity and selectivity for transduction of cultured murine cells representing the two most prevalent cell types in the skin: NIH-3T3 cells (fibroblasts) and MPEK-BL6 cells (keratinocytes). Transduction efficiencies were studied both qualitatively and quantitatively via confocal fluorescence microscopy and flow cytometry, respectively. The serotypes with the highest infectivity were then delivered to the skin *in vivo* using intradermal delivery in athymic nude mice. Taken together, our results provide (1) a quantitative knowledge base of serotype infectivity in cultured cells, and (2) a qualitative demonstration of the ability of the identified AAV serotypes to drive robust transgene expression in the cutaneous microenvironment *in vivo*.

Results

Comparison of AAV serotype infectivity in cultured mouse fibroblasts and keratinocytes.

AAV of serotypes 1, 2, 5, 6, 8, and DJ were chosen to screen for relative infectivity in mouse keratinocytes and fibroblasts *in vitro*. These particular serotypes were used due to their commercial availability and their history of use in the literature[31]. To facilitate comparison, for each serotype, viruses that carry an identical transgene (Figure 1-3) with enhanced green fluorescent protein (eGFP) were used. Expression of eGFP is driven by the constitutively-active cytomegalovirus (CMV) promoter element, which drives high levels of expression *in vitro*[62]. Cells that are effectively transduced with these constructs are expected to produce high levels of eGFP, thereby allowing simple analysis of the infected cells through fluorescence detection.

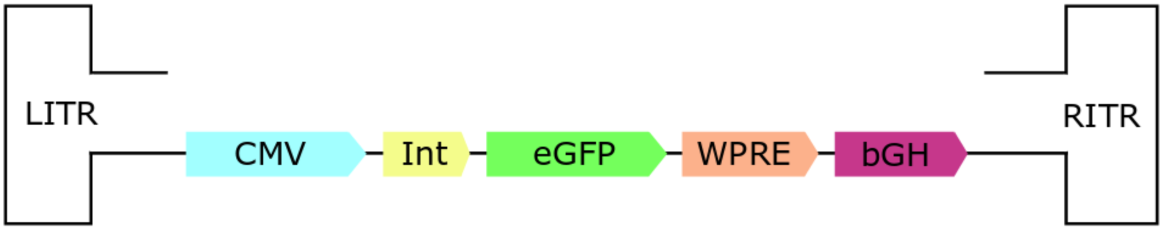

Figure 1-3. Transgene employed in the control AAV genome of serotypes 1, 2, 5, 6, and 8 from the University of Pennsylvania Vector Core. Also used in construction of AAV-DJ by the Stanford Gene Vector and Virus Core. Elements are not shown to scale. This transgene is encoded by a cis-plasmid delivered to virus-producing cells during AAV production and is processed and incorporated into virus particles as single-stranded DNA flanked by hairpin inverted terminal repeats (ITRs)[18]. The core elements of this genome are the constitutive CMV promoter and the eGFP fluorescent protein gene that the promoter drives. Int = SV40 intron; bGH = bovine growth hormone poly(A). The included woodchuck hepatitis virus post-transcriptional regulatory element (WPRE) enhances the expression of viral transgenes[170] and is commonly included in AAV vectors[171].

MPEK-BL6 and NIH-3T3 cells were selected as *in vitro* models of murine keratinocytes and fibroblasts, respectively. MPEK-BL6 cells (MPEKs) are spontaneously immortalized mouse keratinocytes that are isolated from normal C57BL/6 mouse skin and have been used previously in studies of mouse skin immunology[63,64] and other basic processes[65,66]. NIH-3T3 cells (3T3s) have been utilized in a multitude of mouse fibroblast studies[67].

To obtain a baseline evaluation of the infectivity of each viral serotype in these cell types, MPEK and 3T3 cells were plated and separately transduced with each of the above six serotypes at a viral dose of 10,000 genome copies (GC; also referred to as viral genomes [vg]) per cell. Forty-eight hours post-treatment, the transduction efficiencies were determined by using flow cytometry to count the percentage of cells expressing the transgene for eGFP (Figure 1-4), as previously described[19,68,69]. The infectivity of AAV1 was approximately 3% in both MPEK and 3T3 cells. AAV5 and AAV8 both transduced less than 1% of the cultured cells. The infectivity of AAV-DJ in 3T3 cells was also below 1%; however, the serotype showed approximately 7% infectivity in MPEK cells. AAV6 and AAV2 transduced keratinocytes and fibroblasts, respectively, at high levels while showing little transduction in the other cell line. The infectivity of AAV2 in 3T3 cells and in MPEK cells was around 20% and 2%, respectively, and the infectivity of AAV6 in 3T3s and in MPEKs was about 1% and 23%, respectively. Representative fluorescence microscopy images of cells transduced by AAV2 and AAV6 are shown in Figures 1-5A (3T3s) and -5B (MPEKs).

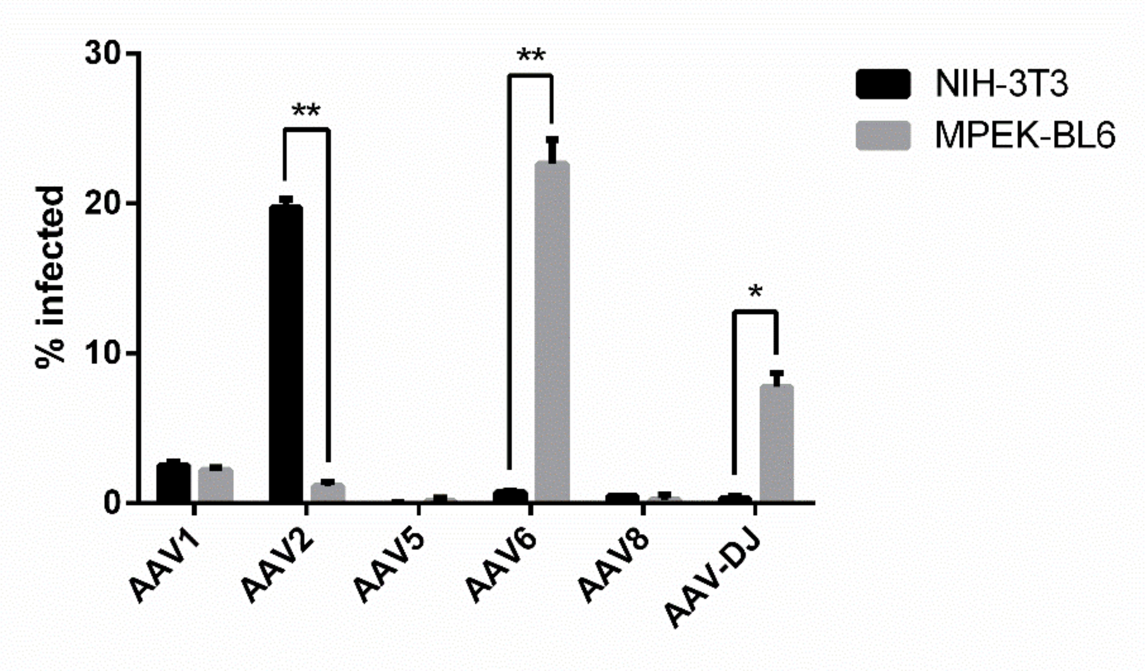

Figure 1-4. Transduction efficiencies of common AAV serotypes in MPEK keratinocytes and 3T3 fibroblasts. Cells were transduced with 10,000 GC/cell and analyzed for eGFP expression via flow cytometry 48 hours after treatment. % infected = the percentage of cells expressing eGFP fluorescence, representing the serotype's transduction efficiency. Data shown are the average of three replicates ± SD. * = $p < 0.01$; ** = $p < 0.001$ (Table 1-S1).

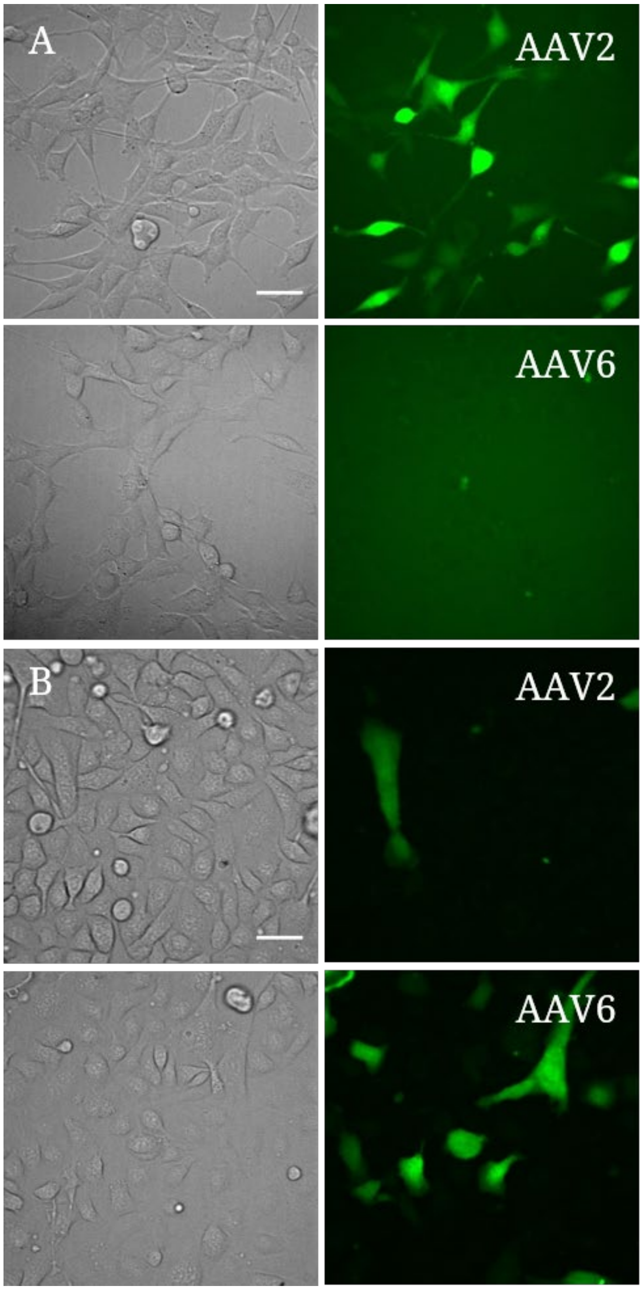

Figure 1-5. Representative confocal transmitted light (left) and fluorescence (right) microscopy images of 3T3s and MPEKs transduced at viral dose = 10,000 GC/cell. Cells were seeded onto an optical-bottom 96-well plate for imaging and subsequent flow cytometry analysis. (**A**) 3T3 cells expressing eGFP via AAV2 or AAV6 transduction. (**B**) MPEK cells expressing eGFP via infection by the same serotypes. Scale bars = 40 µm.

Transduction efficiency of AAV2 and AAV6 in fibroblasts and keratinocytes at varying viral doses.

The results presented in Figure 1-4 prompted further experiments with AAV2 and AAV6. MPEK and 3T3 cells were transduced with AAV2 and AAV6 at doses of $5x10^3$, $2x10^4$, $5x10^4$, and $1x10^5$ GC/cell to construct titration curves (transduction efficiency vs. viral dose) for both viruses in both cell types over a range of physiologically relevant viral doses[19]. These cells were quantitatively analyzed for eGFP expression at 48 hours post-treatment to determine their transduction efficiencies.

The titration curves for AAV2 and AAV6 are shown in Figure 1-6. AAV2 is more infective in 3T3 cells than in MPEK cells over a wide range of viral doses, with its transduction efficiency appearing to plateau close to 85% (Figure 1-6A). Over this same range, its infectivity in MPEK cells barely approaches 5%. However, this ratio is nearly flipped for AAV6, which reached a maximum of 85% infectivity in keratinocytes (Figure 1-6B). This serotype displays higher infectivity in fibroblasts than does AAV2 in MPEKs, with its transduction efficiency reaching 10% at the highest viral dose tested.

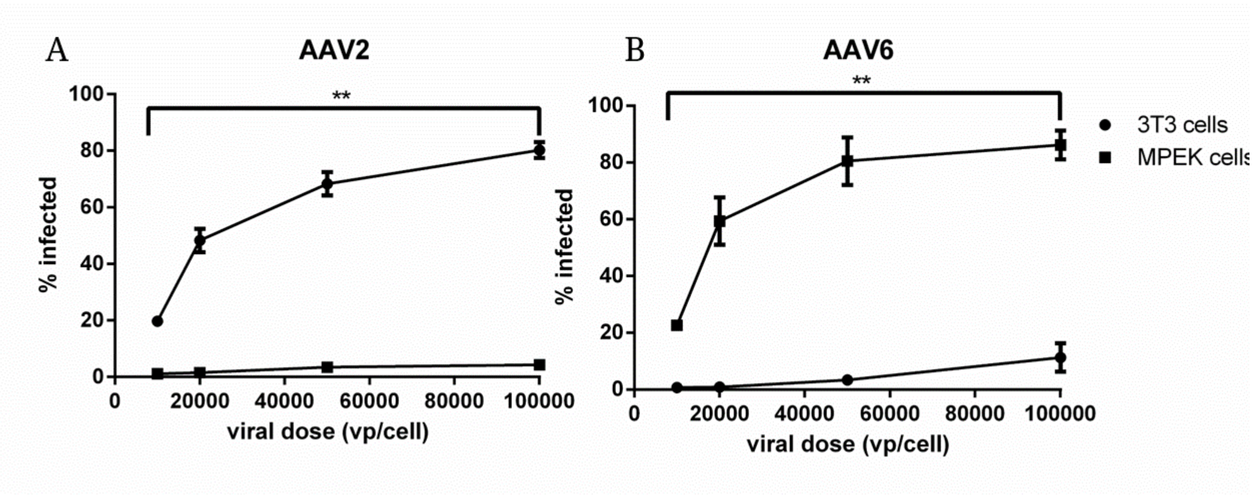

Figure 1-6. Transduction efficiency of AAV2 and AAV6 on mouse skin cells. AAV2 displays higher infectivity in mouse fibroblasts than in keratinocytes, while AAV6 shows the opposite tropism. Cells were transduced with the viruses and analyzed for eGFP expression two days later. (**A**) Titration curves showing infectivity of AAV2 in 3T3 fibroblasts (circles) and MPEK keratinocytes (squares) over a range of viral doses. (**B**) Titration curves showing transduction efficiency of AAV6 for the same cell types. Viral dose = 10,000 data are the average of three replicates ± SD. Other data are the average of three independent experiments ± SD. Lack of error bar indicates error too small to show to scale. ** = $p \leq 0.001$ (Tables 1-S2 and -S3).

Analysis of the fold infectivity of AAV2 in 3T3s over MPEKs, and AAV6 in the opposite ratio, shows the trend in selective transduction efficiency generated from these data. Although the highest ratios are achieved at the lowest viral dose, where the infectivity of both serotypes in the other cell type is close to zero, the absolute numbers at the lowest doses are relatively low. These viral doses may therefore not be suitable for *in vitro* experiments requiring widespread transgene expression. However, even at the highest doses tested, AAV2 is roughly 18 times more infective in 3T3s than in MPEKs. AAV6 transduced fibroblasts more effectively than AAV2 did keratinocytes, lowering the selectivity ratio in MPEKs at the highest dose of 100,000 GC/cell to only about 8.5-fold. However, using a dose of 50,000 GC/cell dropped the infectivity in keratinocytes only slightly (~85% to 80%) while substantially decreasing the percentage of transduced fibroblasts, resulting in a higher selectivity ratio of ~26.5x.

In vivo analysis of AAV2 and AAV6 infectivity in the cutaneous microenvironment.

With AAV2 and AAV6 having demonstrated superior transduction efficiency for cultured mouse fibroblasts and keratinocytes, respectively, we next tested their transduction efficiency in living mouse models in the cutaneous microenvironment *in vivo*. The infectivity profile of AAV (both transduction efficiency and tropism) is known to vary unpredictably between *in vitro* and *in vivo*[19,20], perhaps owing to the greater biochemical and environmental complexity within living tissue. To explore this, we conducted an *in vivo* study of AAV2 and AAV6 cutaneous infectivity in athymic nude mice. The mice were injected intradermally with AAV2 and AAV6 vectors containing the -CMV-eGFP genome (Figure 1-3), identical to those used in our *in vitro* studies. Effective transduction of skin cells would therefore be indicated by local transgene (eGFP) expression at the injected skin sites. Although biological tissue autofluorescence is high in the green optical range, the proximity of the fluorescing cells to the surface of the tissue was expected to minimize light scattering sufficiently to make fluorescent signal localization possible.

Traditional intradermal injections into the skin microenvironment are particularly challenging in mice, where the skin is extremely thin[70]. Therefore, in complement with our intradermal injections, we delivered AAV to the skin of the nude mouse models using dissolvable microneedle arrays (dMNAs). dMNAs are a well-established intradermal delivery method that has been used to successfully transport various biological cargoes[71,72], including live virus[73,74], into the skin. We used dMNAs loaded with either AAV2-CMV-eGFP or AAV6-CMV-eGFP to precisely deliver the virus into the thin skin of nude mice. Delivered viral doses were approximately 1.3×10^{10} vp/injection (10μL) for the intradermal injections and 3.1×10^{9} vp/application for the AAV-dMNAs.

Figure 1-7 shows representative fluorescence images taken 72 hours after administration of AAV to the skin of our nude mouse models. We used this early timepoint to minimize the impact of cutaneous cell migration and division on apparent fluorescent intensity *in vivo*[20]. Figures 1-7A and -7B show the results of the intradermal injections and MNA applications, respectively. Both methods of viral delivery resulted in eGFP-expressing cells localized at the injected sites. We subsequently sacrificed the mouse and excised the skin to minimize noise from the autofluorescence of underlying tissues and confirm the localization of fluorescent cells in the skin. All four expression sites are clearly visible in Figure 1-7C, and their fluorescence emission was significantly higher than the surrounding background autofluorescence (Figure 1-7D).

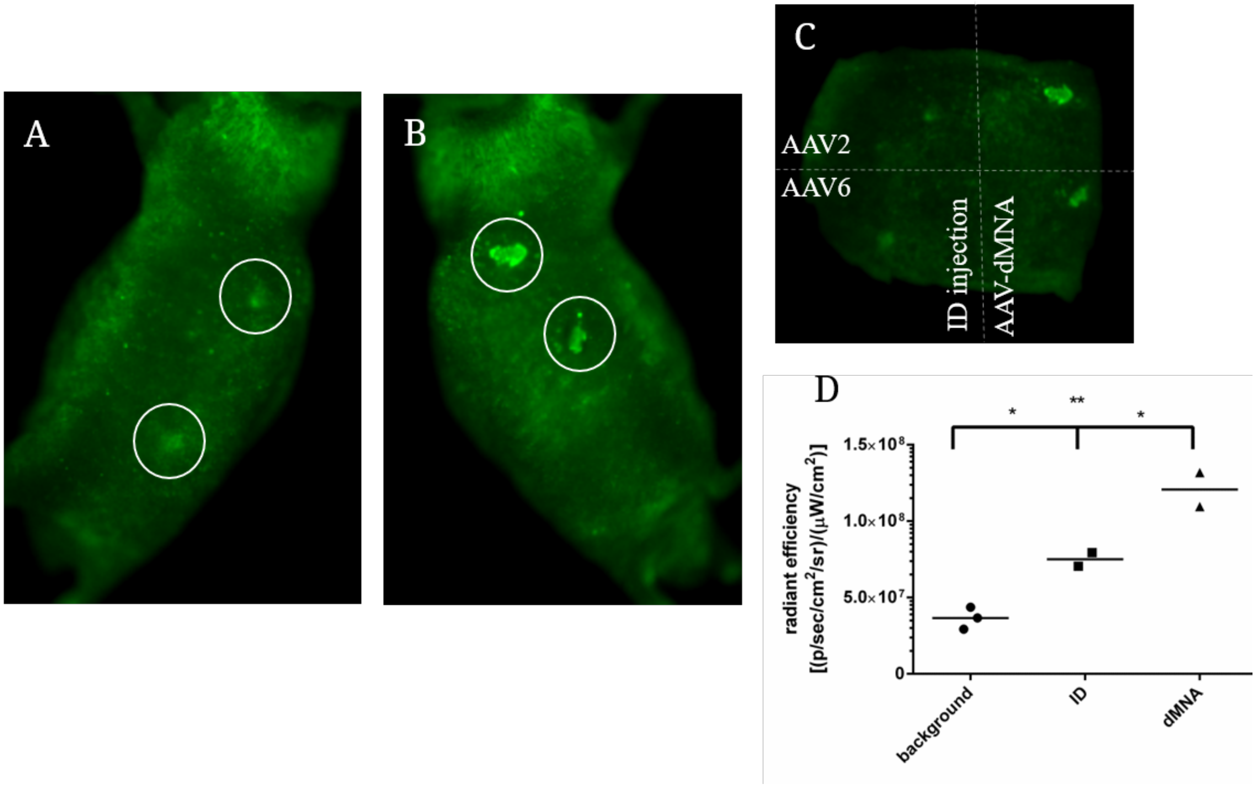
A
B
C
AAV2
AAV6
ID injection
AAV-dMNA
D
*
**
*
radiant efficiency
[(p/sec/cm²/sr)/(µW/cm²)]
1.5×10⁸
1.0×10⁸
5.0×10⁷
0
background
ID
dMNA

Figure 1-7. Intradermally-delivered AAV2 and AAV6 transduce skin cells to produce fluorescent protein in vivo. (**A**) ID-injected left side of the nude mouse. White circles indicate the ID injection sites of AAV2- (upper) and AAV6- (lower) CMV-eGFP. (**B**) MNA-treated right side of the mouse. Circles show the MNA application sites for AAV2 (upper) and AAV6 (lower). (**C**) Skin explant isolated from the treated nude mouse. eGFP expression sites appear as brighter green patches and are labeled with their viral serotype and route of delivery. All expression sites are shown approximately 72 hours post-AAV application. Images have identical lookup tables to allow quantitative comparison. (**D**) Radiant efficiency (fluorescence) measurements of fluorescing vs. non-fluorescing (background) sites (Figure 1-S2). Data shown are individual data points with mean. * = $p < 0.05$. ** = $p < 0.005$ (Table 1-S4).

To observe the transduced cells directly, expression sites were isolated from the skin sample using a biopsy punch and prepared for cryo-sectioning and fluorescence microscopy. Epifluorescence microscopy on these skin sections was performed to confirm the presence of eGFP-expressing cells. These results are shown in Figures 1-8A and -8B for AAV2 and AAV6, respectively. Here, the epidermal keratinocytes are present as a thin band of tightly-packed cells just under the *stratum corneum*, while the rest of the cells are primarily dermal fibroblasts. Both AAV2 and AAV6 were effective at transducing murine skin cells *in vivo*, with fluorescent cells observed in the local area around the AAV application sites. Both serotypes appeared to transduce primarily dermal fibroblasts based on their location in the skin. Overall, these results show that AAV of serotypes 2 and 6 are capable of transducing mouse skin cells *in vivo* when delivered by either intradermal injection or MNA application.

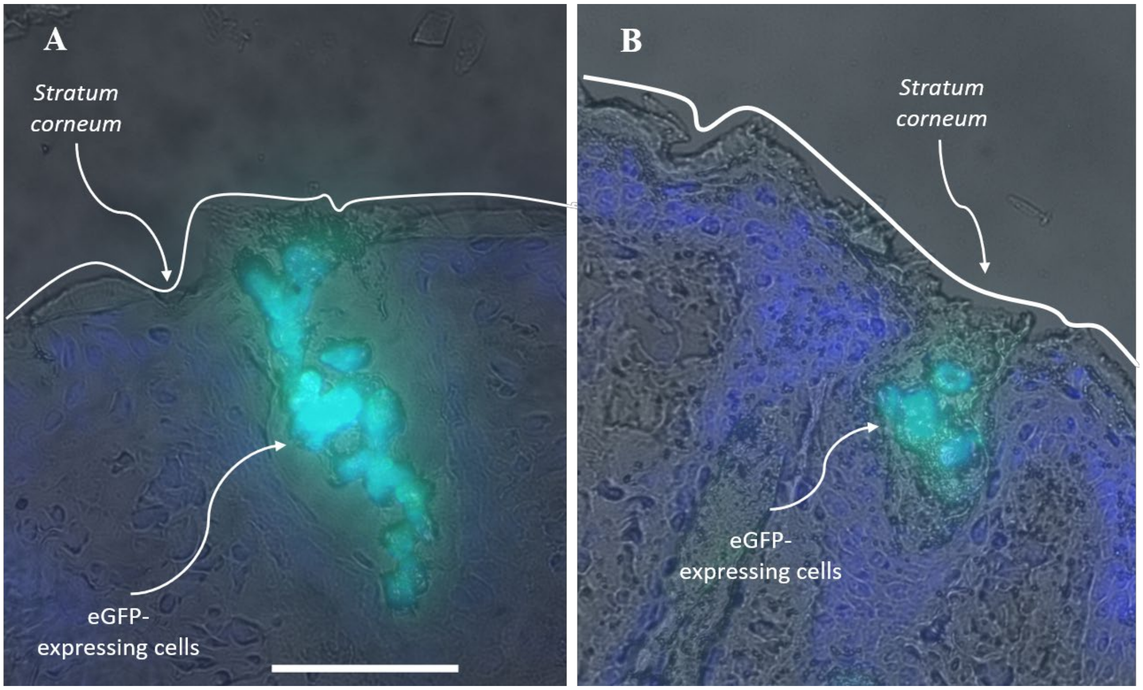
A
Stratum corneum
eGFP-expressing cells
B
Stratum corneum
eGFP-expressing cells

Figure 1-8. In vivo cutaneous transduction with AAV2 and AAV6 does not lead to preferential targeting of keratinocytes or fibroblasts. Blue fluorescence is DAPI nuclear stain; green fluorescence is eGFP. (**A**) Fluorescence micrograph showing eGFP-expressing cells in cross-section of mouse skin transduced with AAV2-CMV-eGFP via dMNA application. Expressing cells and approximate boundaries of the *stratum corneum* are shown. (**B**) Micrograph showing cells transduced by AAV6-CMV-eGFP via dMNA. Scale bar = 50 µm.

Discussion

Cutaneous gene therapy has the potential for (1) treating severe wounds that damage the skin to the extent that it fails to regenerate[20]; (2) enabling novel therapies for skin inflammatory diseases such as psoriasis[56]; and (3) modifying skin cells to serve as a reservoir to supply some therapeutic protein to the bloodstream, thereby correcting systemic disorders[39]. For these purposes, cutaneous cells can be exogenously modified and engrafted onto the skin. However, this option carries the risk of deleterious host-graft interactions. The use of recombinant viral vectors to modify endogenous skin cells could avoid these issues by rewiring the body's own cellular processes to produce therapeutic agents or repair deficient pathways involved in autoimmune diseases.

Developing treatments for skin diseases and genetic conditions requires the use of *in vitro* and animal models to evaluate the potency of skin-targeted therapies. Despite differences in skin structure and physiology, mouse models remain a critical component in many avenues of cutaneous gene therapy towards clinical trials[75–77]. Mice have been used as models for skin wound repair and regeneration processes and for various skin diseases[57,58,78–80]. Identifying AAV serotypes specific for dominant murine cutaneous cell populations is therefore of high importance. Cultured immortalized cells serve as a critical step in testing, allowing in-depth biochemical and mechanistic studies that are either difficult or impossible in more physiologically advanced models.

Here we have shown that, in model skin cell lines, AAV6 selectively targets mouse keratinocytes, the main cell type of the epidermis, while having low levels of transduction in fibroblasts, which are predominant in the dermis. AAV2, conversely, has high transduction efficiency in fibroblast cells but is minimally infective in keratinocytes. Moving our experiments *in vivo*, we used both intradermal injection and AAV-loaded dMNAs to deliver virus into nude mouse skin. dMNAs were found to be qualitatively superior, eliciting higher apparent rates of transduction due to their more precise delivery into the thin mouse skin, in spite of substantially reduced viral dose. However, in *in vivo* experiments in mice, AAV2 and AAV6 did not show the selectivity that was seen *in vitro*, instead appearing to transduce cutaneous cells relatively promiscuously without any obvious tropism. One potential reason for this observation may be the ineffective targeting of keratinocytes: in mice, the epidermal layer is very thin and the number of keratinocytes is correspondingly very small. Thus, using either intradermal injection or dMNAs, the efficiency of targeting keratinocytes may be too low.

Aside from the potential targeting inefficiency, these results suggest that AAV tropism profiles *in vitro* may be a poor predictor of viral performance *in vivo*[19,45]. AAV serotypes 2 and 6 are good starting points for serotype comparison assays in the skin, in line with the current literature[19,20]. Beyond the capsid proteins that define the viral serotype, other factors known to impact AAV transduction efficiency are the identity and structure of the genome and even the purification method used to isolate the viral particles (which, for commercially-available vectors, may vary from vendor to vendor)[18,81]. Therefore, consistency is key in such assays, as many elements can impact the mechanism of AAV binding and/or infection of cells. In this work, all canonical AAV (1, 2, 5, 6, 8) were obtained from the same vendor, using the same genome.

Both AAV2 and AAV6 showed strong transduction in the skin of a nude mouse, indicating that either serotype is capable of efficiently transducing cutaneous cells for a variety of purposes. Such commonly-available serotypes will be primary research tools until capsid engineering technology becomes more widespread[34,82]. As previously described, capsid engineering strategies have been successful in generating cell type-specific AAV serotypes through cycles of screening and selection. However, this technology remains of limited availability due to its required resources and labor-intensive nature. If commercially-available AAV serotypes could be identified as particularly targetable to mouse keratinocytes and fibroblasts, this would greatly increase the ease and availability of cutaneous cell type-specific AAV-based assays. Additionally, the use of MNAs allowed directed infection of skin cells in our hands, increasing the efficiency and simplicity of intradermal viral delivery without a need for invasive intradermal injections that require trained personnel for reproducible delivery.

Importantly, we have shown that we are able to deliver viruses directly into the cutaneous microenvironment and elicit rapid transgene expression in skin cells. This delivery is targeted to the local area of application, transporting viruses straight to their target cells without the need for exposure to the bulk bloodstream. This increases both the ease and the reproducibility of cutaneous AAV treatment and, in conjunction with highly infective serotypes like AAV2 and

AAV6, may increase bioavailability of the injected vectors by delivering them directly to their target site.

Materials and Methods

Tissue culture and cell lines.

NIH-3T3 mouse fibroblasts (ATCC, Manassas, VA, #CRL-1658) were maintained in Dulbecco's modified Eagle's medium (DMEM) with 4.5 g/L glucose, L-glutamine, and sodium pyruvate (VWR, Radnor, PA), supplemented with 10% fetal bovine serum (ThermoFisher, Waltham, MA)[67]. MPEK-BL6 long-term mouse keratinocytes (CELLnTEC, Bern, Switzerland) were grown in CnT-Prime (CnT-PR) medium (CELLnTEC) and maintained following manufacturer's recommendations. All cells were grown in a humidified incubator at 37°C and 5% CO_2.

Adeno-associated virus production.

The recombinant AAV vectors of serotypes 1, 2, 5, 6, and 8 used in this study were stock viruses produced by the Penn Vector Core in the Gene Therapy Program of the University of Pennsylvania (Penn Core cat. #AV-(1,2,5,6,8)-PV0101). These vectors were produced as previously described[83]. Briefly, HEK293 cells were triple-transfected via calcium phosphate with an AAV rep/cap plasmid (with the cap gene determining the viral serotype), adenovirus helper plasmid (pDF6) and cis-plasmid containing the desired viral genome (pAAV-CMV-PI-eGFP-WPRE-bGH, Penn Core cat. #PL-C-PV0101) flanked by AAV inverted terminal repeat (ITR) sequences[84]. Virus-containing culture medium was collected, concentrated, and purified via iodixanol gradient ultracentrifugation before final concentration and buffer exchange into PBS. Viruses were titered

(GC/mL) using qPCR. AAV-DJ with the same viral genome was produced by the Stanford University Gene Vector and Virus Core.

In vitro transduction experiments, flow cytometry, and statistical analysis.

NIH-3T3 cells

On day 1, NIH-3T3 cells growing in log phase were washed with PBS, lifted with 0.05% trypsin-EDTA (ThermoFisher), and split 10^4 cells/well to 24-well plates in 500µL of DMEM + 10% FBS. Shortly after plating, these cells were transduced with Penn Vector Core's AAV2 and AAV6 vectors described above at viral doses of 2x10^4, 5x10^4, and 1x10^5 viruses/cell (viruses were diluted in PBS immediately prior to addition). Additionally, cells were plated in a negative control well to which no virus was added. Cells were then placed in standard tissue culture conditions for 48 hours.

MPEK-BL6 cells

These cells, which respond more poorly than 3T3s to sparse plating, were washed with PBS and lifted in Accutase (CELLnTEC), then split more densely at 2x10^4 cells to a 48-well plate in 250µL of CnT-PR as previously described for mouse keratinocytes *in vitro*[19]. These cells were treated as described above with AAV2 and AAV6 and then left to incubate for 48 hours.

At approximately 48 hours post-transduction (day 3), both sets of cells were washed with PBS and lifted with either trypsin+EDTA or Accutase. Cells were taken up in fresh growth media and filtered through nylon membranes to eliminate cell clumps. Filtered cells were then analyzed for eGFP expression using the FL1 channel of an Accuri C6 flow cytometer (BD Biosciences, San Jose, CA). This channel used a 488 nm laser for excitation with a 533/30 nm bandpass filter to collect emission. For 3T3 cells, 20000 total events were collected; for MPEKs, between 7500 and 10000. Data was initially collected in ForeCyt software (IntelliCyt, Albuquerque, NM) and then analyzed using FlowJo ver. 10.2 (FlowJo LLC, Ashland, OR). Briefly, 3T3 and MPEK cells were gated on plots of SSC-A vs. FSC-A to isolate cell populations, then FSC-H vs. FSC-A to conduct doublet exclusion. Cells were then plotted as SSC-A vs. FL1-A. The negative control sample for each experiment was used to define the range of untransduced cells on this plot, with the percentage of events falling outside this range usually <1% for the negative controls. This gate was applied to all other samples to determine the percentage of events with stronger FL1 signal than the negative control (Figure 1-S1). The percentage of outliers in the negative control sample was subtracted from this number to generate the final percentage of AAV-infected, eGFP-expressing cells in each sample.

For the broad comparison of AAV serotype transduction efficiencies at 10,000 vp/cell (shown in Figures 1-4 and -5), the above protocol was followed except that 3T3 and MPEK cells were plated and transduced on an optical-bottom 96-well plate (Greiner Bio-One, Gremsmünster, Austria) at 1.7x10^3 and 6.8x10^3 cells/well, respectively.

For statistical analysis, quantitative data was subjected to Analysis of Variance (ANOVA) followed by Tukey’s HSD post hoc test using Systat (SYSTAT Software, Inc., Chicago, IL). The results of the initial test of AAV infectivity in 3T3 and MPEK cells at a viral dose of 10,000 GC/cell (Figure 1-4) were subjected to an ANOVA with Tukey's HSD post hoc test (Table 1-S1) to determine significant differences in infectivity for specific serotypes between cell lines. Results of the titration curves for AAV2 and AAV6 in these cells (Figure 1-6) were analyzed in the same fashion and are shown in S2-S3 Tables.

Fluorescence microscopy on cultured cells.

Confocal fluorescence microscopy on AAV-transduced NIH-3T3 and MPEK-BL6 cells was performed using an Andor Revolution XD System with Spinning Disk (Andor Technology, Belfast, UK) with a 20X dry plan apochromat objective (NA = 0.8). A solid state 488 nm laser line was used to excite eGFP with a 525/25 nm bandpass filter to collect emission. Imaging data were collected using Andor iQ3 software and analyzed with ImageJ, an image analysis software package developed at the NIH[85].

Fabrication of dissolvable microneedle arrays with viral cargo.

Dissolvable MNAs with obelisk-shaped microneedles were manufactured from a water-soluble biomaterial combination (carboxymethylcellulose, CMC and Trehalose, Treh) using a fabrication strategy previously described[71]. Briefly, the microneedle master molds were created from poly(methyl methacrylate) through micromilling. The master molds were used to fabricate production molds from polydimethylsiloxane (PDMS) through micromolding. Dissolvable MNAs with embedded AAV vectors were produced through spin-casting. First, hydrogel form of the MNA material was prepared by dissolving CMC (Sigma-Aldrich, St Louis, MO, cat. #C5678) and Trehalose (Sigma-Aldrich, cat. #T9531) powders in liquid virus solution containing the desired number of AAV vectors to achieve 20% final solute concentration. The final MNA material was 60% CMC/40% Treh. Subsequently, 15 µl of the prepared hydrogel containing the AAV vectors was dispensed over each of the PDMS molds and spin-dried for 2 hours at 3500 rpm, 10°C to fill the obelisk-shaped cavities of the PDMS mold. Finally, 50 µl of 20% CMC hydrogel without any viral cargo was dispensed over the PDMS molds and spin-dried for 5 hours at 3500 rpm, 10°C to form the backing layer of MNAs, thereby obtaining final dissolvable MNAs with AAV vectors.

In vivo experiments and statistical analysis.

Three nude mice (Harlan, Indianapolis, IN) were anesthetized via isoflurane inhalation. AAV2- and AAV6-CMV-eGFP were intradermally administered by injecting 10µL ($1.3\text{x}10^{10}$ vp/injection of both serotypes) of purified virus into the skin. Application of AAV-loaded dMNAs ($3.1\ \text{x}10^{9}$ vp/MNA for both serotypes) was performed by using a spring-loaded applicator. Then tape was applied to cover the MNA and gentle thumb pressure placed for 20 minutes post-application to ensure optimal dissolution of needles and delivery of viral cargo. Tape was left in place for an additional 10 minutes before dMNAs were removed for visual analysis and optical microscopy. Baseline images were taken using an IVIS Spectrum CT imaging system (Caliper Life Sciences, Waltham, MA) set to image at excitation/emission of 465/520 nm, capturing background autofluorescence in the range of eGFP expression. Three days post-injection, mice were again imaged using the same settings on the IVIS imaging system. After imaging, mice were euthanized via CO_2 inhalation and cervical dislocation, after which the dorsal skin was removed for further analysis. Viral injection sites (location of eGFP-expressing cells) were excised and prepared for histology. The prepared skin samples were cryo-sectioned into 10 μm thick cross-sections. The sectioned skin samples were counter-stained using DAPI fluorescent dye. The stained sections were then imaged using a Nikon epifluorescent microscope with a 40X objective to detect the eGFP expressing skin cells. All animal research was performed under the purview of the Institutional Animal Care and Use Committee (IACUC) of Carnegie Mellon University.

For statistical analysis, a one-way ANOVA was performed on the radiant efficiency data shown in Figure 1-S2, followed by Tukey's multiple comparisons test using GraphPad Prism 6.01 (GraphPad Software, Inc., La Jolla, CA). These results are shown in Table 1-S4.

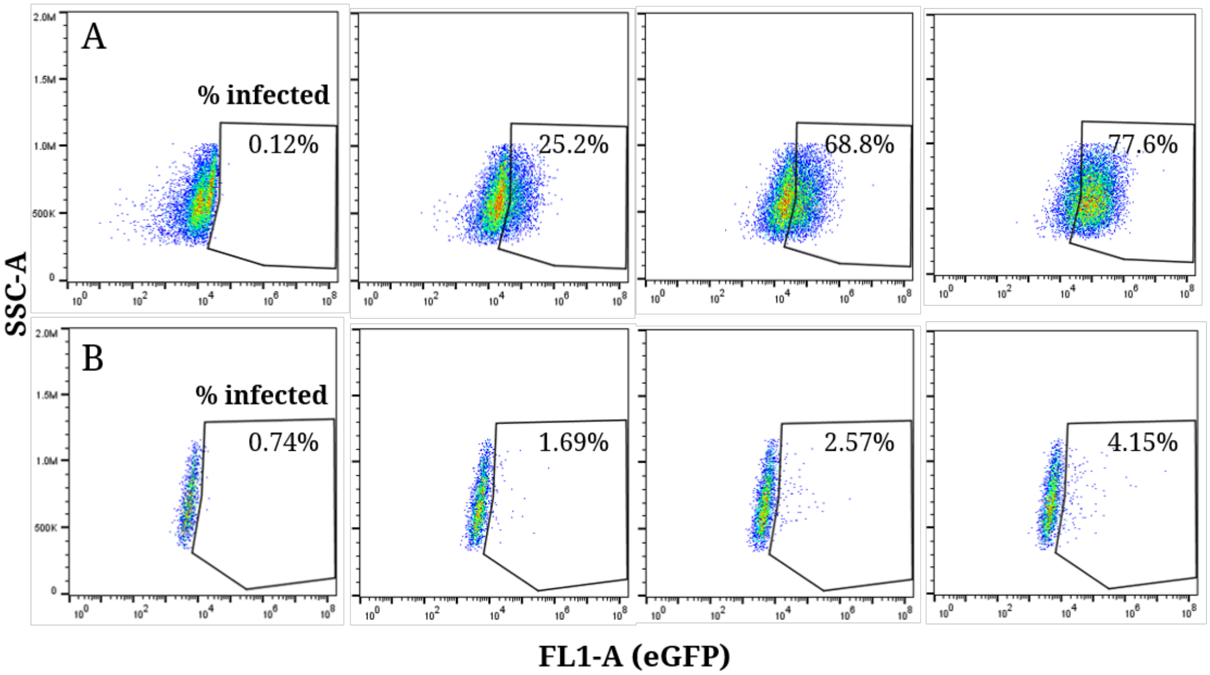

Figure 1-S1. Representative dot plots and gating from flow cytometry analyses shown in Figure 1-6. (**A**) 3T3 fibroblasts and (**B**) MPEK keratinocytes. For both cell types, data is shown from cells untransduced (first column) or transduced with AAV2-CMV-eGFP at a viral dose of 5,000 (second column), 20,000 (third column), or 100,000 (fourth column) GC/cell. Gates shown were used to identify eGFP-expressing cells and the % negative control was subtracted from the experimental numbers to arrive at final values.

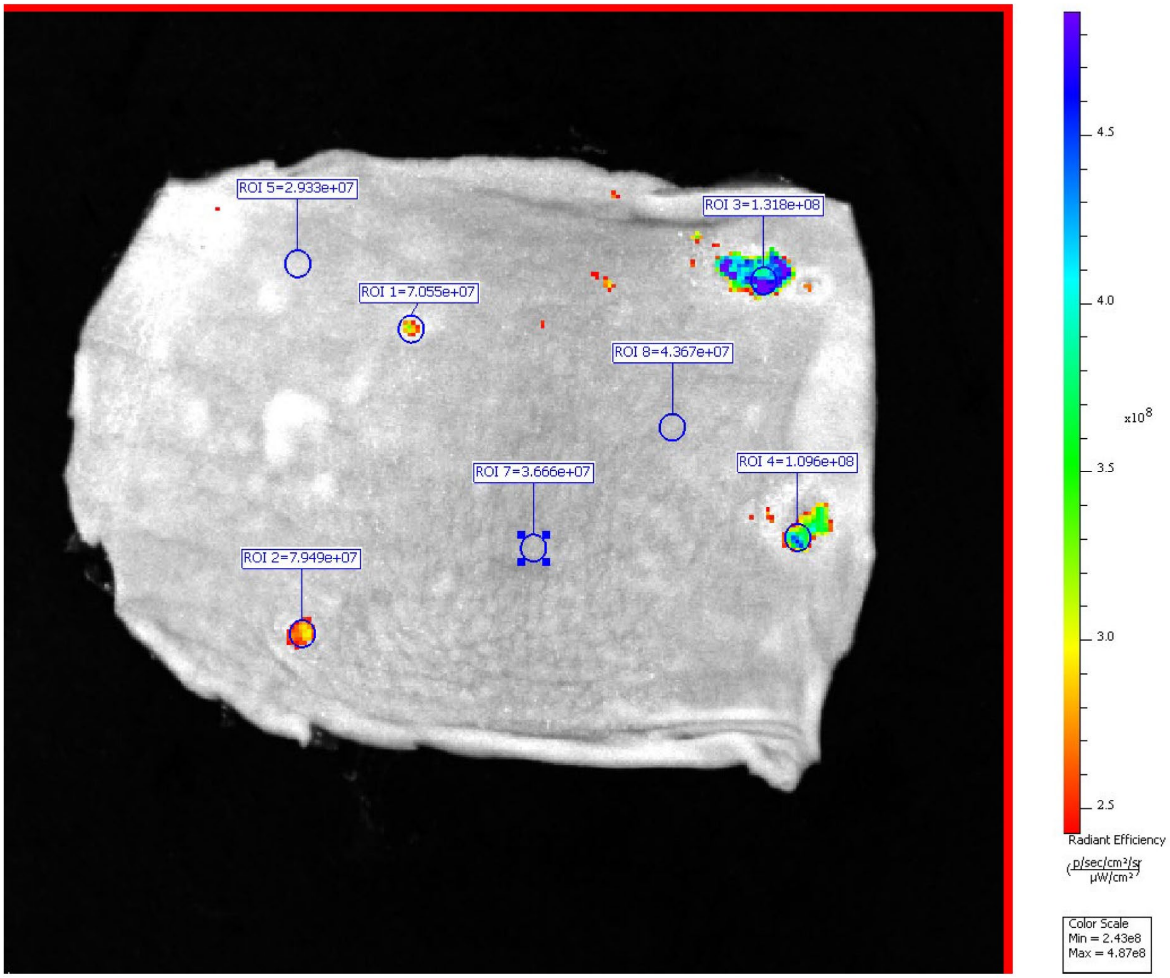
ROI 5=2.933e+07
ROI 3=1.318e+08
ROI 1=7.055e+07
ROI 8=4.367e+07
ROI 4=1.096e+08
ROI 7=3.666e+07
ROI 2=7.949e+07
4.5
4.0
x10^8
3.5
3.0
2.5
Radiant Efficiency
(p/sec/cm²/sr / µW/cm²)
Color Scale
Min = 2.43e8
Max = 4.87e8

Figure 1-S2. Raw data from post-processing of in vivo images shown in Figure 1-7 using IVIS Spectrum CT software. Three background locations (ROIs) were selected at random to compare against two ID injection sites and two dMNA application sites of equal area. Data shown are radiant efficiency with color scale bar on the right.

Table 1-S1. Statistical analyses of AAV infectivity comparison data shown in Figure 1-4.

Analysis of Variance					
Source	**Type III SS**	**df**	**Mean Squares**	**F-Ratio**	**p-Value**
Cell	17.989	1	17.989	8.761	0.007
Serotype	778.527	5	155.705	75.828	<0.001
Cell*Serotype	1,264.498	5	252.900	123.161	<0.001
Error	49.282	24	2.053		

Tukey’s Honestly-Significant-Difference Post Hoc Test				
3T3 vs. MPEK*Serotype	**Difference**	**p-Value**	**95% Confidence Interval**	
			Lower	**Upper**
AAV1	0.323	1.000	-3.895	4.542
AAV2	18.603	<0.001	14.385	22.822
AAV5	-0.199	1.000	-4.418	4.020
AAV6	-21.893	<0.001	-26.112	-17.675
AAV8	0.220	1.000	-3.999	4.439
AAV-DJ	-5.625	0.006	-10.100	-1.150

Table 1-S2. Statistical analyses of AAV2 titration curves shown in Figure 1-6A.

<table>
<tr><th colspan="6">Analysis of Variance</th></tr>
<tr><th>Source</th><th>Type III SS</th><th>df</th><th>Mean Squares</th><th>F-Ratio</th><th>p-Value</th></tr>
<tr><td>Cell</td><td>31,855.263</td><td>1</td><td>31,855.263</td><td>4,390.056</td><td><0.001</td></tr>
<tr><td>Viral Dose</td><td>5,857.310</td><td>3</td><td>1,952.437</td><td>269.070</td><td><0.001</td></tr>
<tr><td>Cell*Viral Dose</td><td>4,566.216</td><td>3</td><td>1,522.072</td><td>209.761</td><td><0.001</td></tr>
<tr><td>Error</td><td>377.324</td><td>52</td><td>7.256</td><td></td><td></td></tr>
<tr><th colspan="6">Tukey’s Honestly-Significant-Difference Post Hoc Test</th></tr>
<tr><th colspan="2">3T3 vs. MPEK*Viral Dose</th><th>Difference</th><th>p-Value</th><th colspan="2">95% Confidence Interval</th></tr>
<tr><th colspan="2"></th><th></th><th></th><th>Lower</th><th>Upper</th></tr>
<tr><td colspan="2">10,000 GC/cell</td><td>18.603</td><td><0.001</td><td>11.659</td><td>25.548</td></tr>
<tr><td colspan="2">20,000 GC/cell</td><td>46.692</td><td><0.001</td><td>42.683</td><td>50.702</td></tr>
<tr><td colspan="2">50,000 GC/cell</td><td>64.826</td><td><0.001</td><td>60.816</td><td>68.835</td></tr>
<tr><td colspan="2">100,000 GC/cell</td><td>75.970</td><td><0.001</td><td>71.961</td><td>79.890</td></tr>
</table>

Table 1-S3. Statistical analyses of AAV6 titration curves shown in Figure 1-6B.

Analysis of Variance					
Source	**Type III SS**	**df**	**Mean Squares**	**F-Ratio**	**p-Value**
Cell	41,002.286	1	41,002.286	1,219.143	<0.001
Viral Dose	7,276.487	3	2,575.496	76.579	<0.001
Cell*Viral Dose	4,228.438	3	1,409.479	41.909	<0.001
Error	1,748.867	52	33.632		

Tukey’s Honestly-Significant-Difference Post Hoc Test				
3T3 vs. MPEK*Viral Dose	**Difference**	**p-Value**	**95% Confidence Interval**	
			Lower	**Upper**
10,000 GC/cell	-21.893	0.001	-36.845	-6.942
20,000 GC/cell	-58.504	<0.001	-67.137	-49.872
50,000 GC/cell	-78.416	<0.001	-87.048	-69.783
100,000 GC/cell	-75.002	<0.001	-83.634	-66.370

Table 1-S4. Statistical analysis of *in vivo* data shown in Figures 1-7C and -7D.

Analysis of Variance					
Source	**SS**	**df**	**Mean Squares**	**F-Ratio**	**p-Value**
Between Columns	8.53x10^{15}	2	4.265 x10^{15}	43.83	0.0019
Within Columns	3.892 x10^{14}	4	9.730 x10^{15}		
Total	8.919 x10^{15}	6			

Tukey's Multiple Comparisons Test				
Comparison	**Difference**	**p-Value**	**95% Confidence Interval**	
			Lower	**Upper**
Background vs. ID	-3.847x10^{7}	<0.05	-7.056x10^{7}	-6.374 x10^{6}
Background vs. dMNA	-8.415 x10^{7}	<0.005	-1.162 x10^{8}	-5.205 x10^{7}
ID vs. dMNA	-4.568 x10^{7}	<0.05	-8.084 x10^{7}	-1.052 x10^{7}

Chapter 2 – Development and Validation of AAV Drivers of Inflammation-responsive Fluorescence *In Vitro* and *In Vivo*

Introduction

Clinical monitoring of the status of patients receiving immunotherapies is usually limited in scope, relying on general clinical presentation and other effects that can only be indirectly inferred and are commonly modified by interactions with non-therapeutic drivers. Additionally, immunotherapies can fail before they are observable through changes in symptoms, necessitating more accurate and timely technologies for measuring inflammation-linked biomarkers[7–9,13,14]. Such a technology should be modular, precise, and patient-specific to allow the coverage of as wide an array of biomarkers as possible across a diverse clinical population.

The current gold standards for clinical assays of anti-inflammatory therapeutic efficiency include radioimmunoassays, ELISAs, and electrophoretic mobility shift assays[8]. These measure the levels of a particular biomarker or therapeutic in the blood and have shown a high level of precision in managing immunotherapies. However, these assays suffer from a number of unavoidable problems, including lack of information on the target's bioactivity, complications from anti-drug antibodies (in the case of therapeutic measurements), and lengthy sample preparation and analysis times[8–10] – a substantial issue, as many cytokines have short half-lives in the blood (and may degrade in a sample even as it is being prepped for analysis[9]) and important signaling events may take place in the interval between blood collections. Other inflammation-monitoring approaches in development are either subject to similar limitations (e.g. high-throughput microfluidic assays or aptamer-based ELISA-like technologies) or are not amenable to repeated measurement (e.g. interstitial cutaneous microdialysis).

The biotattoo technology (Figure 1-1) is designed to address many of these concerns by (1) providing real-time, noninvasive readout on the bioactivity of therapeutics *in vivo*, (2) circumventing anti-drug antibodies and other complications by reporting directly on cellular signaling pathways, and (3) allowing repeated analysis over time as opposed to snapshots of inflammatory activity at a given moment of measurement. The use of transcription factor reporters to monitor intracellular bioactivity is well-established *in vitro* for many cytokine-linked signal transduction pathways[86], and deploying such a technology using adeno-associated virus vectors *in vivo* could allow the measurement of multiple inflammatory pathways in real time.

Central to the biotattoo project is the construction and validation of inflammation-responsive DNA reporter elements capable of being delivered to living cells by AAV. The core of such a reporter element will be the gene for a reporter (e.g. a fluorescent or luminescent protein) linked to and driven by a binding site for an inflammatory transcription factor. Activation and binding of this factor will upregulate production of the protein and lead to measurable signal through the skin (Figure 1-2).

Among the most biologically significant of the inflammatory transcription factors is nuclear factor κB. NFκB is a dimeric transcription factor activated by a wide array of pro-inflammatory stimuli, including various cytokines, pathogenic antigens, and UV radiation[87]. Signaling pathways activated by NFκB interact with numerous other inflammatory transcription factors and influence nearly every aspect of cellular homeostasis[88]. NFκB activity is particularly important in autoimmune disorders such as rheumatoid arthritis[89], and several anti-arthritic therapies are designed to inhibit its activity[90].

Plasmids containing NFκB reporter elements are widely commercially available for *in vitro* assays, but such reporters are rarely found in a format amenable to viral packaging – particularly for the stringent size and organization requirements of an AAV genome. AAV is capable of packaging a genome with a maximum size of ~five thousand basepairs (5 kb), a size much smaller than that of most other viral vectors and one routinely exceeded by reporter plasmids. Therefore, the design and production of an AAV-compatible NFκB sensor genome was a crucial first step, along with its testing in an *in vitro* format to confirm inflammatory responsiveness and signal generation. Following this, we produced viral vectors carrying our genome and tested them in living animal models. Constitutive control and inflammation-responsive virus drivers were deployed *in vivo* to test both the suitability of AAV vectors for repeated use in living skin and the ability of our NFκB reporter to drive real-time responsive signal. Together, our results show the feasibility of the AAV-based biotattoo technology while cautioning against the use of fluorescent reporters due to the difficulty of distinguishing low levels of signal from tissue autofluorescence.

Results

Construction and *in vitro* testing of NF-κB-responsive AAV genome.

Transcription factor reporter plasmids are commonly commercially available for a range of biologically relevant processes. Cloning an AAV genome presents the unique difficulty, however, of strictly limiting size to >5kb[91]. Based on recently-published results showing the feasibility of AAV-based inflammation sensors[23,24], we constructed our NF-κB-responsive genome to drive fluorescent protein production in response to transcription factor binding.

Figure 2-1 shows a schematic of this construct, pAAV-4xNFkB-mCherry-PEST. This plasmid contains an NF-κB-responsive cassette flanked by inverted terminal repeats (ITRs), which define the DNA that is cut out and inserted into viral particles during AAV production. Our cassette includes four consecutive copies of the consensus NF-κB binding sequence, GGGACTTTCC[92], followed by the minimal thymidine kinase promoter. This promoter is a commonly-used element that is too weak to recruit transcriptional machinery without activation by a nearby enhancer (in this case, the NF-κB binding sites)[24]. Preceding these elements is a synthetic polyA/transcriptional pause site designed to dampen nonspecific promoter activity from the left ITR, which has been observed *in vitro*[62]. Together, these elements should drive robust production of fluorescent protein only in the presence of activated NF-κB.

Our chosen fluorescent protein was mCherry, as its red emission wavelength is more able than commonly-used greener proteins to penetrate through skin tissue *in vivo*[93]. Finally, the mCherry was linked to a PEST sequence, a degradation-enhancing element isolated from the mouse ornithine decarboxylase enzyme. This sequence has been found to dramatically decrease protein half-life *in vitro*[94,95], allowing typically long-lived fluorescent proteins to degrade more rapidly in response to changes in inflammatory dynamics.

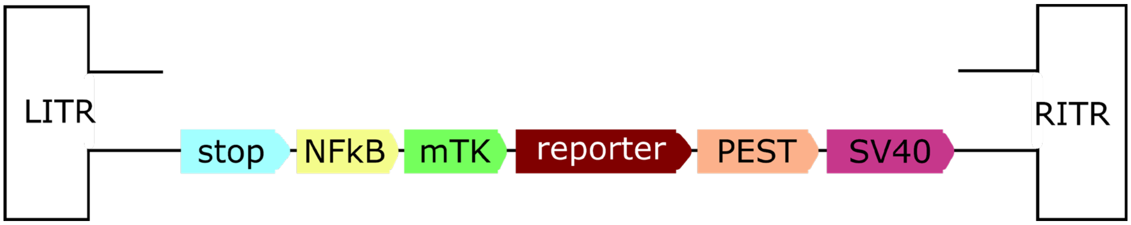

Figure 2-1. Inflammation-responsive transgene that drives reporter protein production in response to NF-κB activation. As in Figure 1-3, this transgene is encoded by a cis-plasmid that is delivered to virus-producing cells AAV production and is encapsulated within viral particles as single-stranded DNA flanked by the inverted terminal repeats (ITRs). The core elements of this genome are as follows: stop = transcriptional pause site to block nonspecific promoter activity from the left ITR. NFkB = four copies of the NF-κB consensus binding site (GGGACTTTCC). mTK = minimal thymidine kinase promoter. reporter = customizable reporter protein (our variants included the yellow fluorescent protein SYFP2 and the red mCherry). PEST = degradation-enhancing sequence derived from mouse ornithine decarboxylase enzyme. SV40 = viral poly(A) element.

Following large-scale production of pAAV-4xNFkB-mCherry-PEST, we tested the construct *in vitro* prior to proceeding with recombinant AAV production. We transiently transfected the AAV genome plasmid into HEK-293 cells, a control cell line that is commonly used due to its versatility and high transfectability. After giving the cells time to begin expressing the inflammation-responsive construct, half of the cells were treated with 100ng/mL of recombinant human tumor necrosis factor alpha (TNFα), a potent proinflammatory cytokine and canonical activator of NF-κB signaling pathways. Cells were left to incubate with the cytokine for 5 hours, in line with previous measurements of *in vitro* inflammatory signaling, before epifluorescence microscopy to assay for expression of NF-κB-responsive mCherry. These results are shown in Figure 1-2. Low levels of mCherry production were observed in untreated cells, owing most likely to (1) leaky promoter activity and (2) constitutive low-level signaling from NF-κB pathways. This expression level increased dramatically in cells exposed to TNFα, where significant production of mCherry was observed (Figure 1-2B).

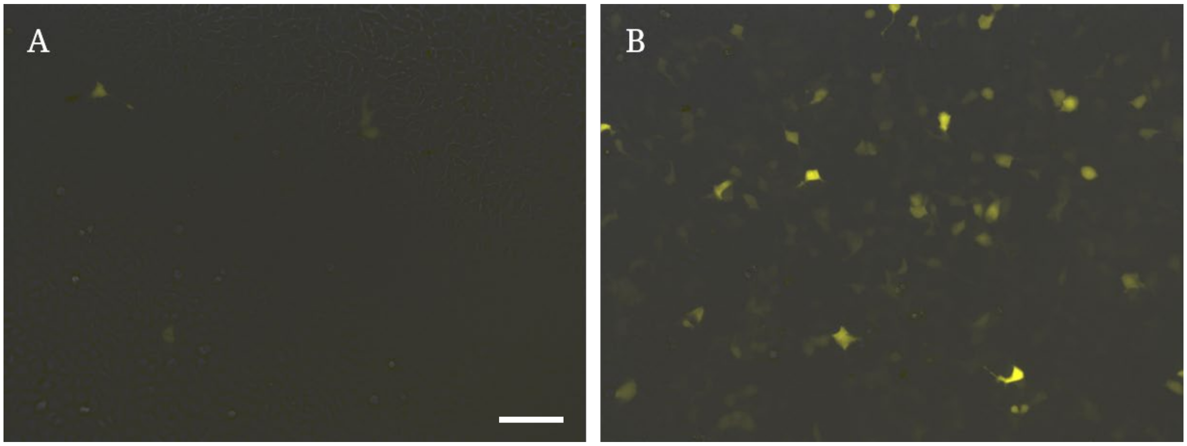

Figure 2-2. HEK-293 cells transfected with pAAV-4xNFkB-mCherry-PEST express inflammatory signaling-dependent fluorescent protein. Cells in B were treated with 100ng/mL of TNFα for 5 hours prior to imaging, while cells in A were treated with an equivalent volume of PBS (vehicle control). Scale bar = approx. 100 μm.

In vivo testing of fluorescent and luminescent AAV-based NF-κB reporters.

With the NF-κB reporter AAV genome exhibiting inflammation-responsive signal *in vitro*, we packaged our construct into viral particles for testing *in vivo*. We chose AAV8 as the serotype for our prototype NF-κB reporters, as previous results had shown this serotype to exhibit the highest infectivity out of a panel of common commercially-available AAV serotypes when intradermally injected into rat skin (Figure 2-S1). Additionally, a control counterpart to this virus was also produced (AAV8-CMV-mCherry-PEST). This virus contains a genome with mCherry, our chosen fluorescent reporter protein, driven by the constitutively active cytomegalovirus (CMV) promoter, leading to lasting high-level expression against which our inflammation-reporter can be normalized and compared.

These viruses were injected into the skin of a hairless rat. Rats are a commonly-used animal model for studies of skin bioactivity and wound healing, as they combine the advantages of mice (ready obtainability and large body of available research) with a larger and more human-like skin physiology. The hairless rat, a strain frequently used for immunology and oncology studies[96,97], was used to increase fluorescence visibility through the skin and avoid the need for abrasive shaving or proinflammatory chemical hair removal prior to virus treatment.

To test the efficacy of our viral constructs *in vivo*, we injected intradermally injected the back of a hairless rat in two locations with either AAV8-CMV-mCherry-PEST, our constitutive control vector, or the inflammation-responsive

AAV8-4xNFkB-mCherry-PEST construct. Forty-eight hours post-injection, the rat was injected with 5mg/kg of lipopolysaccharide (LPS), a broad-spectrum inflammatory stimulator encountered *in vivo* as a component of bacterial cell walls. Thereafter, the rat was monitored for several hours to assay for expression of fluorescent reporter protein at the site of injection with our NF-κB reporter virus. Results from this experiment are shown in Figure 2-3. Although high expression was observed from the constitutive control virus, no fluorescent signal was seen at the site of inflammation-reporter expression. Similar results were obtained from subsequent experiments in multiple rats using varying doses of LPS or local injections of TNFα to stimulate reporter expression.

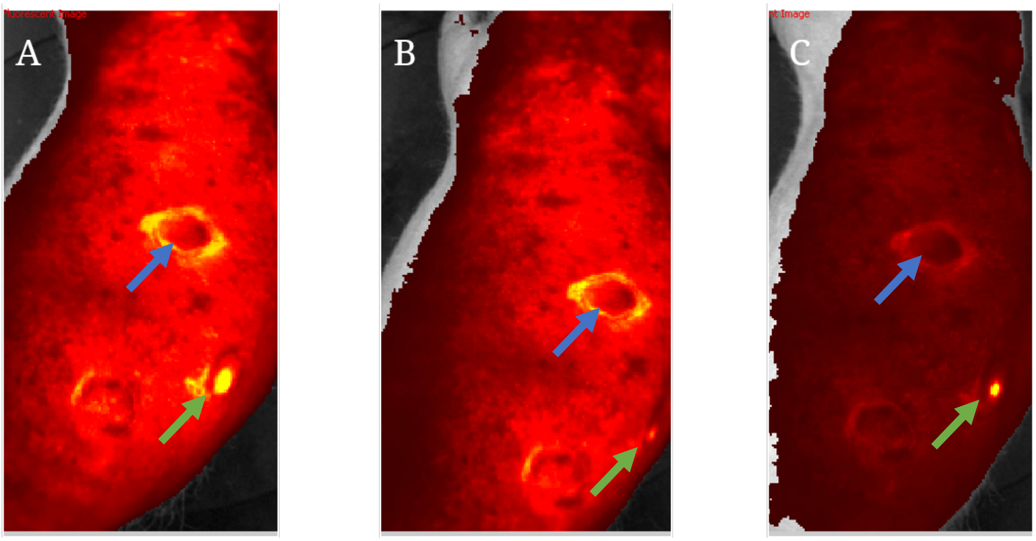

Figure 2-3. AAV inflammation sensors do not drive measurable reporter production when fluorescent proteins are used. A, B, and C show the back of a rat injected with either AAV8-4xNFkB-mCherry (top, blue arrow) or an AAV8 constitutive control vector also driving mCherry production (bottom, green arrow). Shown are timepoints 2 hours (A), 4 hours (B), and 6 hours (C) after injection with proinflammatory LPS. Bright circle around inflammation reporter injection is autofluorescence from materials in ink used to mark the site.

The most likely reason for the lack of responsive signal in Figure 2-3 is a combination of properties of biological tissue that routinely stymie fluorescent assays *in vivo*: scattering of emitted light, absorption by the tissues, and background autofluorescence from proteins in the skin and deeper organs[98–100]. Based on these results, we decided to switch reporter proteins, moving from the fluorescent mCherry to the luminescent luciferase.

Luciferases are a family of bioluminescent oxidative enzymes derived from several species of insects, aquatic organisms, and bacteria. Compared to fluorescent protein reporters, luciferase has the important limitation of requiring a substrate (luciferin or coelenterazine, depending on the type of luciferase used) upon which the enzyme acts to produce light. However, it has distinct advantages that make it an attractive replacement for fluorescent proteins when autofluorescence presents problems. There is no luminescent counterpart to autofluorescence, and the light produced by luciferase therefore has little to no biological background. This allows for extremely accurate and precise measurements even through many layers of tissue[101]. Additionally, luciferase has a naturally short half-life and does not need a degradation-enhancing PEST element in order to bring its reporter lifetime in line with inflammatory kinetics[102].

Previous research has been published on the viability of AAV-based luminescent inflammation reporters *in vivo*. Most compellingly, recent results from the Husain lab at the Children’s Hospital of Pittsburgh demonstrated successful use of an AAV6-based luminescent sensor of NF-κB activation to monitor inflammation in a mouse model of pancreatitis[23]. We obtained the Husain lab's AAV6-NFkB-luciferase vector in order to test it in rat skin in place of our fluorescence-based vectors. Although we had previously had little success with AAV6 transduction of rat skin cells (Figure 2-S1), we believed that the enhanced signal-to-noise ratio of luminescence over fluorescence (roughly three orders of magnitude *in vivo*[101]) would allow signal to be observed from relatively few transduced cells.

To test these vectors *in vivo*, we followed the same protocol developed for the fluorescent vectors: intradermal injection of a hairless rat in two locations with either AAV6-NFkB-luciferase or AAV6-CMV-luciferase (a constitutive control vector). Forty-eight hours after injection, the rat was injected with 5mg/kg of LPS. The rat was then imaged at following timepoints to determine expression levels of the control and inflammation-responsive constructs. These results are shown in Figure 2-4. Figure 2-4A shows positive expression of the constitutive control construct, while B-D show the NF-κB reporter. Reporter signal was observed to increase to ~8.5-fold above baseline levels four hours after inflammatory stimulation via LPS, decreasing to ~5.5-fold at 6.5 hours post-stimulation.

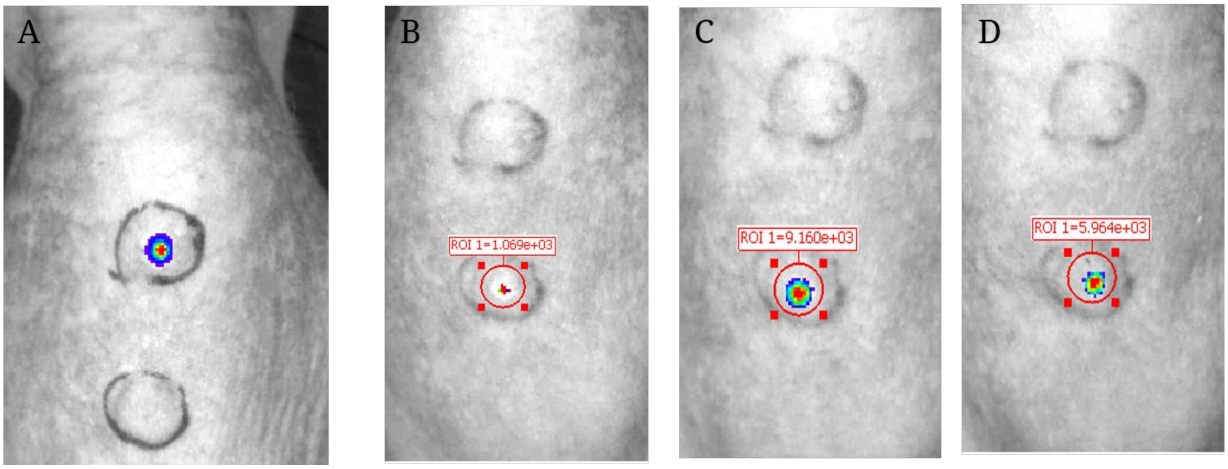

Figure 2-4. AAV-based luminescent reporters drive inflammation-responsive signal in living rat skin. (A) shows a rat injected with a luminescent control vector, AAV6-CMV-luc. B, C, and D show the same rat injected with inflammation-responsive vector, AAV6-NFkB-luc, at 0 (B), 4 (C), and 6.5 (D) hours post-injection with proinflammatory LPS. Numbers shown are luminescent signal intensity in arbitrary units. For all images, luciferin was locally injected at expression sites to allow luminescence (constitutive control site in A; inflammation reporter site in B-D).

Discussion

Disorders of the immune system are a complex and diverse target for physicians and drug developers. Their effects in the body can be devastating and far-reaching, often serving as the precursors to cancers or heart disease[103], and their prevalence in Western society has been estimated at 5-7% of the total population[104]. Meanwhile, the diversity of the immune system leads to significant patient-to-patient variability in disease mechanisms, progression, and responsiveness to treatment. As personalized medicine moves to the forefront of clinical research, it is important that we develop the technologies needed to confront inflammatory diseases effectively in ways that are attuned to patients' specific biology.

The goal of our research was to begin the development of a prototype inflammation reporter that is directly linked to the activity of a patient's own cells. By directly monitoring transcription factor activity, we circumvent many of the problems inherent to *ex vivo* assays while receiving information that is itself more physiologically relevant. The biotattoo technology could therefore provide a new means for efficient, personalized monitoring of inflammatory disease progression, immune gene networks, and therapeutic efficacy.

The data shown here demonstrate the viability of the crucial first steps of this technology. We have shown that intradermal injections of adeno-associated virus lead to localized transduction of small patches of skin cells at the site of injection, and that these cells can be induced to express reporter protein in a time-dependent manner after the induction of a general inflammatory response.

Ideally, a complete biotattoo system would be able to report on multiple inflammatory pathways in real time, and the results shown here support the feasibility of this outcome after further development.

The failure of fluorescent inflammation reporters to produce visible signal through the skin was significant. There are a number of potential avenues toward solving this problem. The first is simply to replace fluorescent proteins with luciferase in all future experiments. This, as illustrated in the difference between Figures 2-3 and 2-4, dramatically increases signal-to-noise ratio by eliminating background signal from the animal. However, the requirement of an added substrate (e.g. luciferin) for signal generation is problematic, as it introduces a source of potential application error and reduces the system's real-time responsiveness by linking signal generation to the kinetic curve of the luciferin/luciferase reaction[102].

Another possible solution is to simply maximize signal from our fluorescent reporters, for instance by (1) optimizing the NF-κB-responsive cassette by using stronger induction elements (e.g. more NF-κB binding sites or a stronger minimal promoter); (2) using a further-red fluorescent protein (e.g. a near-infrared [NIR] protein) as our reporter. There is less and less autofluorescence from biological tissues at longer and longer wavelengths[105]. However, NIR fluorescent proteins tend to be dimmer and less photoefficient than their shorter-wavelength counterparts[99]. Therefore, convergent technology development would be required to make this option feasible.

Finally, a change in viral vector may serve to increase visible reporter signal through the skin. Adeno-associated virus was used in this study due to its attractive clinical properties, including low immunogenicity and lack of genomic integration. However, its relative infectivity is generally lower than that of other commonly used research viruses like adenovirus or lentivirus[106,107]. Swapping viral vectors would not only increase the available cloning space, giving more room to include expression-enhancing genetic elements, but could also significantly increase the number and intensity of expressing cells in the skin. Any such change would have to be carefully balanced against the potential problems of increasing immunogenicity or risk of insertional mutagenesis in transduced cells.

Materials and Methods

NFκB-responsive AAV genome production.

Our prototype NF-κB-responsive AAV genome (pAAV-4xNFkB-mCherry-PEST) was built from pAAV-MCS, a basic cloning vector from Cell Biolabs (San Diego, CA, cat. #VPK-410). We constructed our NF-κB-responsive cassette in a separate control vector (pSB1C3) for ease of cloning, as AAV genomes frequently recombine during routine cloning due to the GC-richness and hairpin structure of the ITRs. We inserted this cassette into pAAV-MCS via a double digest using Thermo Scientific FastDigest BamHI and BglII (cat. #s FD0054 and FD0083), following manufacturer protocols. After ligation, the product was transformed into Stbl2 cells (ThermoFisher cat. #10268019), a strain of *E. coli* suitable for cloning of difficult plasmids with high potential for recombination. The resulting AAV genome plasmid was sent to Alta Biotech for large-scale DNA production.

In vitro testing of NFκB-responsive AAV genome.

To test the activity and inflammation-responsiveness of our AAV genome prior to viral packaging, 2.5 μg of pAAV-4xNFkB-mCherry-PEST were transfected into HEK-293 cells (ATCC #CRL-1573). These cells were grown on glass-bottom MatTek dishes in DMEM with 4.5 g/L glucose, L-glutamine, and sodium pyruvate, supplemented with 10% FBS, and the transfection reagent was Xfect (Takara Bio, Shiga, Japan, cat. #631318). Forty-eight hours post-transfection, one dish per construct was treated with 100ng/mL of recombinant human TNFα (Peprotech, Rocky Hill, NJ, cat. #300-01A), while the other was treated with vehicle control.

The dishes were incubated at 37°C, 5% CO_2 for a further five hours before imaging on an EVOS Cell Imaging System epifluorescence microscope (ThermoFisher) using an RFP light cube to visualize mCherry fluorescence.

Recombinant AAV vectors.

Constitutive control vectors of serotype 8 were purchased from the University of Pennsylvania Vector Core (cat. #AV-6-PV0101 [eGFP] and #AV-6-PV2177 [TurboRFP]). The protocol for production of these vectors was previously described by the Watson lab[83]. Briefly, these vectors were manufactured through transfection of producer cells (i.e., HEK-293 cells) with three plasmids: (1) AAV cis-plasmid composed of the desired viral genome (pAAV-CMV-PI-eGFP-WPRE-bGH or pAAV-CMV-TurboRFP-WPRE.rBG) flanked by AAV inverted terminal repeat (ITR) sequences, (2) AAV trans-plasmid containing AAV rep and cap genes (the cap gene determines the AAV serotype), and (3) adenovirus helper plasmid (pDF6). These single-stranded DNA viruses encoded the gene for a widely-used green fluorescent protein (eGFP), driven by the strong, constitutively-active cytomegalovirus (CMV) promoter. The culture medium containing the viral vectors was collected, concentrated using flow filtration, and purified by iodixanol gradient ultracentrifugation prior to final concentration and buffer exchange. The produced recombinant viruses were then titered (GC/mL) using quantitative polymerase chain reaction (qPCR) and stored at -80°C until use.

Fluorescent NFκB-responsive and constitutive control AAV8 was produced by custom large-scale order from Vector Biolabs (Malvern, PA, service ID #70200).

This virus was produced in similar fashion to the control viruses from the Penn Vector Core, with our custom recombinant genomes used in place of a control plasmid. After receipt, viruses were aliquoted and stored at -80°C.

Luminescent NF-κB-responsive AAV6 (AAV6-NFkB-luc) was generously provided by Dr. Sohail Husain at Children's Hospital of Pittsburgh (Pitt MTA #00002826). Constitutive luminescent control AAV6 (AAV6-CMV-luciferase) was purchased from the Vector Core at the University of North Carolina, Chapel Hill.

In vivo testing of control and inflammation-responsive AAV.

Hairless rats (Harlan, Indianapolis, IN) were anesthetized via isoflurane inhalation. AAV vectors were intradermally administered by injecting 10uL (approximately 10^{10} viral particles of AAV6-CMV- and -NFkB-luciferase and 10^{11} of all other viruses used) into the skin. Baseline images were taken using an IVIS Spectrum CT imaging system (Caliper Life Sciences) set to image at excitation emission of 465/520 nm (eGFP) or 570/620 nm (mCherry). Standard luminescence imaging settings with an exposure time of 10 seconds were used for luciferase assays. Two to three days post-injection, rats were imaged again using the same settings on the IVIS system. To stimulate inflammation reporter signal, mice were treated via tail vein injection with 5 mg/kg of LPS and timepoint imaging was conducted to monitor reporter signal over time. For luminescence production at luciferase virus injection sites, D-luciferin was locally injected (~21 μg/injection; Promega, Madison, WI, cat. #P1041) ten minutes prior to imaging.

All animal research was performed under the purview of the Institutional Animal Care and Use Committee (IACUC) of Carnegie Mellon University.

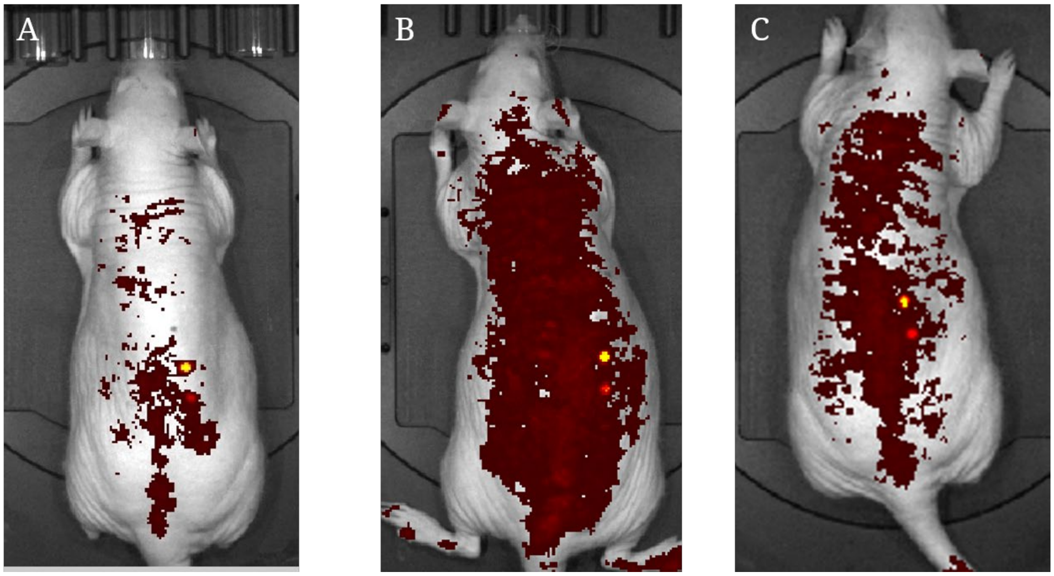

Figure 2-S1. AAV8 exhibits higher infectivity in hairless rat skin than other comparable serotypes. A, B, and C show the same animal at three, five, and seven days after intradermal injection with approximately 10^{11} GC of AAV1-, AAV2-, AAV5-, AAV6-, AAV8-, and AAVDJ-CMV-eGFP fluorescent control vectors. Only the AAV8 (upper) and AAVDJ (lower) expression sites were observed, and expression persisted throughout the seven-day monitoring period.

Conclusions and Future Directions (Part 1)

These data shown in Part 1 establish critical groundwork for development of the biotattoo *in vivo* inflammation sensor. In Chapter 1, I conducted a feasibility survey of adeno-associated virus serotypes for transduction of murine skin cells *in vitro* and *in vivo*. These experiments were critical for establishing useful, commonly-available AAV serotypes for our preliminary experiments *ex vivo* and *in vivo*, and for other researchers conducting similar experiments in cultured mouse cells.

In the future, if AAV continues to be specifically pursued as the viral driver of the biotattoo project (see Chapter 2's last page for a brief discussion of this), it will likely require the use of synthetic serotypes specifically designed for transduction of skin cells. Several groups have used capsid engineering strategies to generate AAV serotypes designed to selectively bind to specific cell types, and this has been demonstrated by the Büning group for human keratinocytes[34]. The use of primary cells was not conducive to the large-scale experiments we needed to conduct (e.g. testing the infectivity of AAV serotypes, viability of dMNA-encapsulated viruses, or cytotoxicity of dMNA fabrication materials *in vitro*), which is why they were avoided here in favor of immortalized cell lines. However, the results of Chapter 1 clearly show the importance of conducting such assays moving forward.

Chapter 1 also shows the feasibility of using dissolvable microneedle arrays for the delivery of living viral vectors into the skin. Although only a minor piece of Chapter 1, the use of dissolvable microneedle arrays to deliver AAV to the skin is a major focus from the engineering side of the biotattoo project. Here, our efforts to use dMNAs as our primary viral delivery system were hampered by problems with mechanical design (dMNAs must be designed specifically for the skin of each model organism[71]), physical application to skin, and poor reproducibility *in vivo*. However, if these problems can be solved (e.g. by greater standardization of dMNA design and application technique), dMNAs would provide substantial advantages over traditional intradermal deliveries for the biotattoo system. Specifically, microneedle arrays are physically customizable, require no specialized training to use[108], and induce only a minimal and quick-resolving inflammatory response in the skin during wound healing[109].

Chapter 2 presents my most preliminary results, with many future directions branching off from the data shown. The use of a basic AAV-driven, NF-κB-responsive reporter *in vivo* has been demonstrated. However, a number of mechanical and logistical problems with these assays remain to be pursued and/or solved. We used a premade luciferase-based viral vector as a stand-in for our inflammation reporter when it became clear that our construct was not powerful enough to drive visible fluorescence expression through the skin. However, the use of luciferase requires the co-application of a substrate (e.g. luciferin or coelenterazine) to produce luminescent signal. This is not convenient for the purposes of a real-time biological sensor, as substrate would have to be continually provided in order to receive steady signal over time.

This requirement has been circumvented by other groups seeking to use luciferase as a real-time bioreporter system. For instance, the Sayler group has published an optimized version of the bacterial *lux* cassette containing all the genes necessary for both enzyme and substrate production[110]. However, the completed *lux* cassette contains >7500bp, making it much too large for use in adeno-associated virus vectors.

Conversely, the discussion of Chapter 2 presents several ways in which fluorescent reporters could potentially be tuned to make their signal more visible through the skin. The use of fluorescent reporters also leaves open the possibility of dual-color assays (e.g. using differently-colored fluorescent proteins within the same cells to serve as both inflammation reporter and constitutive reference element).

Another important factor to consider is the tropism of the viruses used. We have not yet conducted a thorough interrogation of which specific cells in the skin are being transduced by our viral vectors (e.g. epidermal keratinocytes, basal keratinocyte stem cells, dermal fibroblast, etc.). This will be important when considering both the efficacy and safety of the biotattoo (e.g. transduction of epidermal keratinocytes would lead to eventual loss of expression as the cell slough off the skin's surface, decreasing efficacy but increasing safety by imposing an endogenous time limit).

These are some of the most crucial questions to answer, from a cell biology standpoint, as we continue to move forward with development of the biotattoo technology. Additional questions relating to engineering (e.g. mechanical properties of the dMNAs) and immunology (e.g. inflammatory reactions to viral particles or transgenes), while also important, are not discussed here due to the relatively narrow focus of a thesis.

Overall, the results shown in Part 1 emphasize both the feasibility and potential utility of a working tattoo biosensor model. Real-time inflammation sensing remains an active area of clinical research, and the data presented here provide a crucial foundation for further development of this novel paradigm.

Part 2 – TEFLA and TAPS: Expanding the Fluorogen Toolkit for *in Vitro* Cell Contact Sensing and Targeted Photoablation

Abstract (Part 2)

Much critical and unexplored biology takes place at close interfaces between adjoining cells, particularly at neurological and immunological synapses. Neurological synapses, in particular, form interconnecting networks of such density and complexity that visualizing and categorizing them on a large scale can be difficult to impossible. Fluorescence imaging strategies have been designed to individually label each synapse in a given network for high-throughput identification and analysis. However, current such methods are time-consuming, labor-intensive, and likely to impact the function of the synapses they are meant to monitor. Here, I show the development of a new technology for fluorescently labeling points of intercellular contact using fluorogen-activating proteins (FAPs). Chapter 3 shows the trans-TEFLA assay to be capable of producing bright, dual-color fluorescence selectively at points of close contact between two different cells. Chapter 4 describes the extension of this technology to FAP-antibody fusions which can selectively label antigen-expressing cells and facilitate trans-TEFLA without the need for transgenic cells. I also show proof-of-concept data for the use of these FAP-antibodies as photoablative agents capable of killing specific cells *in vitro*.

Introduction (Part 2)

In Part 1, macro-scale fluorescence imaging was shown to be a challenging prospect, with interference from surrounding tissues, light scattering and absorption, and high autofluorescence. Conversely, at the micro-scale, fluorescence imaging is by far the most advanced and best-developed method for imaging intracellular dynamics[111]. Labeling of proteins with fluorescent tags allows researchers to track individual particles within a cell and monitor their movements and interactions with other cellular structures. Fluorescence imaging has been employed for innumerable purposes in cell biology, including the monitoring of intracellular trafficking[112], protein-protein interactions[113], and specific organelles or vesicles within a cell[114,115].

A particularly promising use for cell-scale fluorescence imaging is the labeling of intercellular contact points between two cells. Much critical and poorly-understood biology occurs at such contact points in the body[116], including electrical and chemical synapses between neurons and immunological synapses between immune cells. Traditional means of identifying intercellular contact points in cell culture or tissue samples (e.g. electron microscopy) are both subjective and labor-intensive[117,118], requiring considerable time and experience to perform adequately. A fluorescent sensor of intercellular contacts would ideally label such sites for quick, large-scale detection without the need for painstaking image analysis. Fluorescent cell contact sensing is therefore an active field of ongoing method development[119,120]. The most commonly-used methods are typically based in the general paradigm of fluorescent signal reconstitution by binding across a membrane[118,121].

An especially well-established representative example of fluorescence reconstitution-based cell contact assays is GRASP (GFP reconstitution across synaptic partners)[122]. GRASP is an assay wherein two separate domains of a superfolder GFP variant are transgenically expressed on membrane proteins on two cell types of interest. When a contact is formed between these two cells (e.g. a synapse), the two domains bind to each other and reconstitute a complete GFP molecule, which fluoresces. This technique has allowed *in vivo* imaging of formed neuronal synapses without the need for more labor-intensive methods of analysis[123]. However, it and similar techniques suffer from significant shortcomings. First, the binding and maturation of GFP is not an instantaneous process, potentially taking hours to produce fluorescent signal after synapse formation[124]. Second, once protein is reconstituted, it cannot be broken apart. GRASP is therefore an endpoint-only measurement; once the process is complete, it cannot report on the dissociation of a synapse and, indeed, tethers contacting neurons together such that dissociation is impossible[125].

Part 2 of this thesis will describe our efforts to develop a method for fluorescent sensing of intercellular contacts that circumvents these issues and introduces its own unique benefits. Our method, called trans-TEFLA (tethered fluorogen assay), relies on a protein moieties called FAPs (fluorogen activating peptides) to reversibly produce dual-color fluorescent signal at cell contact sites *in vitro*.

FAPs are a class of peptide, based on single-chain antibodies, that bind tightly to specific small molecule dyes called fluorogens[126]. These dyes are dark in solution but undergo a >10,000-fold enhancement in fluorescent signal upon binding to their cognate FAPs (Figure 3-1). FAPs can be genetically linked to proteins of interest in a manner identical to the production of standard fluorescent protein fusions. However, they have several distinct advantages that set them apart.

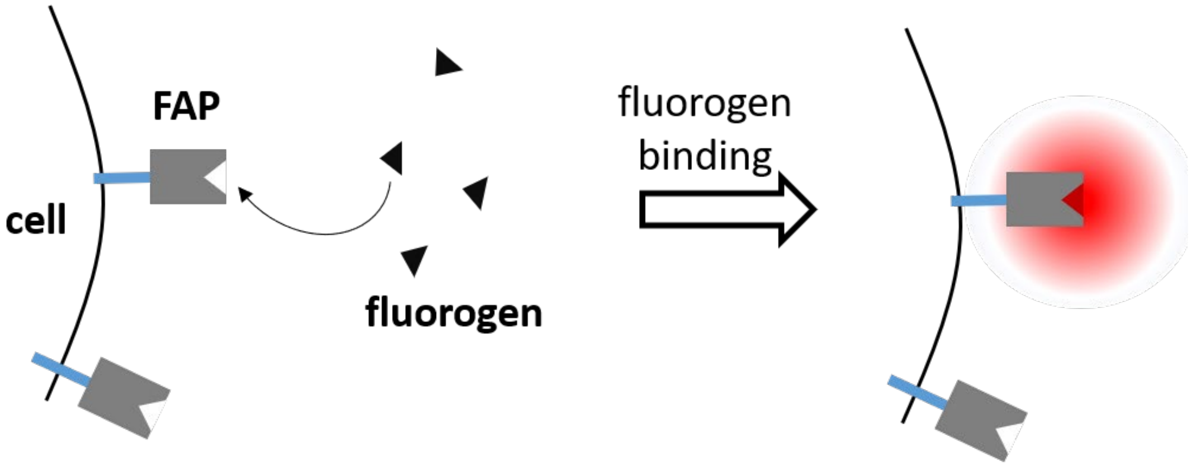
FAP
cell
fluorogen
fluorogen
binding

Figure 3-1. Fluorogen-activating proteins induce fluorescence from fluorogen ligands. Shown is a FAP linked to some cell surface protein (blue rod). It is not fluorescent but instead binds tightly to a small molecule ligand (fluorogen) that then produces fluorescent signal.

First, FAPs are modular, able to bind to multiple different fluorogens with different photochemical properties[127]. The ability to bind the same FAP with fluorogens that are green or red, strong- or weak-binding, etc., provides substantial flexibility and allows multiple assays to be performed from the same fusion protein. Specific fluorogen variants have been developed for such uses as pH sensing[128], compartment selectivity[129], and photosensitization[130]. Second, FAP/fluorogen pairs tend in general to exhibit higher brightness and greater photostability than their traditional green fluorescent protein counterparts, permitting longer and more elaborate measurements of fluorescence over time[131].

Chapter 3 of this thesis will describe the use of FAPs to develop a new method for labeling points of contact between two specific cell types. I show that trans-TEFLA can be used to produce bright, dual-color fluorescence at intercellular contact sites between cells in culture and that this labeling appears to be reversible as the contacts break apart. Chapter 4 will show data on a new application for a previously-developed fluorogen-based photosensitizer that can be used to selectively target and ablate specific cell types *in vitro*. Together, these data set the stage for rapid and reliable fluorescent labeling of physiologically-relevant contact points and the extension of our labeling reagents toward selective ablation of cells of interest *in vivo*.

Chapter 3 – Tethered Dual Fluorogens Fluorescently Label Intercellular Contacts

This work was published in Bioconjugate Chemistry and is adapted here.

Ackerman, D. S.; Vasilev, K. V.; Schmidt, B. F.; and Jarvik, J. W. Tethered fluorogen assay to visualize membrane apposition in living cells. (2017). *Bioconj. Chem.* *28*(5): 1356-1362.

Introduction

Fluorogen-activating proteins (FAPs) bind to particular non-fluorescent dye molecules (fluorogens) with high specificity, resulting in dramatic increases in fluorescence over free dye in solution by constraining release of energy via bond rotation in the fluorogen molecule[132,133]. A large number of FAP/fluorogen pairs have been described with various fluorescence spectra, binding characteristics, and photophysical properties[130,132,134]. The flexibility and modular nature of the FAP/fluorogen pair allows these unique biosensors to be useful in a wide number of biological contexts, including membrane translocation assays, live-cell confocal and super-resolution microscopy, monitoring of physiological pH, and *in vivo* photosensitizer development[130,134–138].

We recently described a tethered fluorogen assay (TEFLA) that uses FAPs to report on the proximity of recombinant protein species in the plasma membranes of individual living cells[139]. The present communication describes an application of TEFLA, “trans-TEFLA”, in which signal depends on close proximity between the membranes of two different cells. The ability to visualize regions of close contact in living cells using our approach could be useful in many contexts; of these, neuronal or immunological synapse formation and dissolution are particularly relevant, but many other biological processes (e.g. organ formation and cell migration) also involve detailed networks of contact between specialized cell types[122].

Figure 3-2A illustrates the trans-TEFLA principle. One cell (cell A) is engineered to express a protein on its surface that has high affinity for a small-molecule ligand. For example, the high-affinity protein could be avidin and the high-affinity ligand could be biotin. The other cell (cell B) expresses a FAP at its surface. Cells are cultured together and then exposed to a hetero-bivalent reagent comprised of the high-affinity ligand (e.g. biotin) joined by a flexible polymer linker to the cognate fluorogen recognized by the FAP (Figure 3-2B). The concentration of the bivalent reagent is chosen to be above the binding equilibrium dissociation constant (K_d) for the high-affinity pair and below the K_d for the FAP/fluorogen pair. In these conditions, high-affinity reagent moieties occupy the majority of their binding sites on cell A such that its surface is decorated with tethered fluorogens. The surface of cell B is not decorated with bivalent reagent molecules, however, because the reagent concentration is below the FAP/fluorogen K_d. Only if the membrane of cell B comes within a linker-length of the membrane of cell A, where the local concentration of fluorogen is very high, will FAP and fluorogen interact, resulting in fluorescent signal. This design has the potential to provide a real-time readout of the proximity status of the membranes of the two cells.

To test the trans-TEFLA approach, we used co-cultured mixtures of recombinant HEK-293 cells expressing surface-tethered protein partners of both ends of the bivalent reagent. HEK-293 cells do not form highly structured cell junctions, but in near-confluent conditions they exhibit many adventitious and transitory cell-cell contacts at which fluorescent signal might be observed.

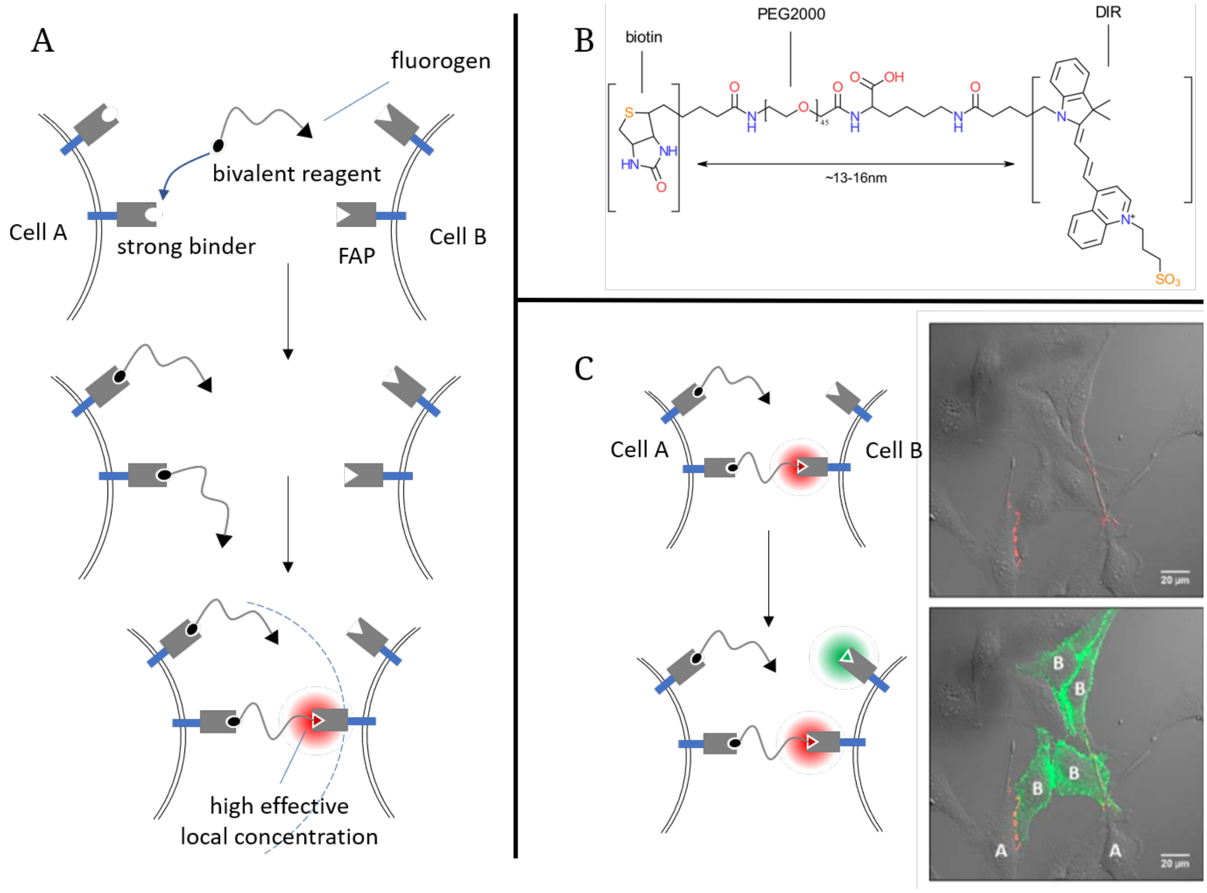
A
fluorogen
bivalent reagent
Cell A
strong binder
FAP
Cell B
high effective
local concentration
B
biotin
PEG2000
DIR
~13-16nm
C
Cell A
Cell B
20 µm
B
B
B
B
A
A
20 µm

Figure 3-2. Trans-TEFLA allows fluorescent labeling of cell contacts *in vitro*. (A) Graphic representation of the trans-TEFLA principle. Addition of bivalent reagent below the dissociation constant of the FAP/fluorogen interaction allows only weak to non-existent fluorescence from cell B. Membrane proximity with cell A raises the local concentration of tethered fluorogen, resulting in a dramatic increase in fluorescent signal. (B) Structure of bivalent reagent biotin-PEG2000-DIR. (C) Biotin-PEG2000-DIR labels contact points between cells. Upper panel shows co-cultured HEK-293 transfectants incubated with 10 nM bivalent reagent; lower panel shows the same cells after addition of 250 nM TO1-2p.

Results

In a first set of experiments, the high-affinity protein on cell-A was single-chain avidin (scAvd[140]) anchored to the membrane by a C-terminal transmembrane anchoring domain from platelet-derived growth factor receptor (PDGFR)[138]. Like avidin, scAvd is a tetravalent molecule that can bind up to four biotin moieties. For the sake of simplicity, it is represented as monovalent in Figure 3-2. The FAP on cell B was HL1[126] (also called scFv1), also anchored to the membrane by a PDGFR transmembrane domain.

The bivalent reagent was biotin-PEG2000-DIR[139], in which a biotin moiety is linked to a dimethylindole red (DIR) fluorogen via a flexible polyethylene glycol linker (Figure 3-2B). The K_d for the binding of DIR to HL1 is 440 nM. When bound to the fluorogen, DIR emits fluorescence in the red, with an excitation maximum at 610 nm and an emission maximum at 641 nm[141]. The monovalent green-fluorescing fluorogen TO1-2p (excitation/emission maxima = 510/527 nm), which also binds to HL1 with a K_d of 360 nM[126], was used as a counterstain as described below.

In order to create a mixed population of cells expressing either scAvd or HL1 on their surfaces, HEK-293 cells were transfected separately with the single transmembrane constructs and mixed on the same dish approximately 24 hours prior to imaging. When HEK-293 transfectants that expressed only the surface-localized HL1 were incubated with 10 nM biotin-PEG2000-DIR, they showed no fluorescent signal above background (Figure 3-S1A). This was expected, since 10 nM is roughly 40-fold below the K_d for the HL1/DIR pair. However, when the cells were co-cultured with scAvd-expressing transfectants and exposed again to 10 nM bivalent reagent, red fluorescence rapidly appeared at many regions of intercellular contact (Figure 3-1C, upper image). These results were consistent with the expectation that only in regions of close membrane apposition would the FAP experience a local fluorogen concentration high enough to yield signal. Low-level nonspecific red fluorescence was sometimes observed in the absence of HL1 FAP (Figure 3-S1A and -S1B), but it was not as bright as signal at true contact zones.

In these co-culture experiments, many cells expressed neither transgene, since the transfection frequencies for both cell populations were <50%. Accordingly, the majority of contact zones between cells were not expected to show signal because they were between two untransfected cells, between an untransfected and a transfected cell, or between two transfected cells expressing the same recombinant protein. Additionally, for those contact zones where we did see signal, there was no way to distinguish which cell carried the scAvd tag and which carried the FAP.

In order to reveal all of the FAP-expressing cells, we deployed a counterstain for HL1, intending to selectively label these cells without disrupting our cell-cell contact sensor. For this purpose, we added the monovalent green fluorogen TO1-2p at a concentration (250 nM) slightly below its K_d, anticipating that it would label the FAP-expressing cells in green without displacing red DIR fluorescence from the zones of contact with scAvd expressing cells due to the high local concentration of the tethered fluorogen on the cell surface. Indeed, within 60 seconds post-addition of counterstain, the membranes of the FAP-positive transfectants became clearly visible in the green channel, while the red signal at the various contact points persisted (Figure 3-2C, lower image). This allowed us to distinguish scAvd- and FAP-expressing cell identities at each labeled intercellular contact zone. Further experiments showed that bivalent reagent and monovalent fluorogen could be added simultaneously with no change in the outcome as compared to adding the reagents sequentially; accordingly, 250 nM TO1-2p was added concurrently with bivalent reagent in all subsequent biotin-PEG2000-DIR experiments.

HEK-293 cells cultured on glass surfaces typically extrude large lamellipodia from which numbers of probing filopodia extend. In our experiments, we frequently observed DIR signal at small contact points where filopodia of one cell contacted another (Figure 3-3, arrow 1). The images also revealed very fine “touch-down” points where the tip of a single filopodium contacted a neighboring cell's surface (Figure 3-3, arrow 2). Figure 3-3 shows labeled protrusions extending from cell B to cell A. In other image fields, labeling was observed for similar protrusions from cell A to cell B.

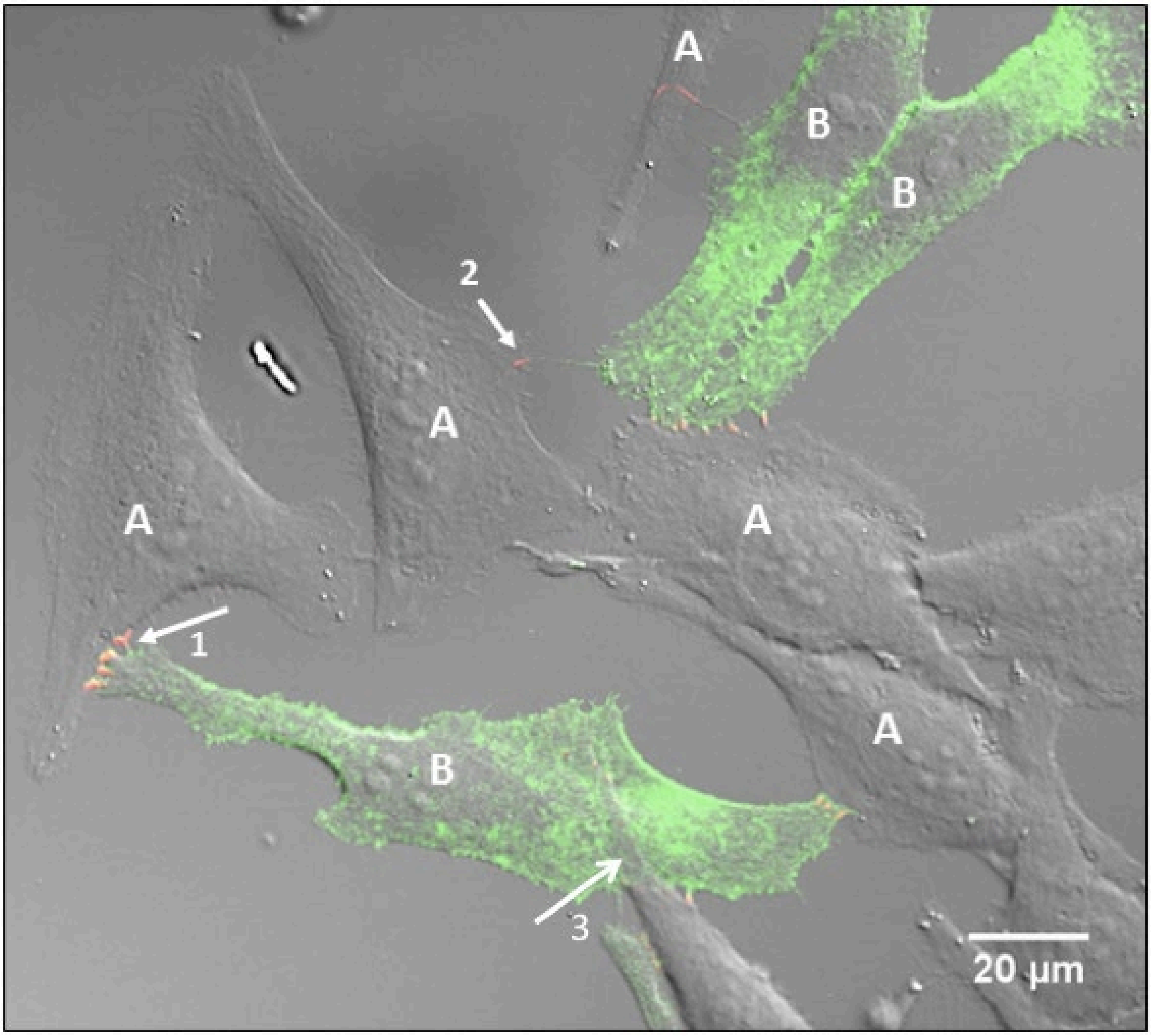

Figure 3-3. Visualization of cell-cell contacts with simultaneous application of bivalent (biotin-PEG2000-DIR) and monovalent (TO1-2p) reagents. Clustered interaction regions (arrow 1) and fine single filopodium "touch-points" (arrow 2) show DIR fluorescence. Larger regions of cell overlap do not show DIR signal (arrow 3).

To attempt to visualize both the appearance and dissolution of cell-cell contacts, we recorded representative time-lapse image series at 2-minute intervals after addition of biotin-PEG2000-DIR and TO1-2p to mixed cell cultures. A typical series lasted up to 30 minutes; Figure 3-4A presents some eventful frames from such a series. The initial frame is labeled with time-stamp 00:00 (hh:mm) although this does not represent the beginning of the time-lapse sequence but simply a relative point of initiation. At location 1' (magnified location 1) we observed a TO1-2p labeled filopodium protruding from FAP-expressing cell B, approaching proximity to the biotin-PEG2000-DIR decorated membrane of scAvd-expressing cell A (Figure 3-4A, 00:00-1'). Micrographs were recorded 2 minutes apart. At time point 00:02 the same filopodium had extended and overlapped with cell A, although DIR activation was not yet achieved (Figure 3-4A, 00:02-1'). At time point 00:04 we recorded the appearance of new DIR fluorescence. The TO marker showed that this event occurred at the tip of the extended filopodium, while the differential interference contrast channel allowed us to clearly locate the non-fluorescent membrane of cell A (Figure 3-4A, 00:04-1').

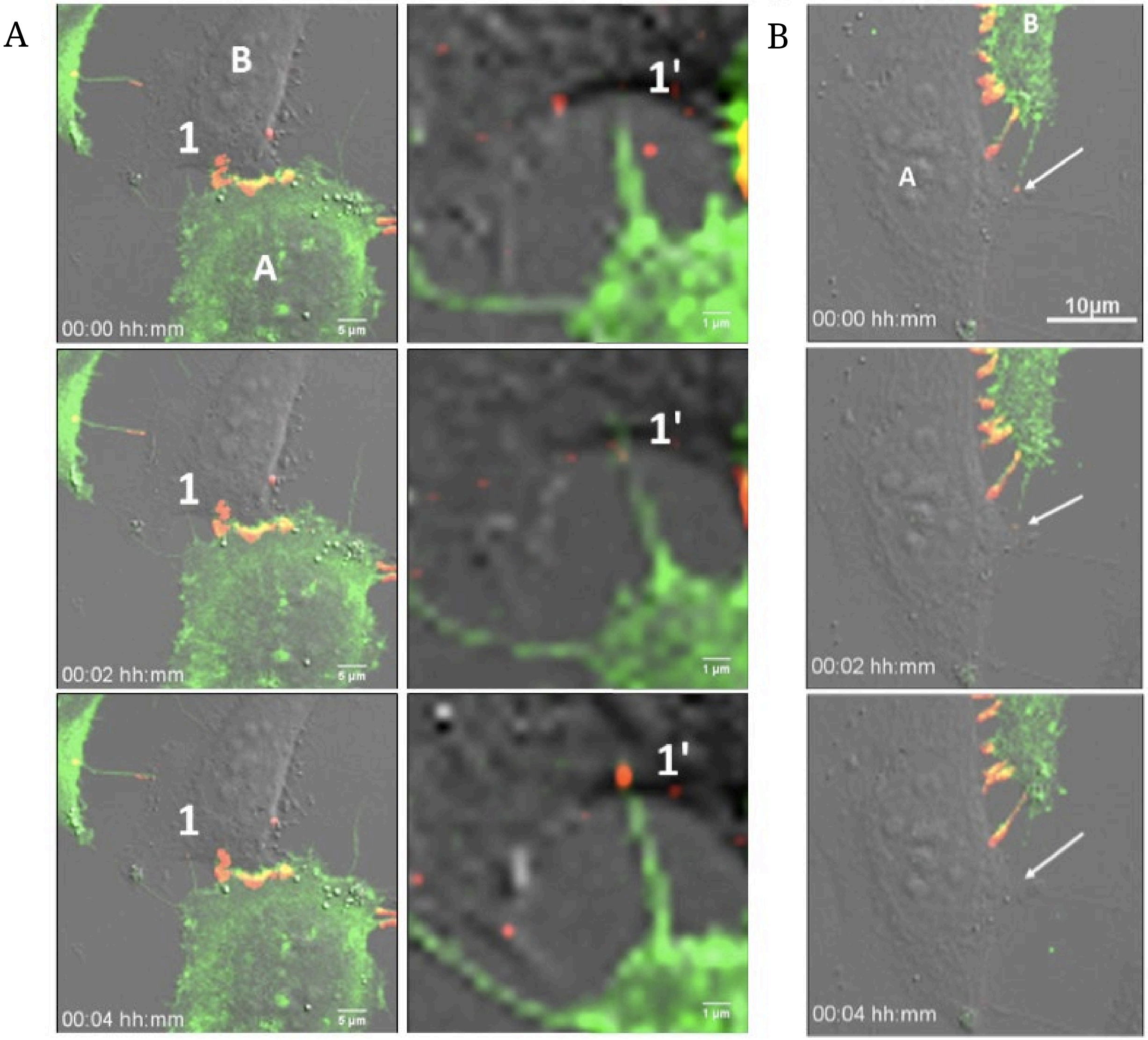
A
B
1
A
00:00 hh:mm
5 µm
1'
1 µm
1
00:02 hh:mm
5 µm
1'
1 µm
1
00:04 hh:mm
5 µm
1'
1 µm
B
B
A
00:00 hh:mm
10µm
00:02 hh:mm
00:04 hh:mm

Figure 3-4. Visualizing formation and loss of cell-to-cell contacts using trans-TEFLA. 30-minute time lapse sequences were recorded (2min intervals) after addition of 10 nM biotin-PEG2000-DIR and 250 nM TO1-2p. (A) Three consecutive frames at two levels of magnification showing a single filopodium extending from cell A towards cell B that acquires DIR fluorescence at its tip only after contacting cell A. (B) Three consecutive frames showing a filopodium shortening and losing DIR fluorescence at its tip as contact with cell A is lost.

In other series, we observed the loss of already-established intercellular contacts, with DIR fluorescent signal disappearing as the interacting membranes separated. To our knowledge, this has never been demonstrated before by direct *in vivo* fluorescence microscopy. In time-lapse series taken over several hours, we captured the retraction process for a number of individual filopodia, as demonstrated in Figure 3-4B. At relative time point 00:00, a filopodium extends from cell B to cell A. DIR signal was present at the tip of the filopodium in contact with cell A (arrow, Figure 3-4B, 00:00). At time point 00:02, the filopodium appears slightly shortened with diminished DIR fluorescence. By 00:04, DIR signal is completely gone. The TO1-2p fluorescence and differential interference contrast images confirm that fluorescence loss accompanied physical separation of the filopodium from cell A. These results provide proof-of-concept for trans-TEFLA as a means to track both forward and reverse dynamics of cell-cell contacts without subjecting the cells to wash steps or multiple reagent additions during observation.

Trans-TEFLA using two different FAPs.

Additional pilot experiments were performed in which the high-affinity protein was itself a FAP. In particular, we used the FAP dL5 (also called dNP138[142,143]), which binds its cognate fluorogen, malachite green (MG), very tightly (K_d < 1 nM). Here, the hetero-bivalent reagent was MG-PEG3500-TO1 (Figure 3-5A). This reagent follows the same principles as the biotin-PEG2000-DIR reagent (Figure 3-5B) but does not require the addition of a secondary dye to distinguish cell populations. Additionally, this dye exhibits no nonspecific fluorescence of the weak binder when bound to dL5-expressing cells and minimal interaction between TO1 and its cognate FAP when below the K_d (Figure 3-S1C). The MG moiety in this reagent fluoresces in the far red when bound to the dL5 FAP (excitation maximum 634 nm, emission maximum 667 nm[126,134]), and so its signal is readily distinguished from the green fluorescence characteristic of TO1 bound to HL1.

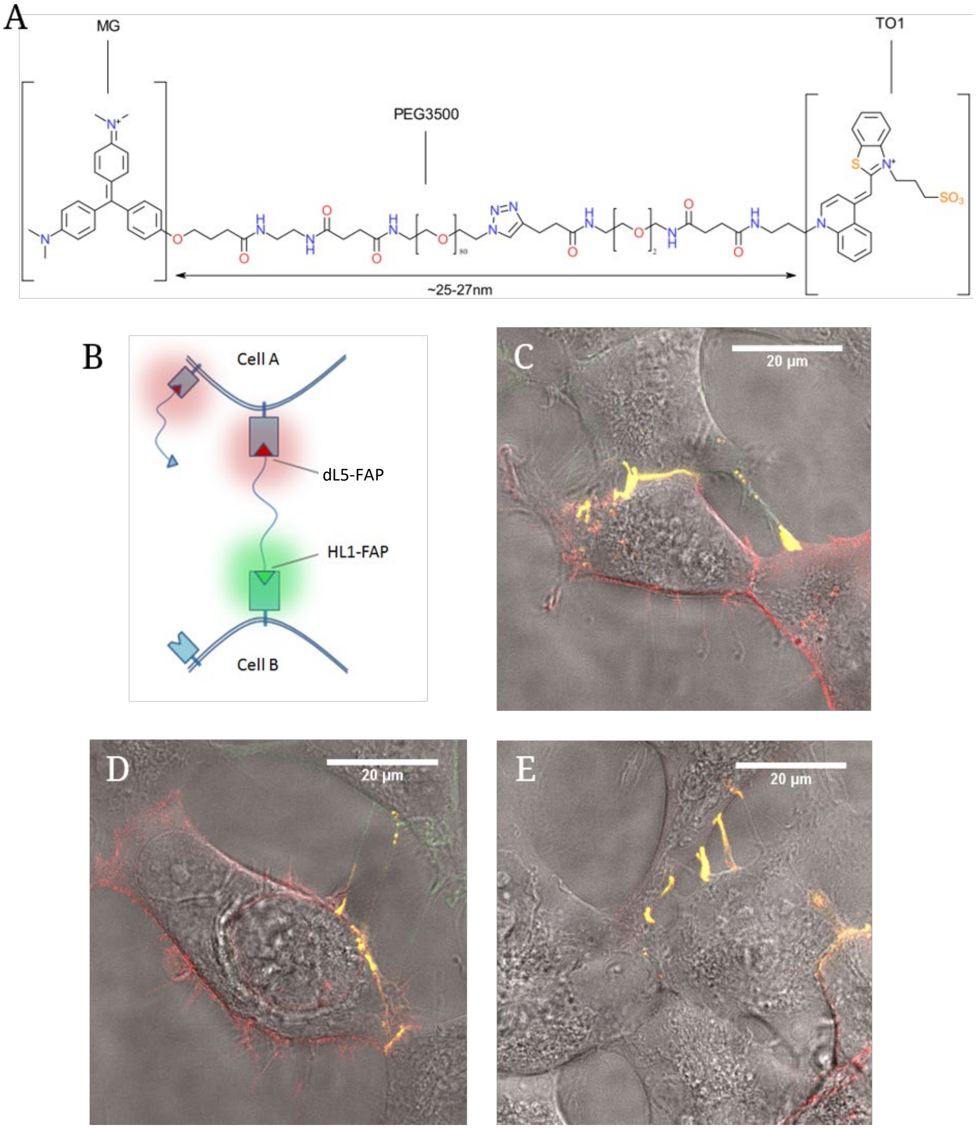

Figure 3-5. Bivalent FAP reagent selectively labels intercellular contacts with bright, dual-color fluorescence. (A) Structure of the MG-PEG3500-TO1 reagent. (B) Graphic illustrating trans-TEFLA with this reagent on HL1- and dL5-tagged cells. Representative confocal fluorescence micrographs (C-E) show co-cultured HEK-293 cells (expressing dL5 and HL1 FAPs) exposed to 25 nM MG-PEG3500-TO1 reagent. The plasma membranes of dL5-expressing cells are strongly labeled at all locations. HL1 membranes exhibit weak green fluorescence except at points of close proximity to dL5 membranes where the signal dramatically increases in proportion with the local concentration of TO1.

When HEK-293 cells were transfected to express the individual FAPs, co-cultured, and exposed to 25 nM bivalent reagent, strong red fluorescence rapidly appeared on the medium-exposed surface of the dL5-expressing cells, and very weak green fluorescence appeared at equivalent locations on the HL1-expressing cells. This was expected, since the concentration of bivalent reagent was well above the K_d for the MG/dL5 pair and well below the K_d for TO1/HL1. Strong green fluorescence also appeared, but only in regions of close contact between the two cell populations. Examples are shown in Figure 3-5C, -5D, and -5E; locations with strong green signal appear yellow because of the co-localized green and red fluorescence from TO1 and MG, respectively.

To quantify the extent of signal augmentation in regions of cell contact, we tabulated the highest pixel values in cell edges and projections that showed TEFLA signal and the brightest pixels at edges and projections of the same cells that did not show TEFLA signal (Figure 3-S2A, -S2B, and -S2C). We divided the former value by the latter to obtain a fold increase in fluorescence intensity at regions of TEFLA contact. The analysis indicated that green signal increased by an average of ~10.5-fold at regions of contact (Figure 3-S2D). Red signal also increased, but more modestly, with the increase likely resulting from reduced lateral diffusion of the fusion proteins out of the contact zone due to the transitory linking of the FAPs by the bivalent reagent.

Discussion

In both sets of experiments, strong TEFLA signal was observed after reagent addition where cells A and B directly abutted each other, or where filopodia or other thin extensions of one cell meet lamellopodia or filopodia of the other. Strong signal generally did not appear where an extensive portion of one cell lay above or below another (e.g., Figure 3-3, arrow 3). As this image is focused on filopodia contacts, it does not preclude the possibility of out-of-focus TEFLA signal above the z-level shown. However, another plausible explanation for this observation is that in such regions of cell-cell overlap, the membranes are too far apart for the bivalent reagent - whose extended linker length is estimated to be 13-16 nm for the biotin-PEG2000-DIR reagent and 25-27 nm for the MG-PEG3500-TO1 reagent - to reach from one membrane to the other, perhaps due to intervening extracellular matrix or glycocalyx[144]. If this is the case, then bivalent reagents synthesized with longer linkers might show TEFLA signal, and thereby provide an approximate measuring rod to evaluate membrane-to-membrane distance. An alternative possibility is that the reagent is inhibited from diffusing into cell-overlap regions by glycocalyx or extracellular matrix, but if this were the case, we would expect a line of signal at the margins of the overlapped region, and this was not observed. One way to resolve these ambiguities would be to apply correlated light and electron microscopy approaches[145] to reveal the ultrastructure in regions where signal is strong and where it is not.

Although we did not attempt to determine the affinity or dissociation constants of the bivalent reagent for the high-affinity FAP, it is clear from our data that the affinity is high, since 25 nM bivalent reagent was sufficient to brightly label the surface of dL5-expressing cells (Figure 3-5). This was what we expected, since the chemical structure of the linker near the fluorogen is identical to that in the established strong-binding monovalent fluorogens MG-2p and MG-11p[126] . In contrast, a significant reduction in FAP binding affinity was seen when the MG moiety was appended to bulky methacrylate polymers decorated with ethylene oxide sidechains[146], which may be expected to sterically clash with the FAP and decrease binding affinity more strongly than the simpler PEG construct we employed.

In the experiments described here, our intent was to uniformly label the plasma membranes of cells A and B with the strong-affinity and weak-affinity protein moieties, and so those moieties were anchored to the membrane by a single transmembrane helix that was not expected to have biological activity of its own. However, in future studies, the FAPs could be fused *to bona fide* membrane proteins of interest - e.g., to proteins that localize to presynaptic or postsynaptic membranes of neurons, where they could provide dynamic live-cell reporters of the formation and dissolution of individual synapses. In such a context, trans-TEFLA could provide an attractive alternative to current biosensor systems based on protein fragment complementation[123,125,147,148] – systems that, unlike TEFLA, lock apposed membranes together and thus cannot report on the dissolution, as well as the formation, of synapses or other cell junctions.

Finally, we note that the methodology described here is currently limited to transgenic cells that express recombinant fusion proteins. If, however, one could use existing antibodies to direct the FAP moieties to chosen cellular locations – e.g., to proteins in the pre- and post-synaptic membranes of particular synapses – then the approach would have much wider application, as it would no longer require the generation of transgenic models for use. We have previously reported on the use of IgG-binding protein A and protein G domains to link standard antibodies to FAPs[149], and we are currently exploring the adaptation of such methods to the trans-TEFLA technology.

Materials and Methods

Reagents and instruments for the synthesis of MG-PEG3500-TO1.

Azide-PEG3500-NH2 was purchased from JenKem Technology. 4-Pentynoic acid was purchased from GFS Organic Chemicals. TSTU was purchased from Advanced Chem Tech. All other reagents were purchased from VWR. ^{1}H NMR spectra were recorded at 500 MHz on a Bruker Avance instrument. Size exclusion chromatography was performed on BioRAD P2-gel. High Pressure Liquid Chromatography analysis was performed on a Waters Acquity UPLC using a Waters Acquity RP-18 column. Electrospray ionization mass spectrometry (ESI-MS) experiments were conducted on a Finnigan LCQ quadrupole ion trap mass spectrometer in positive ion mode using Xcalibur version 1.2. MALDI experiments were performed on an Applied Biosystems Voyager DE-STR MALDI-TOF instrument.

scAvd and FAP expression vectors.

The mammalian expression vector pDisplay-scAvd was constructed by PCR-amplifying the scAvd coding sequence[140] flanked by SfiI restriction sites from template DNA provided by Dr. Vesa Hytonen (University of Tampere, Finland), and ligating the amplicon into pDisplayBlue[150]. pDisplayBlue-HL1 and pDisplay-dL5 were constructed equivalently, using HL1[126] or dL5[134] DNA as templates.

Cell culture and transfection.

HEK-293 cells were cultured under standard conditions in a tissue culture incubator at 37°C and 5% CO_2. Growth media was DMEM (with 4.5g/L glucose, L-glutamine, and sodium pyruvate) supplemented with 10% fetal bovine serum and with or without 10U/mL penicillin and streptomycin. Transfections were performed using *Trans*IT-LT1 (Mirus, Madison WI, #MIR 2300) or Xfect (Takara Bio) transfection reagents following manufacturers' instructions. Twenty-four hours post-transfection, cells were lifted and co-cultured on glass-bottom MatTek dishes (MatTek, Ashland, MA, cat. #P35GC-0-14) to allow confocal microscopy. Cells were cultured together for a further 24 hours prior to fluorescence imaging.

Fluorescence microscopy.

Fluorescence microscopy was performed on a Carl Zeiss LSM 510 or 880 confocal microscope equipped with heated, humidified culture chambers at 5% CO_2. FAP dyes, either biotin-PEG2000-DIR or MG-PEG3500-TO1, were added to cells at concentrations of 10 and 25 nM, respectively, in order to saturate the strong binder while remaining well below the K_d for HL1. Cells were allowed to label with dye for 10 minutes prior to imaging. Cells were not washed prior to imaging, as this is not required for trans-TEFLA imaging. On the LSM 510, 488 and 633 nm lasers were used and signal collected with 505-550 nm and 650lp filters. On the LSM 880, an argon 488 nm and solid-state 633 nm laser were used with corresponding bandpass emission filters of 490-562 nm and 641-695 nm. Microscopy on the LSM 510 instrument used an oil immersion 40X objective, and on the LSM 880 an oil immersion 63X plan apochromat objective. Microscopy settings were adjusted to minimize signal saturation and zero value intensities and were then held constant throughout each experiment. The resulting images were analyzed using Fiji[151]. Fluorescence intensity quantitation for the MG-

PEG3500-TO1 reagent was performed in Fiji by drawing through contact cells lines containing points of TEFLA contact and noncontacting regions (Figure 3-S2A), as described above. The profile plots (Figure 3-S2B and -S2C) were used to determine the brightest pixel values in arbitrary units for both areas in the TO1 and MG channels. This analysis was done for a total of 47 contact regions. For statistical analysis (Figure 3-S2D), a Wilcoxon signed rank test was used to determine that the median of both data sets (TO1 and MG fold increases) was significant above a theoretical median of 1 (which would imply equal fluorescence at contact and noncontact regions). The data were analyzed in Microsoft Excel 2016 and plotted and statistically analyzed with GraphPad Prism v7.03 for Windows (GraphPad Software).

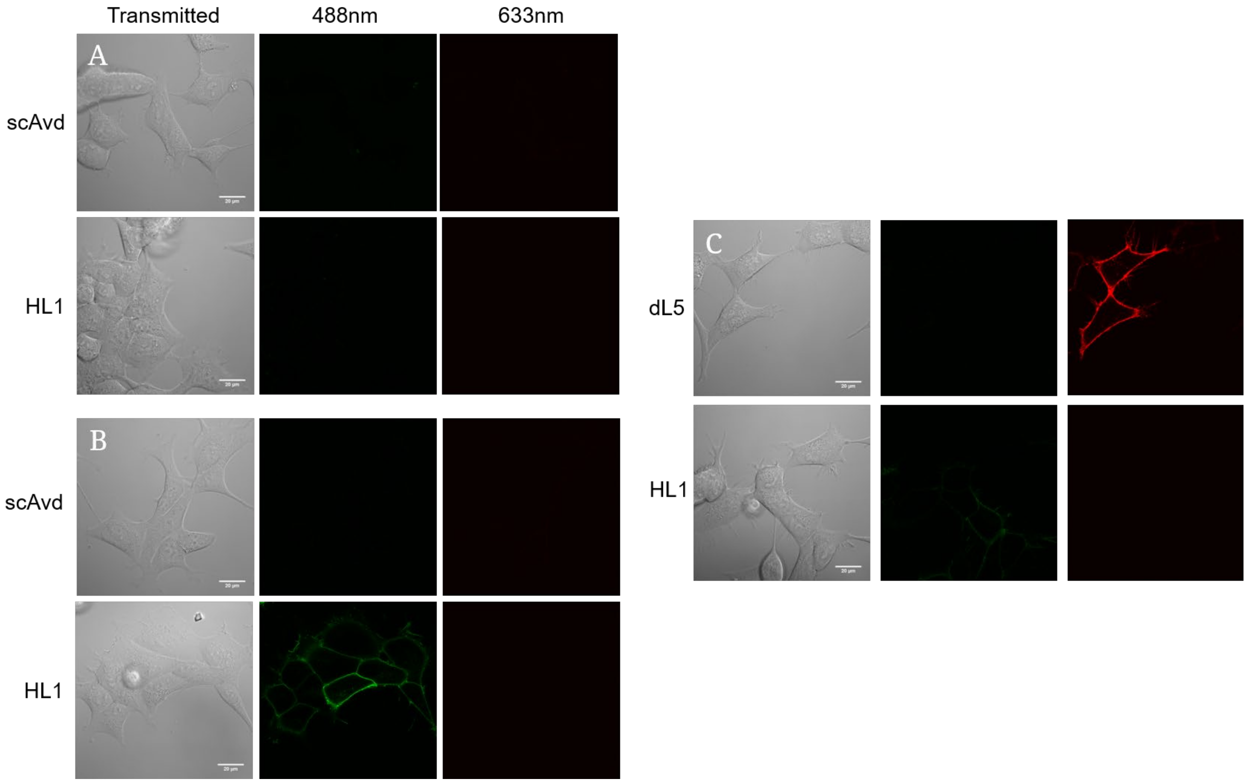

Figure 3-S1. Trans-TEFLA reagents applied to single cognate-expressing HEK-293 cells with or without counterstain. A. Cells expressing either cell surface scAvd (top) or HL1 (bottom) and treated with 10 nM biotin-PEG2000-DIR reagent. B. Cells expressing scAvd (top) or HL1 (bottom), treated with 10 nM biotin-PEG2000-DIR and 250 nM TO1-2p. C. Cells expressing dL5 (top) or HL1 (bottom), treated with 25 nM MG-PEG3500-TO1 reagent. Microscope settings and lookup tables are identical to Figure 3-4 to allow direct comparison. Scale bars = 20 µm.

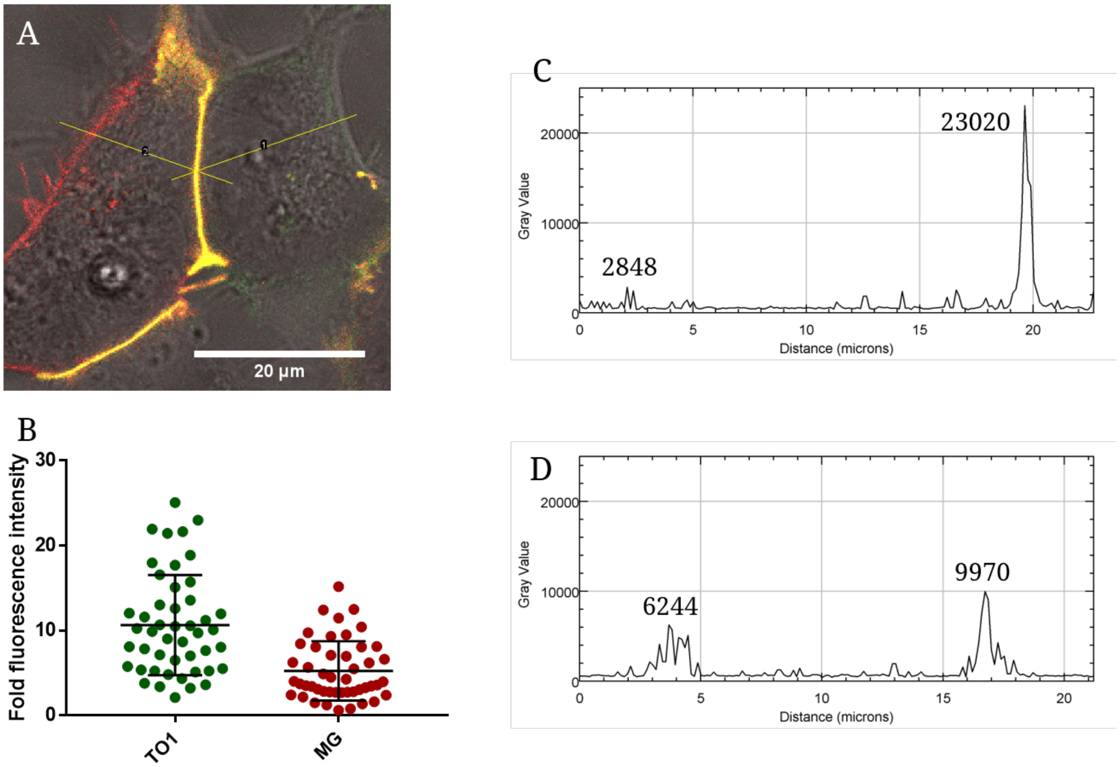

Figure 3-S2. Quantification of increase in fluorescence intensity at points of contact between HL1 and dL5 surface-expressing cells exposed to 25 nM MG-PEG3500-TO1 trans-TEFLA reagent. (A) Representative image showing line ROIs drawn across cells, containing both regions of TEFLA contact and noncontacting regions. #1 = line drawn for HL1-expressing cell. #2 = line drawn for dL5-expressing cell. (B) Scatterplot showing increase in the fluorescence intensity of the green signal (TO1) or red signal (MG) at regions of contact between HL1- and dL5-expressing cells. Data shown is the ratio of the intensity at the contact point over the intensity at a noncontacting area of membrane (fold increase in fluorescence intensity at intercellular contacts). Data are n=47 individual measurements shown with mean (long black line) ± SD. (C-D) Plot profiles generated by Fiji for lines 1 (C; HL1) and 2 (D; dL5). Numbers shown are the maximum pixel values in the noncontacting region (left) and contacting region (right).

Chapter 4 – FAP-Antibody Fusions Facilitate Antigen-Specific Labeling, Intercellular Contact Sensing, and Photoablation

This work was published in Bioconjugate Chemistry and is reprinted here.

Ackerman, D. S.; Altun, B.; Kolodieznyi, D.; Bruchez, M. P.; Tsourkas, A. T.; and Jarvik, J. W. Antibody-linked fluorogen-activating proteins for antigen detection and cell ablation. (2019). *Bioconj. Chem. 30*(1): 63-69.

Introduction

Fluorogen-activating proteins (FAPs) bind organic dyes (fluorogens) that are not fluorescent in solution but become strongly fluorescent when bound to the FAP[126]. Since their initial description in 2008, FAPs have been used to probe a wide variety of biological processes including receptor trafficking, membrane translocation, and changes in intracellular pH[129,133,135,137,138,152]. When used in conjunction with membrane-impermeant fluorogens, FAPs have proved to be particularly valuable for labeling membrane proteins at the cell surface and monitoring their subsequent trafficking to and from the cell interior[128,136–138,153].

A given FAP can activate the fluorescence of multiple chemically-related fluorogens, each with distinct biochemical and spectral properties[128,131,132,138,149,154,155]. The dL5/MG pair used here, for instance, emits light in the far red spectrum where tissue autofluorescence and phototoxicity are low[126,129]. dL5 is also able to bind the green-emitting fluorogen MHN-ester[155], which enables two-color assays and pulse-chase experiments. The modularity of the FAP/fluorogen system thereby allows a single peptide scaffold to serve multiple purposes for cell imaging or manipulation, including compartment and sub-population selectivity through the use of membrane permeant vs. impermeant dyes[127].

Also used here is the iodinated fluorogen MG-2I, a Targeted and Activatable PhotoSensitizer (TAPS) molecule, that generates cell-destructive singlet oxygen molecules when bound to the FAP and irradiated with far-red light. It can thus be used to selectively ablate FAP-carrying cells[130].

Published studies using FAP reporters have generally employed transgenic cell lines that express recombinant FAP-tagged proteins. These allow high-resolution assays in transfected cultured cells, but do not provide an easy path to performing equivalent assays in living organisms, where transgenic production is challenging and risky[156]. A more translatable alternative is to couple the FAPs to antibodies with binding specificities for proteins of interest, thereby enabling FAP labeling of endogenous native proteins.

In one approach, we produced a chimeric fusion protein with a FAP domain and an affibody domain, and we showed that it delivered the FAP to endogenously expressed antigen in cultured cells[127,157]. This approach is of limited general utility, however, because it requires the generation of a new chimeric reagent for each new target.

In a second approach, we generated reagents comprised of FAPs linked to known Fc-binding domains derived from Protein-A or Protein-G, and we showed that mouse and rabbit IgGs formed complexes with these reagents that specifically delivered the FAPs to antigens in fixed and live mammalian cells[149].

A limitation of this approach, however, is that the non-covalent FAP-antibody complexes are subject to spontaneous dissociation during storage or use.

As described here, we have overcome this limitation by generating a FAP reagent that is readily photo-crosslinked to IgGs in a site-specific manner[158], yielding stable conjugates with the antigen-recognition properties of the antibody and the detection/ablation properties of the FAP. We demonstrate the use of these conjugates to (1) label cell surface antigens in cultured human cells, (2) detect zones of close proximity between one cell and another, and (3) photo-ablate antigen-expressing cells. Since thousands of validated primary antibodies are readily available for FAP-conjugation[159], such conjugates should be widely applicable for experimental and therapeutic purposes.

Results

Generation of HTB1-FAP reagent and conjugation to antibodies.

A fusion protein with an N-terminal HTB1(A24BPA) domain[158] and a C-terminal FAP (dL5, MBIC6) domain was expressed and purified as described in Experimental Procedures. HTB1 is a thermally stable variant of the B1 domain of Protein G with a photoreactive amino acid, benzoylphenylalanine, in its Fc-binding region. FAP dL5 binds fluorogens that are derivatives of the triaryl methane dye malachite green[134]. The HTB1-FAP reagent was photo-crosslinked to two monoclonal antibodies: cetuximab (Erbitux), whose target is the human receptor tyrosine kinase EGFR/HER1, and trastuzumab (Herceptin), whose target is the human receptor tyrosine kinase HER2. As shown for cetuximab in Figure 4-S1, the procedure led to near complete covalent crosslinking of the HTB1-FAP polypeptide to the antibody.

Visualization of EGFR and HER2 in human cell lines.

HaCaT and A431 cells, which are known to express EGFR[160,161], were incubated with FAP-conjugated cetuximab and membrane impermeant MG-fluorogen. Strong fluorescent signal was observed at the cell surface (Figure 4-1). Some internalized signal was also observed, due to the internalization of some receptor molecules by endocytosis during the incubation[162]. HEK-293 cells, which express little or no EGFR[160,163], were not labeled, nor were HaCaT or A431 cells that were treated as in Figure 4-1 but without conjugated antibody.

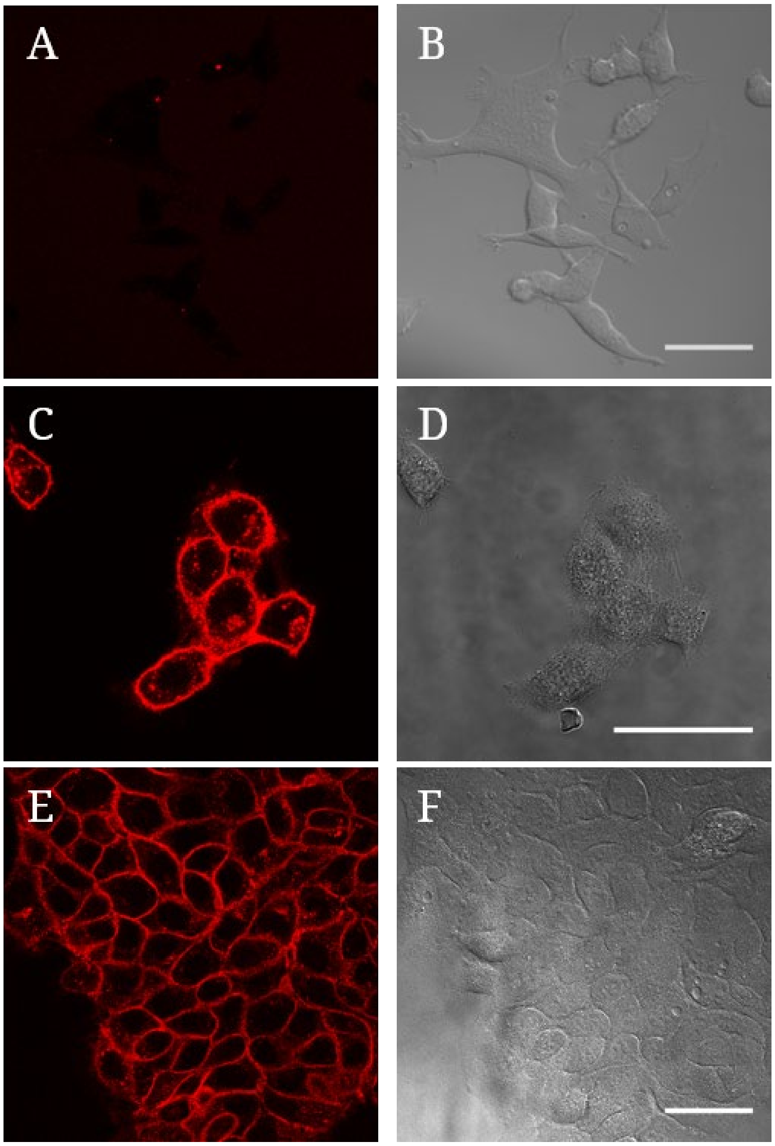

Figure 4-1. dL5-cetuximab labels EGFR on HaCaT and A431 cells. (A-B) HEK-293 cells are not labeled by the reagent. (C-D) HaCaT and (E-F) A431 cells are labeled with dL5-cetuximab and MG fluorogen. MG fluorescence is shown on the left, DIC transmitted light images on the right. Scale bars = 50 μm.

Fixed cells were also probed with the labeled antibody (Figure 4-2). As expected, signal was confined to the surface in unpermeabilized cells, and was seen on the surface and more diffusely inside the cell in fixed and permeabilized cells.

The procedures described above to produce FAP-conjugated cetuximab were also applied to trastuzumab (Herceptin), an antibody whose target is the human tyrosine kinase HER2/ERBB2, and the conjugate was used to probe SK-BR-3 cells, which natively express high levels of HER2[164]. As shown in Figure 4-3, FAP-conjugated trastuzumab labeled SK-BR-3 cells with similar effect as the cetuximab reagent on EGFR-expressing cells. HEK-293 cells, which express minimal HER2, were not labeled by dL5-trastuzumab.

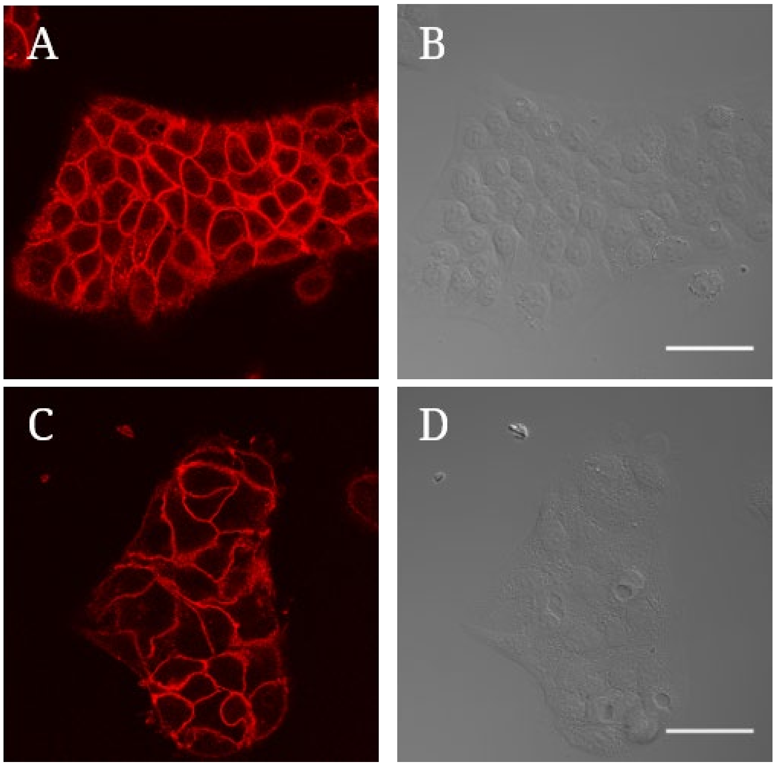

Figure 4-2. dL5-cetuximab labels EGFR on fixed HaCaT cells. (A-B) Permeabilized and (C-D) unpermeabilized HaCaT cells labeled with dL5-cetuximab and MG fluorogen. MG fluorescence is shown on the left, DIC transmitted light images on the right. Scale bars = 50 μm.

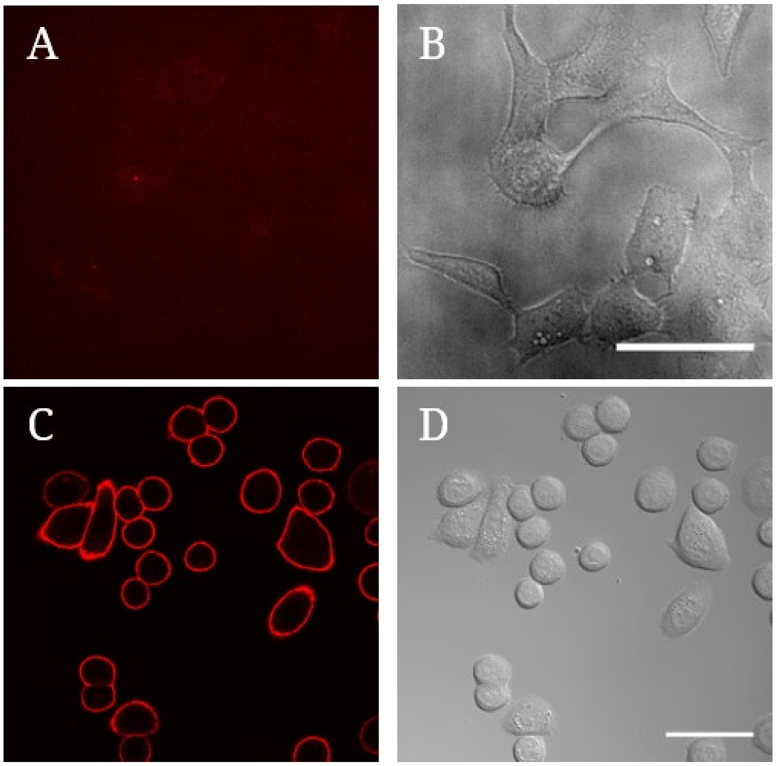

Figure 4-3. dL5-trastuzumab labels HER2 on SK-BR-3 cells. (A-B) HEK-293 cells are not labeled by the reagent. (C-D) SK-BR-3 cells are labeled with dL5-cetuximab and MG fluorogen. MG fluorescence is shown on the left, DIC transmitted light images on the right. Scale bars = 50 µm.

Visualization of cell-cell contacts using FAP-tagged antibodies.

Previously[139,165], we developed a technology called trans-TEFLA (tethered fluorogen assay), in which contact points between two FAP-expressing cell lines exhibit bright fluorescence when labeled with a bivalent fluorogen (MG-PEG3500-TO1). One cell line, expressing dL5, produces red fluorescence when it binds the MG moiety of the bivalent reagent, while the other, expressing scFv1, yields green fluorescence upon binding the TO1 moiety. The "red" FAP binds its fluorogen with a very low Kd (~100 pM), whereas the "green" FAP binds its fluorogen with a much higher Kd (~350 nM). When bivalent fluorogen is provided at an intermediate concentration (10 nM), the red FAP is saturated with fluorogen and thus gives red fluorescence over the entire cell surface, but the green FAP only gives fluorescence when it is very close to the red FAP, where the local concentration of the TO1 moiety is very high. This leads to distinct red plus green (yellow) fluorescence at intercellular contact sites when the cells are co-cultured. There, both cell lines were required to be transgenic in order to express the FAP constructs. However, ease of use and biological applicability would both increase for the trans-TEFLA technology if it did not require the use of transgenic cells.

Here, we sought to advance on this goal by using dL5-cetuximab to replace the transgenic FAP construct on one member of the trans-TEFLA pair (Figure 4-4A). Specifically, we used dL5-cetuximab to label wild-type HaCaTs, which were co-cultured with transgenic scFv1-expressing HEK-293 cells. In these cultures, bright yellow fluorescence was apparent at intercellular contact points (Figure 4-4B and -4C), in a manner identical to that previously seen between two transgenic cell lines[165]. When the cells were incubated with separate, unlinked MG and TO1 fluorogens (Figure 4-4D and -4E), no fluorescence enhancement at contact sites was observed.

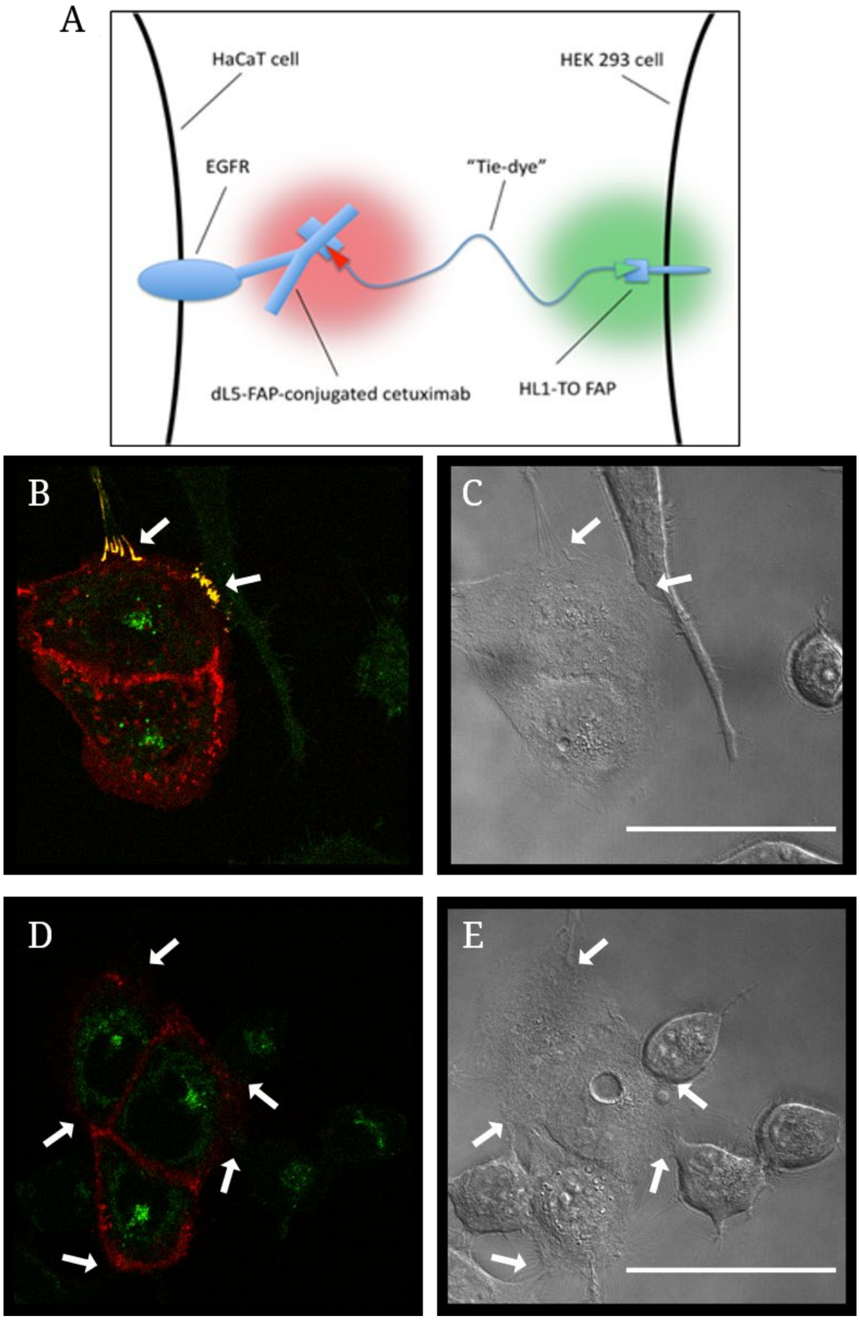

Figure 4-4. dL5-cetuximab facilitates trans-TEFLA with only one partner expressing transgenic FAP. (A) Schematic illustrating the trans-TEFLA principle applied to the dL5-antibody system. (B) and (C) Co-cultured wild-type HaCaT and scFv1-expressing HEK-293 cells. HaCaTs are uniformly surface-labeled by dL5-cetuximab bound to MG-PEG3500-TO1 dual fluorogen, with faint green fluorescence on the scFv1-HEKs. Bright fluorescence enhancement in both channels is observed at sites of intercellular contact (white arrows). (D) and (E) Equivalent cells incubated with single dyes (MG and TO1 fluorogens) exhibit similar labeling but without enhancement at contact sites. Green signal inside HaCaT cells represents background autofluorescence. Scale bars = 50 µm.

FAP-directed photo-ablation.

We also asked whether the FAP-conjugated antibodies could be used to photo-ablate cells using the iodinated photosensitizing fluorogen MG-2I[130]. Antigen-expressing cells grown on optical surfaces were treated with conjugated antibody, followed by addition of either the photosensitizing fluorogen or control fluorogen (MG Ester). Cultures were then illuminated with high-intensity 640 nm light for 7.5 minutes - conditions that had previously been shown to produce severe photodamage in HEK-293 cells that expressed the dL5 FAP[130]. To aid in detecting and quantifying cell injury, we applied 1 μM calcein AM (stains cytoplasm of intact cells) and 5 μM ethidium homodimer-1 (EthD-1, a DNA stain that reaches the nucleus of membrane-damaged cells) to the cultures.

By 30 minutes post-illumination, the cells with the photosensitizing fluorogen showed clear evidence of injury, including surface blebbing and contraction, EthD-1 staining of the nucleus, and diminished calcein signal (Figure 4-5A and -5B). Cells that received the control fluorogen were largely unaffected (Figure 4-5C and -5D).

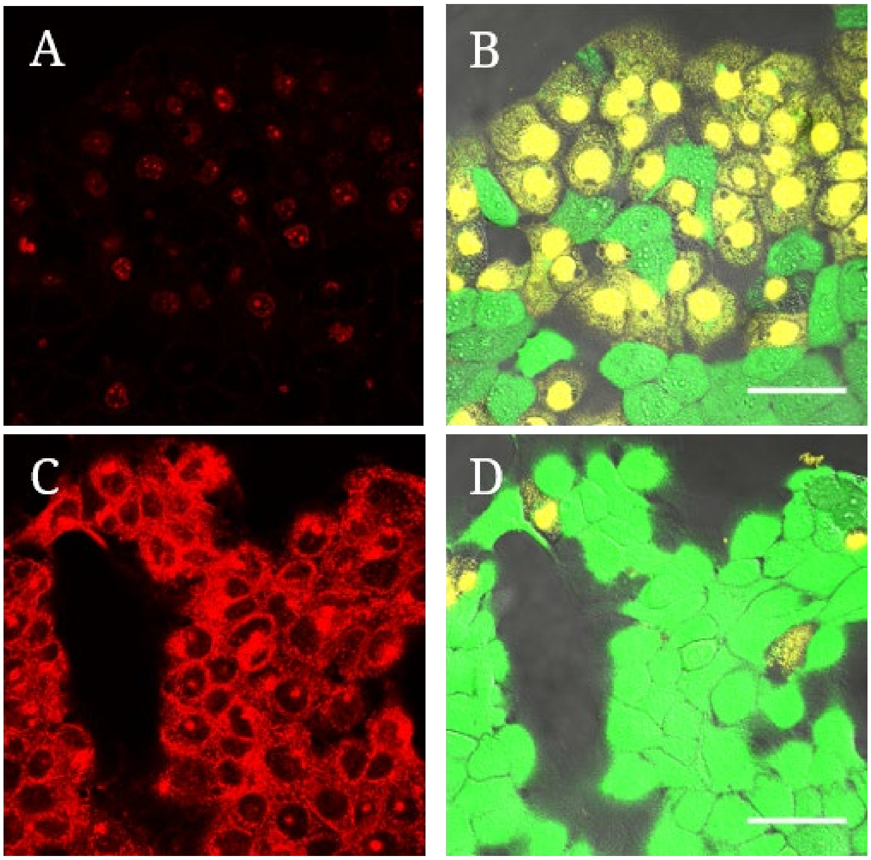

Figure 4-5. dL5-cetuxiumab and MG-2I mediate cell death in EGFR-expressing cells. (A-B) Red channel and merged green and yellow channels (calcein AM and EthD-1, respectively) are shown for HaCaT cells labeled with dL5-cetuximab and MG-2I. (C-D) Red signal shown for non-photosensitizing control fluorogen MG Ester, along with the calcein AM and EthD-1 channels. Scale bars = 50 μm.

To provide a quantitative counterpart to the microscopy data shown in Figure 4-5, we conducted a fluorescence-based cell viability assay (alamarBlue) on irradiated and non-irradiated cells (HEK-293, HaCaT, and A431) to confirm that irradiation of MG-2I bound to dL5-cetuximab on endogenous EDGR leads to cell death in high-expressing cells. Results are shown in Table 4-1. In this assay, living cells reduce resazurin to resorufin, which is highly fluorescent. Therefore, cell damage and death are indicated by a reduced level of overall fluorescent signal. Substantial cell damage and/or death were evident in irradiated A431s, which express high levels of EGFR. This was not observed in EGFR-negative HEK-293 cells. HaCaT cells, which have an intermediate EGFR expression profile, showed a downward trend in signal after irradiation, though less dramatic than for A431 cells.

Table 4-1. Fluorescence intensity data from plate reader analysis of alamarBlue-treated HEK-293, HaCaT, and A431 cells after treatment with dL5-cetuximab +MG-2I and photoirradiation. Numbers shown are averages and standard deviations, in arbitrary units, from 5 replicates for each condition. Background fluorescence (media + alamarBlue only) has been subtracted out. Irr. = cells irradiated at 640 nm. Non-irr. = cells not irradiated. Ester/2I only = only fluorogen, no FAP/antibody. Cetux+Ester/2I = antibody and indicated fluorogen.

HEK-293 cells				
	Irr.		*Non-irr.*	
	Avg.	StdDev.	Avg.	StdDev.
Neg. ctrl.	20420	3273	20997	8501
Ester only	15206	4080	16790	3229
2I only	18512	2912	20633	9015
Cetux+Ester	16882	3158	20088	3802
Cetux+2I	16946	2957	19855	4996
HaCaT cells				
	Irr.		*Non-irr.*	
	Avg.	StdDev.	Avg.	StdDev.
Neg. ctrl.	24870	1813	30172	5507
Ester only	27844	1673	37122	12212
2I only	24552	2331	30150	7381
Cetux+Ester	25932	959	30473	2935
Cetux+2I	17724	1174	25108	6241
A431 cells				
	Irr.		*Non-irr.*	
	Avg.	StdDev.	Avg.	StdDev.
Neg. ctrl.	20365	1771	34047	16013
Ester only	20910	1557	21852	4806
2I only	18931	1371	25351	5603
Cetux+Ester	18380	1574	23188	2619
Cetux+2I	10427	1096	32145	8698

A flow cytometry-based viability assay (calcein AM/ethidium homodimer) was also performed on these cell types as an orthogonal test of the same variable. The results of this assay are shown in Figures 4-S2 and 4-S3. There, a large increase in cell damage in death, as indicated by increased ethidium fluorescence, was observed in irradiated EGFR-expressing cells (HaCaT and A431) treated with antibody and MG-2I, but not in EGFR-negative cells (HEK-293). For A431 cells, (Figure 4-S2C), the great majority (>98%) of the dL5-cetuximab+MG-2I-treated cells were so damaged by irradiation that they did not survive the analysis intact (Table 4-S1). This is likely due to the higher expression of EGFR in A431s compared to HaCaT cells[159], leading to more singlet oxygen production and consequent cell damage.

A test of dL5-trastuzumab on SK-BR-3 cells provided similar photoablation results. These cells were also labeled with dL5-cetuximab and either MG-2I (Figure 4-6A and -6B) or non-photosensitizing MG Ester (Figure 4-6C and -6D). After irradiation, MG-2I-labeled SK-BR-3 cells were observed to have a disrupted and granular appearance, and vital staining revealed many cells that were dead or dying.

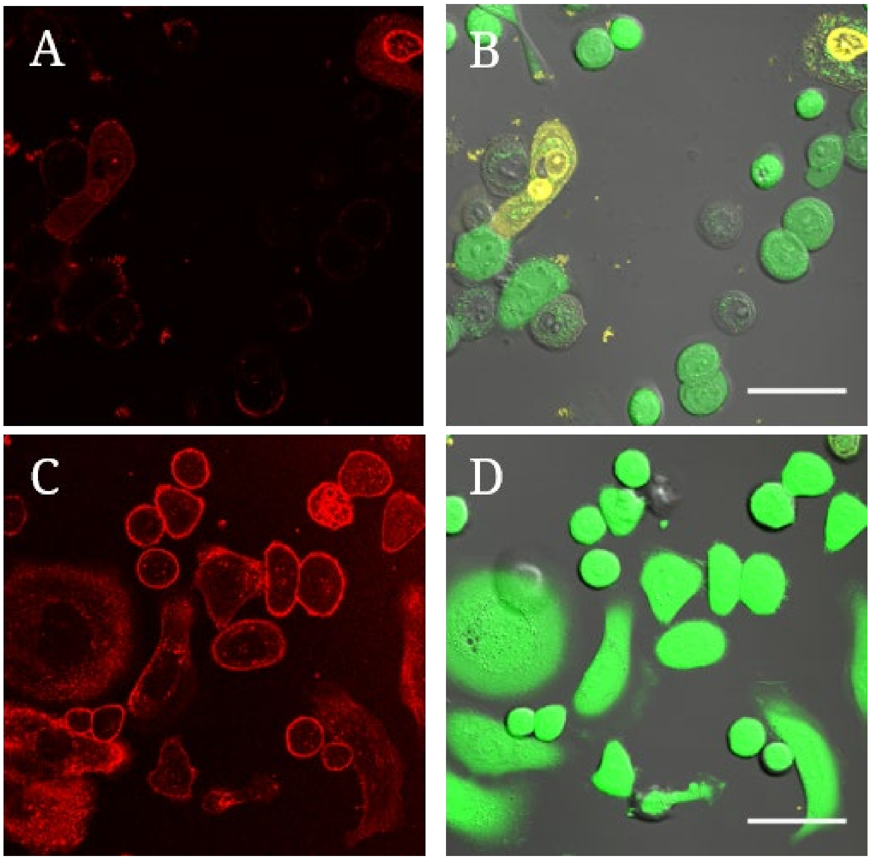

Figure 4-6. dL5-trastuzumab and MG-2I mediate cell death in HER2-expressing SK-BR-3 cells. (A-B) Red channel (MG-2I signal) and merged green and yellow channels (calcein AM and EthD-1, respectively) are shown for cells labeled with dL5-trastuzumab and MG-2I. (C-D) Red signal shown for non-photosensitizing control fluorogen MG-Ester, along with the calcein AM and EthD-1 channels. Scale bars = 50 μm.

Discussion

Efficient photo-crosslinking between the HTB1-FAP reagent and an IgG requires (1) interaction between the Fc portion of the antibody and the HTB1 domain of the reagent (which is derived from the Fc binding domain of protein G[158]), and (2) the presence of a crosslink-accepting methionine near the C_H2-C_H3 junction in the Fc domain of the antibody[158]. Such a residue is present in all human IgGs, all rabbit IgGs and three of the four subclasses of mouse IgG (IgG2a, 2b, 3). Thus, each antibody conjugate has a well-defined structure, with two FAP moieties at locations well removed from the antigen binding site. This is in distinction to antibody-fluorophore conjugates made by most other methods, where both the number and the locations of the fluorophores vary from one antibody molecule to another.

Additionally, each FAP represents a multifunctional module that, depending on the fluorogen used, provides a range of spectral and photochemical properties that can be exploited without the need to generate different antibody conjugates for different uses. The current study illustrates this versatility, with the dL5 FAP enabling the detection of cell-surface antigens, the detection of cell-cell proximity, and the photoablation of antigen expressing cells.

The opportunity to FAP-tag almost any IgG, coupled with the modularity of the FAPs themselves, gives the FAP-antibody technology broad potential application for use in multicellular organisms. Labeling and ablation of FAP-tagged cardiac cells has already been demonstrated in larval and adult transgenic zebrafish [130], and it would be reasonable to attempt to use FAP-tagged antibodies for labeling and /or ablation of other targets in this organism. Performing such experiments in mice could be problematic due to limited penetration of near infrared photons, but penetration should not be an issue for cells in cutaneous or subcutaneous locations, including subcutaneous tumors. Likewise, there is potential for therapeutic use of FAP-antibody conjugates to photoablate human tumor cells at the time of tumor resection, which is typically when photodynamic therapy is applied in cancer treatment.

Another opportunity, which extends results reported here, is to use pairs of antibody-conjugated FAPs to visualize locations where two antigens are in close proximity, as in neural or immunological synapses. FAPs expressed from recombinant genes have already been shown to enable such "trans-TEFLA" experiments in cultured cells[165], and it would be of interest to attempt trans-TEFLA labeling using FAP-tagged antibodies as both partners to investigate intercellular contacts *in vitro* and *in vivo*.

Materials and Methods

Mammalian cell culture and fixation.

HEK-293, HaCaT, A431, and SK-BR-3 cells were cultured under standard conditions in a tissue culture incubator at 37°C and 5% CO_2. Growth media was DMEM (with 4.5 g/L glucose, L-glutamine, and sodium pyruvate) supplemented with 10% fetal bovine serum and 10 U/mL penicillin and streptomycin. For imaging, cells were lifted with 0.05% trypsin+EDTA and plated on glass-bottom MatTek dishes (MatTek) to allow confocal microscopy.

For experiments on fixed cells, HaCaTs were incubated in 2% paraformaldehyde for 15 minutes at room temperature, followed by blocking with 3% BSA for one hour (if permeabilized, this was preceded by 15-minute incubation in 0.5% Triton X-100). Cells were then labeled with 50 nM antibody for an hour and subsequently labeled with MG fluorogen.

Photoablation.

For photoablation experiments, cells were immersed in PBS and placed in a custom-built LED light-box emitting at 669 nm[130] and illuminated for 7.5 minutes at approximately 50 mW/cm^2. Subsequently, cells were incubated for 1-2 hours to allow time for photoablation to have an impact on cellular processes. All samples were then labeled with 1 μM calcein AM (ThermoFisher) to label live cells and 5 μM ethidium homodimer-1 (EthD-1; ThermoFisher) to label dead cells. Thirty minutes later, cells were prepared for microscopy and imaged as described below.

Fluorescence microscopy and image analysis.

Fluorescence microscopy was performed on a Carl Zeiss LSM 880 or Andor Revolution XD Spinning Disk confocal microscope, both equipped with heated, humidified culture chambers at 5% CO_2. For all experiments, cells were incubated with 50 nM antibody for at least 15 minutes prior to washing and labeling with fluorogens to allow adequate binding to surface antigen. Following dye labeling, cells were washed and imaged using an argon 488 nm and solid-state 633 nm laser were bandpass emission filters adjusted to catch maximum signal from TO1-2p and MG fluorogens, respectively. Microscopy on the LSM 880 used an oil immersion 40X plan-neofluar objective and an oil immersion 63X plan apochromat objective. Microscopy on the Revolution XD used a dry 40X objective. Microscopy settings were adjusted to minimize signal saturation and zero value intensities and were then held constant throughout each experiment. The resulting images were analyzed using ImageJ[85].

Plate reader cell viability assay and data analysis.

For plate reader experiments, HEK-293, HaCaT, and A431 cells were plated at 10,000 cells/well in 96-well plates. Approximately 24 hours post-plating, cells were labeled with cetuximab (50 nM) and either MG Ester or MG-2I (500 nM), with wash steps in between to remove unbound reagent. One plate was then irradiated with red light as described above, while the other remained non-irradiated. Cells were incubated at 37°C for one hour and then labeled with alamarBlue cell viability stain (ThermoFisher) for 4 hours. Analysis of fluorescence was performed on a Tecan Infinite M1000 plate reader. Excitation was provided in the 540-570 nm range and emission collected from 580-610 nm as per manufacturer instructions. Gain for each cell type was optimized against the negative controls and held constant throughout the experiment. Resulting data was collated and analyzed in Microsoft Excel 2016 and GraphPad Prism 6.01 (GraphPad Software).

Flow cytometry and data analysis.

For flow cytometry experiments, HEK-293, HaCaT, and A431 cells were prepared exactly as described above for the plate reader assays. Thirty minutes post-irradiation, all cells were labeled with 5 μM EthD-1 to distinguish dead cells. After another thirty minutes, cells were lifted into Accutase (CELLnTEC) and analyzed using an Accuri C6 flow cytometer (BD Biosciences, San Jose, CA). The FL2 channel (488 nm laser for excitation with a 585/40 bandpass filter to collect emission) was used to determine signal from the ethidium homodimer-1. The FL4 channel (640 nm excitation, 670 longpass emission) was used to determine signal from the MG fluorogens. Data was collected in ForeCyt software (IntelliCyt) and analyzed using FlowJo ver. 10.2 (FlowJo LLC). Briefly, cells were gated and singlets discriminated to remove cell clumps from analysis. Median FL2 signals were calculated for each well, and averages and standard deviations calculated. Graphs were produced in GraphPad Prism 6.01.

Details of dL5 FAP.

Plasmid pG-2DL5 encoding the dL5 FAP and a C-terminal HTB1 peptide derived from Streptococcal Protein G was designed with codon usage appropriate for expression in E. coli. A UAG codon at HTB1 position A24 was included to direct incorporation of a p-benzoyl-L-phenylalanine (pBpa) residue , as described in Hui *et al.*[158]

Plasmids pEVOL- pBpF (Addgene) which carries the tRNA/aminoacyl transferase pair and the pG-2DL5 were co-transformed into Origami B(DE3) Competent Cells (EMD Millipore).

Bacterial starter cultures were grown in 2 mL LB + 100 µg/mL ampicillin + 25 µg/mL chloramphenicol at 37°C in a shaker overnight. Starter cultures were added at a 1:1000 dilution to Autoinduction Media LB Broth Base Including Trace Elements (Formedium), 100µg/mL ampicillin and 25 µg/mL chloramphenicol. For BPA incorporation, L-benzoylphenylalanine (Bachem, King of Prussia, PA) was added into the culture to a final concentration of 500 µM and arabinose was added to a final concentration of 0.1% to begin the inductions of the pEVOL plasmid. pG-2DL5 was expressed at 25°C in an open-air shaker for 72h.

Following expression, cultures were pelleted by centrifugation (5,500g for 15 min at 4°C) and the HTB1-FAP peptide was purified as previously described in Hui *et al.*[158]. SDS-PAGE electrophoresis was performed on Bolt 4-12% Bis-Tris Plus Gels (ThermoFisher) with a Mini Gel Tank (ThermoFisher), stained with SimplyBlue SafeStain (Invitrogen), and imaged using a Gel Logic 100 system (Kodak).

Photocrosslinking.

To create antibody conjugates, HTB1-FAP peptide was incubated with the IgG and exposed to long wavelength UV light (365 nm) for 2 hours[158]. Crosslinked products were purified from access proteins by using 100 kDa molecular weight cut-off (MWCO) filter (Amicon Ultra, Milipore, Temecula, CA) and then they were analyzed directly using SDS-PAGE electrophoresis.

Analysis of proteins.

Protein products were analyzed by SDS-PAGE electrophoresis. SDS-PAGE was performed on Bolt 4-12% Bis-Tris Plus Gels (ThermoFisher) with a Mini Gel Tank. Proteins were boiled 5 minutes with 1:1 volume of loading buffer (Biorad, Hercules, CA) containing 1:20 dilution of β-mercaptoethanol (Biorad). Samples were loaded and run for 30 mins at constant 200 volt. The gel was stained using SimplyBlue Coomassie stain (Invitrogen). Image of the gel was taken using a Kodak Gel Logic 100 system (Rochester, NY).

A

```
MTFKLIINGKTLKGEITIEAVDA*EAEKIFKQYANDY
GIDGEWTYDDATKTFTVTEGGSGGSYPYDVPDYAGAQ
PAQAVVTQEPSVTVSPGGTVILTCGSGTGAVTSGHYA
NWFQQKPGQAPRALIFDTDKKYSWTPGRFSGSLLGAK
AALTISDAQPEDEAEYYCSLSDVDGYLFGGGTQLTVL
SGGGGSGGGGSGGGGSGGGGSQAVVTQEPSVTVSPGG
TVILTCGSGTGAVTSGHYANWFQQKPGQAPRALIFDT
DKKYSWTPGRFSGSLLGAKAALTISDAQPEDEAEYYC
SLSDVDGYLFGGGTQLTVLS
```

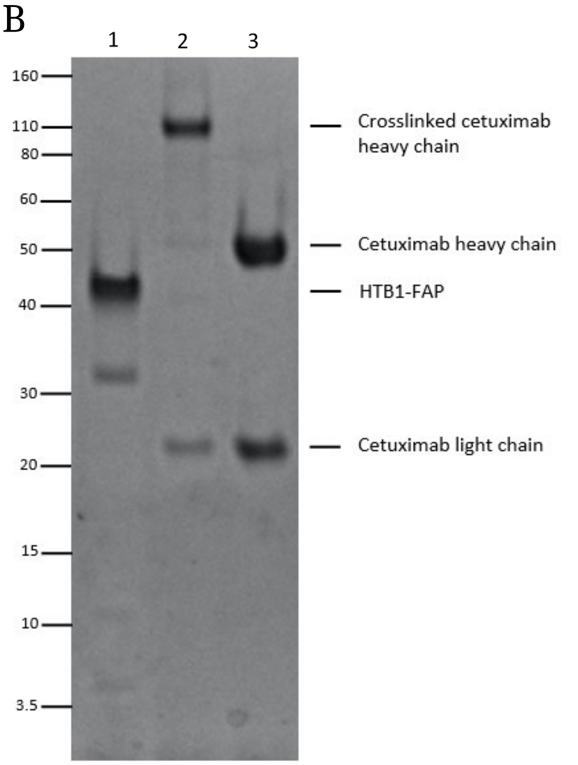
B
1
2
3
160
110
80
60
50
40
30
20
15
10
3.5
Crosslinked cetuximab heavy chain
Cetuximab heavy chain
HTB1-FAP
Cetuximab light chain

Figure 4-S1. HTB1-FAP(dL5) reagent conjugated to cetuximab. (A) Amino acid sequence of HTB1-FAP polypeptide (316 amino acids). The location of the p-benzoyl-L-phenylalanine (BPA) residue is indicated by an asterisk. (B) SDS PAGE showing crosslinked polypeptides. Lane 1: HTB1-FAP polypeptide. Lane 2: Crosslinked cetuximab. Lane 3: Cetuximab alone.

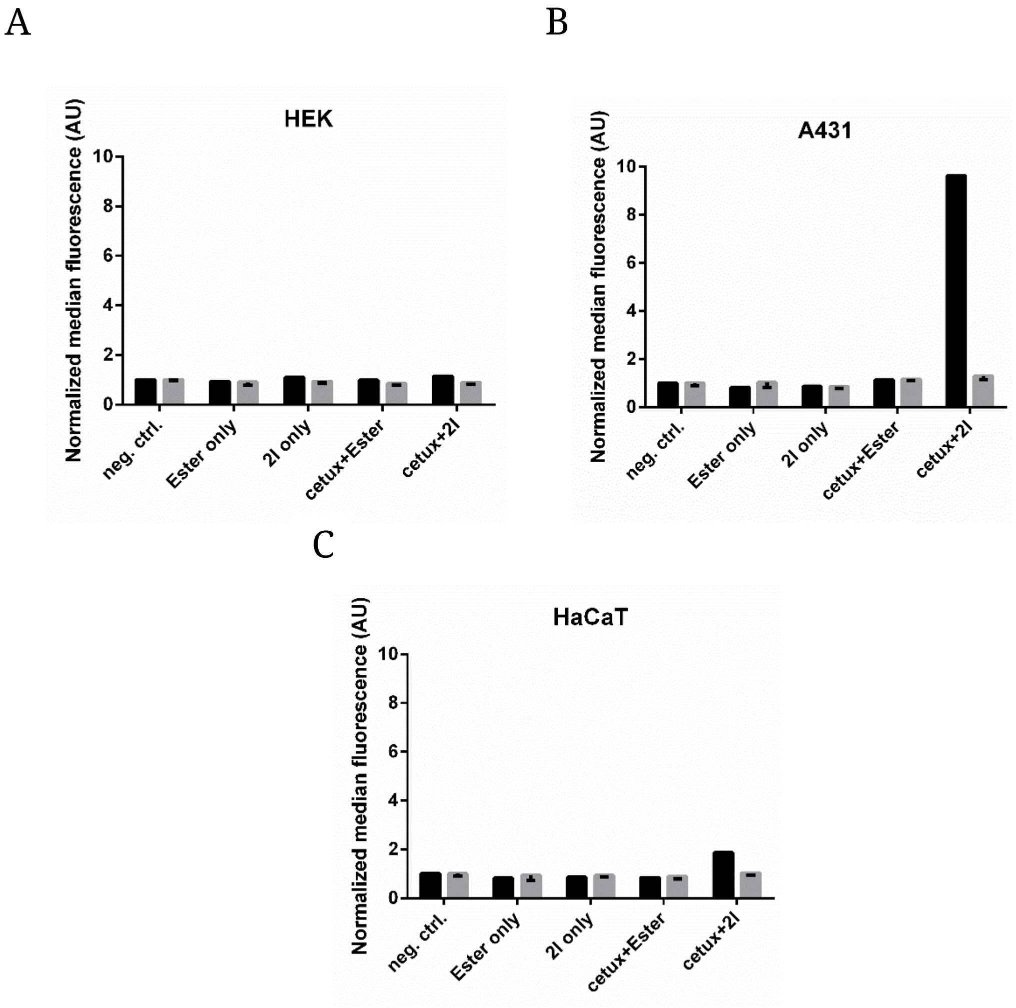

Figure 4-S2. Flow cytometric analysis of cytotoxic response via Eth-D staining in HEK, HaCaT, and A431 cells after dL5-cetuximab and MG-2I treatment and photoirradiation. Gray bars are from irradiated cells, and black bars are from non-irradiated cells. Neg. ctrl. = no antibody or dye. Ester/2I only = only fluorogen, no FAP/antibody. Cetux+Ester/2I = antibody and indicated fluorogen. Data from (A) HEK-293 cells, (B) HaCaT cells, and (C) A431 cells are shown. Numbers shown are the normalized average median FL2 signal (EthD-1 fluorescence) in arbitrary units normalized to the negative controls. Each bar is therefore the fold increase in EthD-1 signal over the negative control. Each bar is the average of three replicates ± SD.

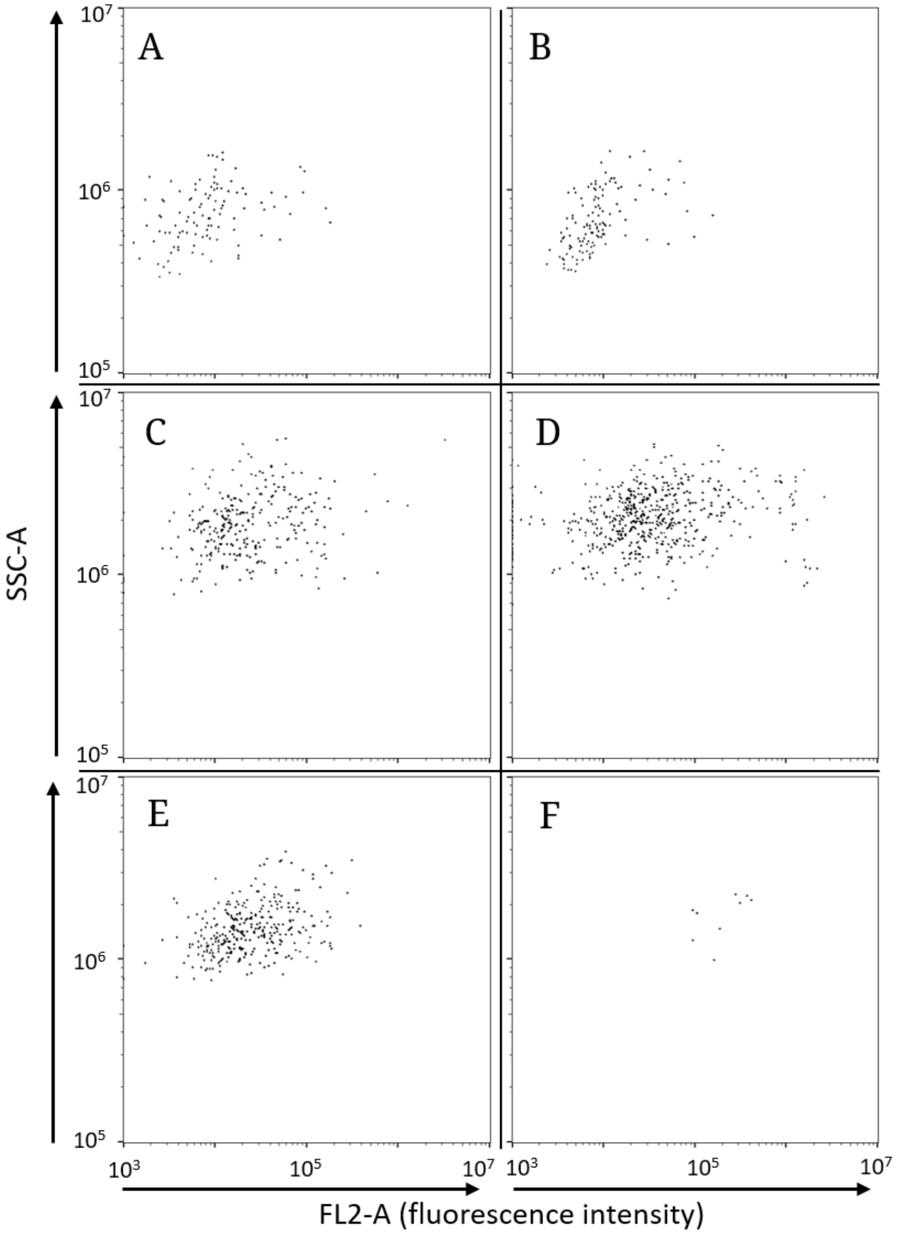

Figure 4-S3. Representative dot plots from flow cytometry data shown in Figure 3-S2. (A) and (B) HEK-293 cells. (C) and (D) HaCaT cells. (E) and (F) A431 cells. All cells shown were exposed to dL5-cetuximab and the photosensitizing fluorogen MG-2I. Cells in the right column were irradiated with 640nm light, while cells in the left column were not irradiated. Axes are side scatter vs. fluorescence intensity in the FL-2 channel (both in arbitrary units). The FL-2 channel shows signal from the dead cell stain EthD-1.

Table 4-S1. Total number of singlet cells analyzed per condition to generate the data shown in Figure 4-S2. Irr. = cells irradiated at 640 nm. Non-irr. = cells not irradiated. Neg. ctrl. = no antibody or dye. Ester/2I only = only fluorogen, no FAP/antibody. Cetux+Ester/2I = antibody and indicated fluorogen.

HEK-293 cells		
	Irr.	*Non-irr.*
Neg. ctrl.	551	314
Ester only	433	248
2I only	601	387
Cetux+Ester	534	331
Cetux+2I	455	392
HaCaT cells		
	Irr.	*Non-irr.*
Neg. ctrl.	1350	901
Ester only	1546	1317
2I only	1385	1451
Cetux+Ester	1644	1047
Cetux+2I	1779	857
A431 cells		
	Irr.	*Non-irr.*
Neg. ctrl.	1105	907
Ester only	946	1020
2I only	709	1089
Cetux+Ester	497	802
Cetux+2I	12	725

Conclusions and Future Directions (Part 2)

Altogether, the results shown in Part 2 demonstrate the development and validation of the trans-TEFLA assay of intercellular contact sensing, the use of FAP-antibody conjugates to apply this technology to wild-type cells *in vitro*, and the potential for using these conjugates as cell-selective photoablation agents. These results suggest several immediate avenues for the continuation of this project.

First, our dL5-cetuximab eliminated the need for one set of cells in trans-TEFLA to be transgenic. It is vital that this be expanded to both cells by using two FAP-antibodies in place of transgenic FAP expression. Even as methods of *in vivo* gene editing become more and more widespread, reliable production of transgenic cells in living organisms is a challenging and laborious process[166,167]. The ability to use specific antibodies (e.g. antibodies against pre- and post-synaptic neuronal markers) to label adjoining cells *in vivo* would greatly increase the physiological relevance of this technology by allow trans-TEFLA on unaltered tissues. This would also minimize the possibility of the cell contact sensor itself having an impact on the biology under observation.

Second, the demonstration of dL5-antibody-mediated photoablation in Chapter 4, though a critical proof-of-concept, did not examine in-depth the properties of the observed cell death (e.g. timecourse of death, type of cell death, etc.). Nor did it examine several possible caveats to this technology. In the original publication describing MG-2I, the photosensitizer was found to selectively kill dL5-expressing cells while leaving nearby wild-type cells untouched[130]. However, the mechanisms of MG-2I-mediated cell killing are still not entirely clear, and it is possible that the increased distance introduced by our antibody between cell and photosensitizer could lead to off-target effects.

There are several relatively simple assays that could help to answer these questions. One is to use a dL5-antibody in a mixed culture (e.g. cultured mouse neurons, which naturally intermix with astrocytes and other cell types isolated from the brain tissue). By deploying an antibody specific for one cell population in this mix, we could test its ability to selectively kill antigen-expressing cells without significant off-target effects. It will also be critical to deploy this technology *in vivo* as soon as feasible. Cetuximab is already FDA-approved and a well-researched treatment option for EGFR-overexpressing cancers. Therefore, it should be a relatively simple task to deploy this system *in vivo* and obtain preliminary data on its ability to ablate tumor cells in a mouse model of cancer.

For the trans-TEFLA cell contact labeling system, *in vivo* deployment is also the long-term goal. The antibody conjugation system developed by the Tsourkas lab should in principle be applicable to any commercially-available antibody[158], and there are a number of antibodies against pre-synaptic and post-synaptic neuronal markers that would be interesting targets for this assay[168,169]. If a pair of trans-TEFLA-compatible pre- and post-synaptic FAP-antibodies could be constructed (e.g. bassoon-dL5 and homer-1-TO1), these could be applied along with bivalent dye to cultured neurons or to tissue samples isolated from mouse brain. This should ideally produce bright co-localized fluorescence at synapses, allowing high-throughput analysis via wide-scale fluorescence microscopy.

Although testing and validation of these technologies *ex vivo* and *in vivo* is bound to present complications, the data presented in this thesis are a critical proof-of-concept for the use of trans-TEFLA to fluorescently label intercellular contacts and of FAP-antibodies to facilitate both TEFLA and selective photoablation *in vitro*. As neuroscience continues to move to the forefront of biology research, technologies that streamline our ability to produce and analyze large datasets become increasingly critical. Trans-TEFLA has the potential to dramatically simplify the process of identification and examination of neuronal (and immunological) synapses. Further, as an offshoot of this technology, FAP-antibody-mediated photoablation may lead to new avenues for both cellular biology and therapeutic development for *in vivo* applications.

Abbreviations

AAV: adeno-associated virus

bp: base pairs (DNA)

CMV: cytomegalovirus

DIR: dimethylindole red

dMNA: dissolvable microneedle array

eGFP: enhanced green fluorescent protein

ELISA: enzyme-linked immunosorbent assay

EGFR: epidermal growth factor receptor

EthD-1: ethidium homodimer-1

FAP: fluorogen-activating protein/peptide

GC: genome copy

GRASP: GFP reconstitution across synaptic partners

IgG: immunoglobulin

LPS: lipopolysaccharide (endotoxin)

MG: malachite green

NF-κB: nuclear factor kappa-light-chain-enhancer of activated B cells

NIR: near-infrared

PBS: phosphate-buffered saline

PDGFR: platelet-derived growth factor receptor

PEG: polyethylene glycol

scAvd: single-chain avidin

TAPS: targeted and activatable photosensitizer

TEFLA: tethered fluorogen assay

TNFα: tumor necrosis factor alpha

TO: thiazole orange

vp: viral particle

WPRE: woodchuck hepatitis virus post-transcriptional regulatory element

References

1. Medzhitov, R. & Horng, T. Transcriptional control of the inflammatory response. *Nat. Rev. Immunol.* **9**, 692–703 (2009).
2. Grivennikov, S. & Karin, M. Dangerous liaisons: STAT3 and NF-κB collaboration and crosstalk in cancer. *Cytokine* **21**, 11–19 (2011).
3. Lippitz, B. E. Cytokine patterns in patients with cancer: a systematic review. *Lancet Oncol.* **14**, e218-228 (2013).
4. Gea-Banacloche, J. C. Immunomodulation. in *Principles of Molecular Medicine* (eds. Runge, M. S. & Patterson, C.) 893–904 (Humana Press, 2006). doi:10.1007/978-1-59259-963-9_92
5. Yu, H., Pardoll, D. & Jove, R. STATs in cancer inflammation and immunity: a leading role for STAT3. *Nat. Rev. Cancer* **9**, 798–809 (2009).
6. Lallemand, C. *et al.* Reporter gene assay for the quantification of the activity and neutralizing antibody response to TNFα antagonists. *J. Immunol. Methods* **373**, 229–239 (2011).
7. Fransen, J. The merits of monitoring: should we follow all our rheumatoid arthritis patients in daily practice? *Rheumatology* **41**, 601–604 (2002).
8. Amsen, D., de Visser, K. E. & Town, T. Approaches to determine expression of inflammatory cytokines. *Methods Mol Biol* **511**, 107–142 (2009).
9. Burska, A., Boissinot, M. & Ponchel, F. Cytokines as biomarkers in rheumatoid arthritis. *Mediators Inflamm.* **2014**, Article 545493 (2014).
10. Johnston, G. R. & Webster, N. R. Cytokines and the immunomodulatory function of the vagus nerve. *Br. J. Anaesth.* **102**, 453–62 (2009).
11. Park, J. Y. & Kricka, L. J. Interferences in Immunoassay. *Clin. Biochem. Rev.* **25**, 105–120 (2004).
12. Marotte, H., Maslinski, W. & Miossec, P. Circulating tumour necrosis factor-alpha bioactivity in rheumatoid arthritis patients treated with infliximab: link to clinical response. *Arthritis Res. Ther.* 7, R149–R155 (2005).
13. Cloutier, G. *et al.* In-vivo and real-time ultrasonic monitoring of red blood cell aggregation with the structure factor size and attenuation estimator during and after cardiopulmonary bypass surgery in swine. *2010 IEEE Int. Ultrason. Symp.* 616–619 (2010). doi:10.1109/ULTSYM.2010.5935591
14. O'Connor, T. E., Carpenter, H. E., Bidari, S., Waters, M. F. & Hedna, V. Role of inflammatory markers in Takayasu arteritis disease monitoring. *BMC Neurol.* **14**, (2014).
15. Tsai, Y.-T. *et al.* Real-time noninvasive monitoring of in vivo inflammatory responses using a pH ratiometric fluorescence imaging probe. *Adv. Healthc. Mater.* **3**, 221–9 (2014).
16. Lardner, A. The effects of extracellular pH on immune function. *J. Leukoc. Biol.* **69**, 522–530 (2001).
17. Samulski, R. J. & Muzyczka, N. AAV-mediated gene therapy for research and therapeutic purposes. *Annu. Rev. Virol.* **1**, 427–451 (2014).
18. Hastie, E. & Samulski, R. J. AAV at 50: A golden anniversary of discovery, research,

and gene therapy success, a personal perspective. *Hum. Gene Ther.* **26**, 257–265 (2015).

19. Ellis, B. L. *et al.* A survey of ex vivo/in vitro transduction efficiency of mammalian primary cells and cell lines with nine natural adeno-associated virus (AAV1-9) and one engineered adeno-associated virus serotype. *Virol. J.* **10**, (2013).
20. Keswani, S. G. *et al.* Pseudotyped adeno-associated viral vector tropism and transduction efficiencies in murine wound healing. *Wound Repair Regen.* **20**, 592–600 (2012).
21. Kaeppel, C. *et al.* A largely random AAV integration profile after LPLD gene therapy. *Nat. Med.* **19**, 889–91 (2013).
22. Gilmore, T. D. Introduction to NF-κB: players, pathways, perspectives. *Oncogene* **25**, 6680–6684 (2006).
23. Orabi, A. I. *et al.* Dynamic imaging of pancreatic nuclear factor κ (NF-κB) activation in live mice using adeno-associated virus (AAV) infusion and bioluminescence. *J. Biol. Chem.* **290**, 11309–11320 (2015).
24. Chtarto, A. *et al.* An adeno-associated virus-based intracellular sensor of pathological nuclear factor-κB activation for disease-inducible gene transfer. *PLoS One* **8**, e53156 (2013).
25. Filonov, G. S. *et al.* Bright and stable near infra-red fluorescent protein for in vivo imaging. *Nat Biotechnol.* **29**, 757–761 (2012).
26. Wallace, D. J., Gavin, I. M., Karpenko, O., Barkhordar, F. & Gillis, B. S. Cytokine and chemokine profiles in fibromyalgia, rheumatoid arthritis and systemic lupus erythematosus: a potentially useful tool in differential diagnosis. *Rheumatol. Int.* **35**, 991–996 (2014).
27. McInnes, I. B. & Schett, G. Cytokines in the pathogenesis of rheumatoid arthritis. *Nat. Rev. Immunol.* **7**, 429–442 (2007).
28. Sattar, N., McCarey, D. W., Capell, H. & McInnes, I. B. Explaining how ‘high-grade’ systemic inflammation accelerates vascular risk in rheumatoid arthritis. *Circulation* **108**, 2957–2963 (2003).
29. Chen, Y. & Lyga, J. Brain-skin connection: stress, inflammation and skin aging. *Inflamm. Allergy Drug Targets* **13**, 177–90 (2014).
30. Nedoszytko, B., Sokołowska-Wojdyło, M., Ruckemann-Dziurdzińska, K., Roszkiewicz, J. & Nowicki, R. J. Chemokines and cytokines network in the pathogenesis of the inflammatory skin diseases: atopic dermatitis, psoriasis and skin mastocytosis. *Postep Derm Alergol* **31**, 84–91 (2014).
31. Asokan, A., Schaffer, D. V & Jude Samulski, R. The AAV vector toolkit: poised at the clinical crossroads. *Mol. Ther.* **20**, 699–708 (2012).
32. Hänel, K. H., Cornelissen, C., Lüscher, B. & Baron, J. M. Cytokines and the skin barrier. *Int. J. Mol. Sci.* **14**, 6720–6745 (2013).
33. Scharadin, T. M. & Eckert, R. L. TIG3 - an important regulator of keratinocyte proliferation and survival. *J Invest Dermatol* **134**, 1811–1816 (2014).
34. Sallach, J. *et al.* Tropism-modified AAV vectors overcome barriers to successful cutaneous therapy. *Mol. Ther.* **22**, 929–939 (2014).

35. Silverberg, N. B. The epidemiology of vitiligo. *Curr. Dermatol. Rep.* **4**, 36–43 (2015).

36. Simpson, J. K. *et al.* An exploratory study to investigate health-seeking behavior in patients with psoriasis using framework analysis. *Br. J. Dermatol.* **1**77, 742–750 (2017).

37. Di Meglio, P., Villanova, F. & Nestle, F. O. Psoriasis. *Cold Spring Harb. Perspect. Med.* **4**, (2014).

38. Spirito, F., Meneguzzi, G., Danos, O. & Mezzina, M. Cutaneous gene transfer and therapy: The present and the future. *J. Gene Med.* **3**, 21–31 (2001).

39. Del Rio, M., Gache, Y., Jorcano, J. L., Meneguzzi, G. & Larcher, F. Current approaches and perspectives in human keratinocyte-based gene therapies. *Gene Ther.* **11**, S57–S63 (2004).

40. Ghazizadeh, S. & Taichman, L. B. Virus-mediated gene transfer for cutaneous gene therapy. *Hum. Gene Ther.* **11**, 2247–2251 (2000).

41. Brill-Almon, E. *et al.* Ex vivo transduction of human dermal tissue structures for autologous implantation production and delivery of therapeutic proteins. *Mol. Ther.* **12**, 274–282 (2005).

42. Kunicher, N., Falk, H., Yaacov, B., Tzur, T. & Panet, A. Tropism of lentiviral vectors in skin tissue. *Hum. Gene Ther.* **19**, 255–66 (2008).

43. Kuhn, U. *et al.* In vivo assessment of gene delivery to keratinocytes by lentiviral vectors in vivo assessment of gene delivery to keratinocytes bylentiviral vectors. *J. Virol.* 7**6**, 1496–1504 (2002).

44. Ertl, H. C. & High, K. A. The impact of AAV capsid-specific T cell responses on design and outcome of clinical gene transfer trials with recombinant AAV vectors – an evolving controversy. *Hum. Gene Ther.* **28**, 328–337 (2017).

45. Zincarelli, C., Soltys, S., Rengo, G. & Rabinowitz, J. E. Analysis of AAV serotypes 1-9 mediated gene expression and tropism in mice after systemic injection. *Mol. Ther.* **16**, 1073–1080 (2008).

46. Calcedo, R. & Wilson, J. M. Humoral immune response to AAV. *Front. Immunol.* **4**, Article 341 (2013).

47. Nonnenmacher, M. & Weber, T. Intracellular transport of recombinant adeno-associated virus vectors. *Gene Ther.* **19**, 649–658 (2012).

48. Lakhan, R. *et al.* Local administration of AAV-DJ pseudo serotype expressing COX2 provided early onset of transgene expression and promoted bone fracture healing in mice. *Gene Ther.* **22**, 721–728 (2015).

49. Schulte, M. *et al.* Innate immune response after adenoviral gene delivery into skin is mediated by AIM2, NALP3, DAI and mda5. *Springerplus* **2**, (2013).

50. Braun-Falco, M., Doenecke, A., Smola, H. & Hallek, M. Efficient gene transfer into human keratinocytes with recombinant adeno-associated virus vectors. *Gene Ther.* **6**, 432–41 (1999).

51. Braun-Falco, M., Eisenried, A., Büning, H. & Ring, J. Recombinant adeno-associated virus type 2-mediated gene transfer into human keratinocytes is influenced by both the ubiquitin/proteasome pathway and epidermal growth factor receptor tyrosine kinase. *Arch. Dermatol. Res.* **296**, 528–535 (2005).

52. Gagnoux-Palacios, L. *et al.* Assessment of optimal transduction of primary human skin keratinocytes by viral vectors. *J. Gene Med.* 7, 1178–1186 (2005).

53. Petek, L. M., Fleckman, P. & Miller, D. G. Efficient KRT14 targeting and functional characterization of transplanted human keratinocytes for the treatment of epidermolysis bullosa simplex. *Mol. Ther.* **18**, 1624–1632 (2010).

54. Lisowski, L. *et al.* Selection and evaluation of clinically relevant AAV variants in a xenograft liver model. *Nature* **506**, 382–6 (2014).

55. Melo, S. P. *et al.* Somatic correction of junctional epidermolysis bullosa by a highly recombinogenic AAV variant. *Mol. Ther.* **22**, 725–33 (2014).

56. Chamorro, C. *et al.* Gene Editing for the efficient correction of a recurrent COL7A1 mutation in recessive dystrophic epidermolysis bullosa keratinocytes. *Mol. Ther. Nucleic Acids* **5**, e307 (2016).

57. Gudjonsson, J. E., Johnston, A., Dyson, M., Valdimarsson, H. & Elder, J. T. Mouse models of psoriasis. *J. Invest. Dermatol.* **127**, 1292–308 (2007).

58. Wagner, E. F., Schonthaler, H. B., Guinea-Viniegra, J. & Tschachler, E. Psoriasis: what we have learned from mouse models. *Nat. Rev. Rheumatol.* **6**, 704–714 (2010).

59. Krueger, J. G. Hiding under the skin: A welcome surprise in psoriasis. *Nat. Med.* **18**, 1750–1 (2012).

60. Gray, S. J. *et al.* Production of recombinant adeno-associated viral vectors and use in in vitro and in vivo administration. *Curr Protoc Neurosci* (2011). doi:10.1002/0471142301.ns0417s57

61. Grimm, D. *et al.* In vitro and in vivo gene therapy vector evolution via multispecies interbreeding and retargeting of adeno-associated viruses in vitro and in vivo gene therapy vector evolution via multispecies interbreeding and retargeting of adeno-associated viruses. *J. Virol.* **82**, 5887–5911 (2008).

62. Chtarto, a *et al.* Tetracycline-inducible transgene expression mediated by a single AAV vector. *Gene Ther.* **10**, 84–94 (2003).

63. Roupé, K. M. *et al.* Injury is a major inducer of epidermal innate immune responses during wound healing. *J. Invest. Dermatol.* **130**, 1167–1177 (2010).

64. Kotzerke, K. *et al.* Immunostimulatory activity of murine keratinocyte-derived exosomes. *Exp. Dermatol.* **22**, 650–655 (2013).

65. Abu-Humaidan, A. H. A. *et al.* The epidermal growth factor receptor is a regulator of epidermal complement component expression and complement activation. *J. Immunol.* **192**, 3355–3364 (2014).

66. Chaturvedi, V., Bacon, P., Bodner, B. & Nickoloff, B. J. Proliferating cultured human keratinocytes are more susceptible to apoptosis compared with mouse keratinocytes. *J. Invest. Dermatol.* **123**, 1200–1203 (2004).

67. Bhrigu, V. & Trempe, J. P. Adeno-associated virus infection of murine fibroblasts with help provided by mouse adenovirus. *Virology* **390**, 22–30 (2009).

68. Maersch, S., Huber, A., Büning, H., Hallek, M. & Perabo, L. Optimization of stealth adeno-associated virus vectors by randomization of immunogenic epitopes. *Virology* **397**, 167–175 (2010).

69. Bell, P. *et al.* A comparative analysis of novel fluorescent proteins as reporters for

gene transfer studies. *J. Histochem. Cytochem.* **55**, 931–9 (2007).

70. Bonnotte, B. *et al.* Intradermal injection, as opposed to subcutaneous injection, enhances immunogenicity and suppresses tumorigenicity of tumor cells. *Cancer Res.* **63**, 2145–2149 (2003).

71. Bediz, B. *et al.* Dissolvable microneedle arrays for intradermal delivery of biologics: fabrication and application. *Pharm. Res.* **31**, 117–135 (2014).

72. Kim, Y.-C., Park, J.-H. & Prausnitz, M. R. Microneedles for drug and vaccine delivery. *Adv Drug Deliv Rev* **64**, 1547–1568 (2012).

73. Carey, J. B. *et al.* Microneedle-mediated immunization of an adenovirus-based malaria vaccine enhances antigen-specific antibody immunity and reduces anti-vector responses compared to the intradermal route. *Sci. Rep.* **4**, 6154 (2014).

74. Bachy, V. *et al.* Langerin negative dendritic cells promote potent CD8 + T-cell priming by skin delivery of live adenovirus vaccine microneedle arrays. *Proc. Natl. Acad. Sci. U. S. A.* **110**, 3041–3046 (2013).

75. Li, J. *et al.* Gene transfer for psoriasis in the K14-VEGF transgenic mouse model by topical transdermal delivery of interleukin-4 using ultradeformable cationic liposome. *J. Gene Med.* **12**, 481–490 (2010).

76. Chen, J. & Roop, D. R. Genetically engineered mouse models for skin research: taking the next step. *J. Dermatol. Sci.* **52**, 1–12 (2008).

77. Zhou, D. *et al.* Highly branched poly(β-amino ester)s for skin gene therapy. *J. Control. Release* **244**, 336–346 (2016).

78. Avci, P. *et al.* Animal models of skin disease for drug discovery. *Expert Opin. Drug Discov.* **8**, 331–55 (2013).

79. González-González, E. *et al.* Visualization of plasmid delivery to keratinocytes in mouse and human epidermis. *Sci. Rep.* **1**, (2011).

80. Lara, M. F. *et al.* Inhibition of CD44 gene expression in human skin models, using self-delivery short interfering RNA administered by dissolvable microneedle arrays. *Hum. Gene Ther.* **23**, 816–823 (2012).

81. Klein, R. L., Dayton, R. D., Tatom, J. B., Henderson, K. M. & Henning, P. P. AAV8, Rh10, Rh43 vector gene transfer in the rat brain: effects of serotype, promoter and purification method. *Mol. Ther.* **16**, 89–96 (2008).

82. Madigan, V. J. & Asokan, A. Engineering AAV receptor footprints for gene therapy. *Curr. Opin. Virol.* **18**, 89–96 (2016).

83. Lock, M. *et al.* Rapid, simple, and versatile manufacturing of recombinant adeno-associated viral vectors at scale. *Hum. Gene Ther.* **21**, 1259–71 (2010).

84. Duan, D., Yan, Z., Yue, Y. & Engelhardt, J. F. Structural analysis of adeno-associated virus transduction circular intermediates. *Virology* **261**, 8–14 (1999).

85. Collins, T. J. ImageJ for microscopy. *Biotechniques* **43**, 25–30 (2007).

86. Wieder, K. J. *et al.* Optimization of reporter cells for expression profiling in a microfluidic device. *Biomed. Microdevices* 7, 213–222 (2005).

87. Badr, C. E. *et al.* Real-time monitoring of nuclear factor kappaB activity in cultured cells and in animal models. *Mol. Imaging* **8**, 278–290 (2009).

88. Wan, F. & Lenardo, M. J. Specification of DNA binding activity of NF-κB proteins.

Cold Spring Harb. Perspect. Biol. **1**, a000067 (2009).

89. Choy, E. Understanding the dynamics: pathways involved in the pathogenesis of rheumatoid arthritis. *Rheumatology* **51**, v3–v11 (2012).

90. Korkmaz, E. *et al.* Therapeutic intradermal delivery of tumor necrosis factor-alpha antibodies using tip-loaded dissolvable microneedle arrays. *Acta Biomater.* **24**, 96–105 (2015).

91. Dong, B., Nakai, H. & Xiao, W. Characterization of genome integrity for oversized recombinant AAV vector. *Mol. Ther.* **18**, 87–92 (2010).

92. Zabel, U., Schreck, R. & Baeuerle, P. A. DNA binding of purified transcription factor NF-κB. *J. Biol. Chem.* **266**, 252–260 (1991).

93. Frangioni, J. In vivo near-infrared fluorescence imaging. *Curr. Opin. Chem. Biol.* **7**, 626–634 (2003).

94. Li, X. *et al.* Generation of destabilized freen fluorescent protein as a transcription reporter. *J. Biol. Chem.* **273**, 34970–34975 (1998).

95. Kitsera, N., Khobta, A. & Epe, B. Destabilized green fluorescent protein detects rapid removal of transcription blocks after genotoxic exposure. *Biotechniques* **43**, 222–227 (2007).

96. Varallyay, C. G. *et al.* Cyclophosphamide enhances human tumor growth in nude rat xenografted tumor models. *Neoplasia* **11**, 187–195 (2015).

97. Belinsky, S. A. Unmasking the lung cancer epigenome. *Annu. Rev. Physiol.* **77**, 453–474 (2015).

98. Andersson, P. S., Kjelli, E. N., Montan, S., Svanrerg, K. & Svanberg, S. Autofluorescence of various rodent tissues and human skin tumour samples. *Lasers Med. Sci.* **2**, 41–49 (1987).

99. Shcherbakova, D. M. *et al.* Bright monomeric near-infrared fluorescent proteins as tags and biosensors for multiscale imaging. *Nat. Commun.* **7**, (2016).

100. Shcherbakova, D. M. & Verkhusha, V. V. Near-infrared fluorescent proteins for multicolor in vivo imaging. *Nat Methods* **10**, 751–754 (2013).

101. Troy, T., Jekic-McMullen, D., Sambucetti, L. & Rice, B. Quantitative comparison of the sensitivity of detection of fluorescent and bioluminescent reporters in animal models. *Mol. Imaging* **3**, 9–23 (2004).

102. Ignowski, J. M. & Schaffer, D. V. Kinetic analysis and modeling of firefly luciferase as a quantitative reporter gene in live mammalian cells. *Biotechnol. Bioeng.* **86**, 827–834 (2004).

103. Straub, R. H. & Schradin, C. Chronic inflammatory systemic diseases: An evolutionary trade-off between acutely beneficial but chronically harmful programs. *Evol. Med. Public Heal.* 37–51 (2016). doi:10.1093/emph/eow001

104. El-Gabalawy, H., Guenther, L. C. & Bernstein, C. N. Epidemiology of immune-mediated inflammatory diseases : incidence, prevalence, natural history, and comorbidities. *J. Rheumatol.* **85**, 2–10 (2010).

105. Marshall, M. V *et al.* Near-infrared fluorescence imaging in humans with indocyanine green: a review and update. *Open Surg Oncol J* **2**, 12–25 (2012).

106. Chen, C., Akerstrom, V., Baus, J., Lan, M. S. & Breslin, M. B. Comparative analysis of

the transduction efficiency of five adeno associated virus serotypes and VSV-G pseudotype lentiviral vector in lung cancer cells. *Virol. J.* **10**, 86 (2013).

107. Teramoto, S., Bartlett, J. S., Carty, D. M. C., Xiao, X. & Samulski, R. J. Factors influencing adeno-associated virus-mediated gene transfer to human cystic fibrosis airway epithelial cells : comparison with Aadenovirus vectors. *J. Virol.* **72**, 8904–8912 (1998).

108. Al-Zahrani, S. *et al.* Microneedle-mediated vaccine delivery: Harnessing cutaneous immunobiology to improve efficacy. *Expert Opin. Drug Deliv.* **9**, 541–550 (2012).

109. Bal, S. M., Caussin, J., Pavel, S. & Bouwstra, J. a. In vivo assessment of safety of microneedle arrays in human skin. *Eur. J. Pharm. Sci.* **35**, 193–202 (2008).

110. Xu, T. *et al.* The evolution of the bacterial luciferase gene cassette (lux) as a real-time bioreporter. *Sensors* **12**, 732–752 (2012).

111. Gautier, A. & Tebo, A. G. Fluorogenic protein-based strategies for detection, actuation, and sensing. *BioEssays* **40**, 1–10 (2018).

112. Lee, N. *et al.* Time-lapse live-cell imaging reveals dual function of Oseg4, drosophila WDR35, in ciliary protein trafficking. *Mol. Cells* **41**, 676–683 (2018).

113. Zhang, P., Monteiro da Silva, G., Deatherage, C., Burd, C. & DiMaio, D. Cell-penetrating peptide mediates intracellular membrane passage of human papillomavirus L2 protein to trigger retrograde trafficking. *Cell* **175**, 1465–1476 (2018).

114. Cui, Y., Gao, C., Zhao, Q. & Jiang, L. Using fluorescent protein fusions to study protein subcellular localization and dynamics in plant cells. in *High-Resolution Imaging of Cellular Proteins* (eds. Schwartzbach, S. D., Skalli, O. & Schikorski, T.) 113–123 (Humana Press, 2016). doi:10.1007/978-1-4939-6352-2_7

115. Afuwape, O. A. T. & Kavalali, E. T. Imaging synaptic vesicle exocytosis-endocytosis with pH-sensitive fluorescent proteins. in *High-Resolution Imaging of Cellular Proteins* (eds. Schwartzbach, S. D., Skalli, O. & Schikorski, T.) 187–200 (Humana Press, 2016). doi:10.1007/978-1-4939-6352-2_11

116. Simhal, A. K. *et al.* Probabilistic fluorescence-based synapse detection. *PLOS Comput. Biol.* **13**, e1005493 (2017).

117. Belmer, A., Klenowski, P. M., Patkar, O. L. & Bartlett, S. E. Mapping the connectivity of serotonin transporter immunoreactive axons to excitatory and inhibitory neurochemical synapses in the mouse limbic brain. *Brain Struct. Funct.* **222**, 1297–1314 (2017).

118. Shearin, A. H. K., Quinn, C. D., Robert, D., Macdonald, I. S. & Stowers, R. S. t-GRASP, a targeted GRASP for assessing neuronal connectivity. *J. Neurosci. Methods* **306**, 94–102 (2018).

119. Hong, S., Wilton, D. K., Stevens, B. & Richardson, D. S. Structured illumination microscopy for the investigation of synaptic structure and function. *Methods Mol Biol* **1538**, 155–167 (2017).

120. Chen, Y. *et al.* Cell-type specific labeling of synapses in vivo through Synaptic Tagging with Recombination (STaR). *Neuron* **81**, 280–293 (2014).

121. Macpherson, L. J. *et al.* Dynamic labelling of neural connections in multiple colours by trans-synaptic fluorescence complementation. *Nat. Commun.* **6**, (2015).

122. Feinberg, E. H. *et al.* GFP Reconstitution Across Synaptic Partners (GRASP) defines cell contacts and synapses in living nervous systems. *Neuron* **57**, 353–363 (2008).

123. Yamagata, M. & Sanes, J. R. Transgenic strategy for identifying synaptic connections in mice by fluorescence complementation (GRASP). *Front. Mol. Neurosci.* **5**, 1–9 (2012).

124. Lundqvist, M. *et al.* Chromophore pre-maturation for improved speed and sensitivity of split-GFP monitoring of protein secretion. *Sci. Rep.* **9**, 310 (2019).

125. Liu, D. S., Loh, K. H., Lam, S. S., White, K. A. & Ting, A. Y. Imaging trans-cellular neurexin-neuroligin interactions by enzymatic probe ligation. *PLoS One* **8**, e52823 (2013).

126. Szent-Gyorgyi, C. *et al.* Fluorogen-activating single-chain antibodies for imaging cell surface proteins. *Nat. Biotechnol.* **26**, 235–240 (2008).

127. Wang, Y. *et al.* Fluorogen activating protein-affibody probes: modular , no-wash measurement of epidermal growth factor receptors. *Bioconjug. Chem.* **26**, 137–144 (2014).

128. Perkins, L. A. *et al.* Genetically Targeted Ratiometric and Activated pH Indicator Complexes (TRApHIC) for receptor trafficking. *Biochemistry* **57**, 861–871 (2018).

129. Telmer, C. A. *et al.* Rapid, specific, no-wash, far-red fluorogen activation in subcellular compartments by targeted fluorogen activating proteins. *ACS Chem. Biol.* **10**, 1239–1246 (2015).

130. He, J. *et al.* A near-infrared genetically targetable and activatable photosensitizer. *Nat. Methods* **13**, 263–268 (2016).

131. Pham, H. H. *et al.* Biochromophoric dyes for wavelength shifting of dye-protein fluoromodules. *Org Biomol Chem* **13**, 3699–3710 (2015).

132. Bruchez, M. P. Dark dyes-bright complexes: fluorogenic protein labeling. *Curr. Opin. Chem. Biol.* **27**, 18–23 (2015).

133. Schwartz, S. L. *et al.* Fluorogen-activating proteins provide tunable labeling densities for tracking FceRI independent of IgE. *ACS Chem. Biol.* **10**, 539–546 (2015).

134. Szent-Gyorgyi, C. *et al.* Malachite green mediates homodimerization of antibody VL domains to form a fluorescent ternary complex with singular symmetric interfaces. *J. Mol. Biol.* **425**, 4595–4613 (2013).

135. Saurabh, S., Perez, A. M., Comerci, C. J., Shapiro, L. & Moerner, W. E. Super-resolution imaging of live bacteria cells using a genetically directed, highly photostable fluoromodule. *J. Am. Chem. Soc.* **138**, 10398–10401 (2016).

136. Wu, Y. *et al.* Discovery of regulators of receptor internalization with high-throughput flow cytometry. *Mol. Pharmacol.* **82**, 645–657 (2012).

137. Holleran, J. P., Zeng, J., Frizzell, R. A. & Watkins, S. C. Regulated recycling of mutant CFTR is partially restored by pharmacological treatment. *J. Cell Sci.* **126**, 2692–2703 (2013).

138. Fisher, G. W. *et al.* Self-checking cell-based assays for GPCR desensitization and resensitization. *J. Biomol. Screen.* **19**, 1220–1226 (2014).

139. Vasilev, K. V, Gallo, E., Shank, N. & Jarvik, J. W. Novel biosensor of membrane protein proximity based on fluorogen activated proteins. *Comb. Chem. High*

Throughput Screen. **19**, 392–399 (2016).

140. Nordlund, H. R. *et al.* Tetravalent single-chain avidin: from subunits to protein domains via circularly permuted avidins. *Biochem. J.* **392**, 485–491 (2005).

141. Constantin, T. P. *et al.* Synthesis of new fluorogenic cyanine dyes and incorporation into RNA fluoromodules. *Org. Lett.* **10**, 1561–1564 (2008).

142. Yan, Q. *et al.* Localization microscopy using noncovalent fluorogen activation by genetically encoded fluorogen activating proteins. *Chemphyschem* **15**, 687–695 (2014).

143. Yan, Q. *et al.* Near-instant surface-selective fluorogenic protein quantification using sulfonated triarylmethane dyes and fluorogen activating proteins. *Org. Biomol. Chem.* **13**, 2078–2086 (2015).

144. Chen, W. T. & Singer, S. J. Immunoelectron microscopic studies of the sites of cell-substratum and cell-cell contacts in cultured fibroblasts. *J. Cell Biol.* **95**, 205–222 (1982).

145. de Boer, P., Hoogenboom, J. P. & Giepmans, B. N. G. Correlated light and electron microscopy: ultrastructure lights up! *Nat. Methods* **12**, 503–13 (2015).

146. Magenau, A. J. D. *et al.* Genetically targeted fluorogenic macromolecules for subcellular imaging and cellular perturbation. *Biomaterials* **66**, 1–8 (2015).

147. Yook, C., Druckmann, S. & Kim, J. Mapping mammalian synaptic connectivity. *Cell. Mol. Life Sci.* 7**0**, 4747–4757 (2013).

148. Kim, J. *et al.* mGRASP enables mapping mammalian synaptic connectivity with light microscopy. *Nat. Methods* **9**, 96–102 (2011).

149. Gallo, E., Vasilev, K. V & Jarvik, J. Fluorogen-activating-proteins as universal affinity biosensors for immunodetection. *Biotechnol. Bioeng.* **111**, 475–484 (2014).

150. Holleran, J. *et al.* Fluorogen-activating proteins as biosensors of cell-surface proteins in living cells. *Cytom. A* 77, 776–782 (2010).

151. Schindelin, J. *et al.* Fiji: an open-source platform for biological-image analysis. *Nat. Methods* **9**, 676–682 (2012).

152. Lorenz-Guertin, J. M. *et al.* A versatile optical tool for studying synaptic GABA $_A$ receptor trafficking. *J. Cell Sci.* **130**, 3933–3945 (2017).

153. Fisher, G. W. *et al.* Detection and quantification of β2AR internalization in living cells using FAP-based biosensor technology. *J. Biomol. Screen.* **15**, 703–709 (2010).

154. Gallo, E. & Jarvik, J. W. Breaking the color barrier – a multi-selective antibody reporter offers innovative strategies of fluorescence detection. *J. Cell Sci.* **130**, 2644–2653 (2017).

155. Pratt, C. P., He, J., Wang, Y., Barth, A. L. & Bruchez, M. P. Fluorogenic Green-Inside Red-Outside (GIRO) labeling approach reveals adenylyl cyclase-dependent control of BKα surface expression. *Bioconjug. Chem.* **26**, 1963–1971 (2015).

156. Escors, D. & Breckpot, K. Lentiviral vectors in gene therapy: Their current status and future potential. *Arch. Immunol. Ther. Exp. (Warsz).* **58**, 107–119 (2011).

157. Wang, Y. *et al.* Affibody-targeted fluorogen activating protein for in vivo tumor imaging. *Chem. Commun.* **53**, 2001–2004 (2017).

158. Hui, J. Z., Tamsen, S., Song, Y. & Tsourkas, A. LASIC : Light Activated Site-Specific

Conjugation of native IgGs. *Bioconjug. Chem.* **26**, 1456–1460 (2015).

159. Thul, P. J. *et al.* A subcellular map of the human proteome. *Science* **356**, eaal3321 (2017).

160. Zhang, F. *et al.* Quantification of epidermal growth factor receptor expression level and binding kinetics on cell surfaces by surface plasmon resonance imaging. *Anal Chem* **87**, 9960–9965 (2015).

161. Ockenga, W., Kühne, S., Bocksberger, S., Banning, A. & Tikkanen, R. Epidermal growth factor receptor transactivation is required for mitogen-activated protein kinase activation by muscarinic acetylcholine receptors in HaCaT keratinocytes. *Int. J. Mol. Sci.* **15**, 21433–21454 (2014).

162. Yewale, C., Baradia, D., Vhora, I., Patil, S. & Misra, A. Epidermal growth factor receptor targeting in cancer: A review of trends and strategies. *Biomaterials* **34**, 8690–8707 (2013).

163. Chen, M., Chen, L. M., Lin, C. Y. & Chai, K. X. The epidermal growth factor receptor (EGFR) is proteolytically modified by the Matriptase-Prostasin serine protease cascade in cultured epithelial cells. *Biochim. Biophys. Acta - Mol. Cell Res.* **1783**, 896–903 (2008).

164. Holliday, D. L. & Speirs, V. Choosing the right cell line for breast cancer research. *Breast Cancer Res* **13**, (2011).

165. Ackerman, D. S., Vasilev, K. V., Schmidt, B. F., Cohen, L. B. & Jarvik, J. W. Tethered fluorogen assay to visualize membrane apposition in living cells. *Bioconjug. Chem.* **28**, 1356–1362 (2017).

166. Ghosh, D., Venkataramani, P., Nandi, S. & Bhattacharjee, S. CRISPR–Cas9 a boon or bane: the bumpy road ahead to cancer therapeutics. *Cancer Cell Int.* **19**, 1–10 (2019).

167. Tratar, U. L., Horvat, S. & Cemazar, M. Transgenic mouse models in cancer research. *Front. Oncol.* **8**, 268 (2018).

168. Chung, W., Allen, N. J. & Eroglu, C. Astrocytes control synapse formation, function, and elimination. *Cold Spring Harb. Perspect. Biol.* 7, a020370 (2015).

169. Bayés, À. *et al.* Evolution of complexity in the zebrafish synapse proteome. *Nat. Commun.* **8**, 14613 (2017).

170. Zufferey, R., Donello, J. E., Trono, D. & Hope, T. J. Woodchuck hepatitis virus posttranscriptional regulatory element enhances expression of transgenes delivered by retroviral vectors. *J. Virol.* 7**3**, 2886–2892 (1999).

171. Choi, J.-H. *et al.* Optimization of AAV expression cassettes to improve packaging capacity and transgene expression in neurons. *Mol. Brain* 7, 17 (2014).